Annual Report 2019 of the Institute for Nuclear and Energy Technologies

Walter Tromm (Ed.)

Walter Tromm (Ed.)

**Annual Report 2019 of the Institute
for Nuclear and Energy Technologies**

Karlsruhe Institute of Technology

KIT SCIENTIFIC REPORTS 7759

Annual Report 2019 of the Institute for Nuclear and Energy Technologies

Edited by
Walter Tromm

Report-Nr. KIT-SR 7759

Content

Institute for Nuclear and Energy Technologies

Structure and Laboratories of the Institute of Nuclear and Energy Technologies

Walter Tromm

The Institute for Nuclear and Energy Technologies (IKET) is situated with its offices and research laboratories in Campus North of Karlsruhe Institute of Technology (KIT).

The research of IKET focuses on conversion from thermal power to electric power for future power plants without CO2 emission, on hydrogen technologies for energy storage and on safety. Traditionally, nuclear power plants, for which IKET concentrates on their safety features and on methods to mitigate severe accidents, were in the focus of investigation. IKET uses its competence, gained from a profound experience in numerical simulation and in design and operation of large-scale experimental facilities to apply this knowledge more and more in the area of renewable energies.

The combination of science and technology with education and training is a systematic approach at KIT, and IKET is contributing accordingly to courses in mechanical engineering, supervises several bachelor and master theses each year and coordinates master programs in energy technologies. Compact courses on energy technologies are given also in executive master programs and in the Framatome Professional School, which is funded by industry and managed by IKET.

Resources

The employees of IKET contribute in the research field energy of the Helmholtz Association (HGF) to the research-programs Nuclear Waste Management, Safety and Radiation Research (NUSAFE), Fusion (FUSION), Renewable Energies (EE) as well as Storage and Cross-linked Infrastructures (SCI), with a focus

on NUSAFE. By the end of 2019, around 75 scientists, engineers and technicians have been working at IKET on this wide range of CO_2-free technologies for energy conversion. Fig. 1 illustrates that more than half of the IKET employees were still working for the NUSAFE program, despite the German phase-out decision, but in accordance with the German energy politics and the 7th Energy Research Program of the German Federal Government. Around two third of the employees were funded in 2019 by the Helmholtz Association (HGF), the others by third party funds of the European Commission, by industry, by German ministries or by other research funds. Doctoral students as well as students of the Baden-Wuerttemberg Cooperative State University (DHBW) were filling around 20% of these positions at IKET. In addition, students perform their bachelor or master theses or spend an internship in the research laboratories of IKET.
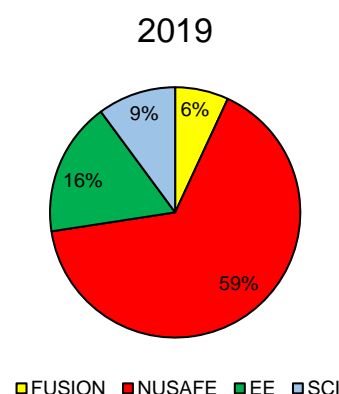
Figure 1: Assignment of IKET personnel to HGF programs.

An overview of the structure of IKET is given by the organization chart, Fig. 2. Each working group is acting in close collaboration with the other groups, particularly in its own research program.

```
┌─────────────────────────────┐
│ Institute for Nuclear and   │
│ Energy Technologies         │
│ W. Tromm (komm.)            │
│ Deputy W. Raskob            │
└─────────────────────────────┘

┌──────────────┐  ┌──────────────┐
│ Multiphase   │  │ Framatome    │
│ Flow         │  │ Professional │
│ S. Gabriel   │  │ School       │
│              │  │ A. Class     │
└──────────────┘  └──────────────┘

┌──────────────┐  ┌──────────────┐
│ Severe Acci- │  │ Magnetohy-   │
│ dent Re-     │  │ drodynamics  │
│ search       │  │ L. Bühler    │
│ X.-Y. Gaus-Liu│ │              │
└──────────────┘  └──────────────┘

┌──────────────┐  ┌──────────────┐
│ Accident Man-│  │ Hydrogen     │
│ agement Sys- │  │ T. Jordan    │
│ tems         │  │              │
│ W. Raskob    │  │              │
└──────────────┘  └──────────────┘

┌──────────────┐  ┌──────────────┐
│ Liquid Metal │  │ Energy and   │
│ Laboratory   │  │ Process En-  │
│ T. Wetzel    │  │ gineering    │
│              │  │ D. Kuhn      │
└──────────────┘  └──────────────┘

┌──────────────┐  ┌──────────────┐
│ Transmuta-   │  │ Infrastruc-  │
│ tion         │  │ ture         │
│ A. Rineiski  │  │ K. Arheidt   │
└──────────────┘  └──────────────┘
```

Figure 2: Organization chart of the Institute for Nuclear and Energy Technologies

Working groups on Severe Accident Research, and on Transmutation as well as the Framatome Professional School have been concentrating in 2019 primarily on nuclear applications, whereas the Karlsruhe Liquid Metal Laboratory (KALLA) and the Hydrogen group were addressing nuclear as well as renewable energy technologies. The working group on Magneto-Hydrodynamics is primarily working on nuclear fusion applications, whereas the working group on Energy and Process Engineering is rather concentrating on geothermal energies. The working group Multiphase Flows is mainly experimentally investigating technically relevant, complex flow phenomena. The field of activity currently comprises mainly the complex structure of the COSMOS-H high-pressure loop. The working group on Accident Management Systems continued to extend the application of its simulation models to several critical infrastructures. Thus, the institute covers a wide field of different energy technologies, and the share of its personnel resources on the different research topics reflects the requirements of the Helmholtz Association's energy research field.

They are all supported by a joint infrastructure, comprising a metal workshop, manufacturing urgent test components, a welding shop, and an electromechanical workshop. Other tasks of the infrastructure include the IT-administration, business administration and public website of the IKET. The Infrastructure team is active as well in education and training activities.

Every year, at least four students of the Baden-Württemberg Cooperative State University are employed by IKET, managed by the Infrastructure group, to work with the research teams as part of their educational program.

Working in a research area with industrial application IKET practices a Quality Management System appropriate to EN ISO 9001.

International Research Projects

Most studies performed at IKET are embedded in international research projects. A few extraordinary highlights for 2019 are given below:

Highlight: Hydrogen group: HyTunnel-CS

The Hydrogen group is strongly involved in the HyTunnel-CS project. The aim of the HyTunnel-CS project is to perform pre-normative research for safety of hydrogen driven vehicles and transport through tunnels and similar confined spaces. The main ambition is to facilitate hydrogen vehicles entering underground traffic systems at risk below or the same as for fossil fuel transport. The specific objectives are: critical analysis of effectiveness of conventional safety measures for hydrogen incidents; generation of unique experimental data using the best European hydrogen safety research facilities and three real tunnels; understanding of relevant physics to underpin the advancement of hydrogen safety engineering; innovative explosion and fire prevention and mitigation strategies; new validated CFD and FE models for consequences analysis; new engineering correlations for novel quantitative risk assessment methodology tailored for tunnels and underground parking; harmonised recommendations for intervention strategies and tactics for first responders; recommendations for inherently safer use of hydrogen vehicles in underground transportation systems; recommendations for RCS.

The objectives will be achieved by conducting inter-disciplinary and inter-sectoral research by a carefully built consortium of academia, emergency services, research and standard development organisations, who have extensive experience from work on hydrogen safety and safety in tunnels and other confined spaces. The complementarities and synergies of theoretical, numerical and experimental research will be used to close knowledge gaps and resolve technological bottlenecks in safe use of hydrogen in confined spaces. The project outcomes will be reflected in appropriate recommendations, models and correlations. HyTunnel-CS will reduce over-conservatism, increase efficiency of installed safety equipment and systems to save costs of underground traffic systems.

The 1st progress meeting was hosted in Karlsruhe by the Hydrogen working group on the 11th-13th September 2019.

Figure 3: HyTunnel-CS consortium and SAB members at the 1st progress meeting in Karlsruhe, 13th September 2019.

Highlight UNF: CONFIDENCE

First of January 2017, the CONFIDENCE (COping with uNcertainties For Improved modelling and DEcision making in Nuclear emergenCiEs) project started as Task 9.1 of the H2020 project CONCERT. The project focuses on identifying and reducing uncertainties in the release and post-release phases of an emergency. The latter includes the transition between the short-term post-release and recovery phases (e.g. the first year(s)). The group emergency management (UNF) coordinated CONFIDENCE. The scientific challenges were addressed though six interlinked work packages (WP), with an additional E&T WP. UNF also contributed to several work packages and coordinated WP6.

Besides the improved Multi Criteria Decision Analysis tool described in this report, UNF was heavily engaged in enhancing the decision

support system JRODOS for nuclear and radiological emergencies to deal with uncertain input of weather and source term. In this respect, JRODOS was extended by an ensemble generator and an ensemble visualisation engine (ensemble approach means realisation of a state by many simulations with slightly different initial conditions). A typical application case consists of an ensemble of 20 weather files and 3 source terms (realistic, worst and optimistic case) with their probabilities of occurrence. The resulting 60 scenarios are processed in one project and stored individually. In a second step and evaluation module allows visualising probability functions of interesting results such as areas of early countermeasures. The percentiles represent probability that a grid point is affected by a particular countermeasure. The 50% percentile means that in our example with 60 cases, 30 result in a countermeasure at that location. Visualisation is still an issue that needs further discussion with decision makers. Colour tables of the visualisation can be adapted by the user
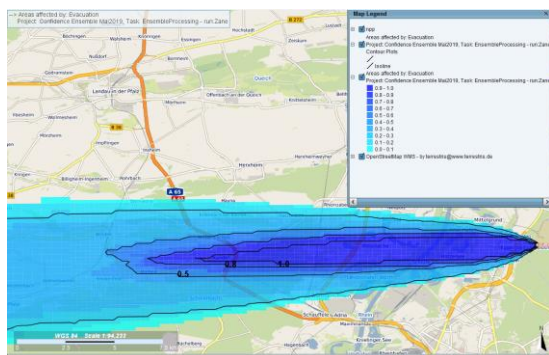
Figure 4: Map from the JRODOS ensemble processor for ensemble runs with blue colour table and added contour plots separating areas with fraction borders of 1, 0.8, 0.5 and 0.2

Future research will concentrate on the testing of the ensemble approach in particular related to operational applications, communicating to decision makers and lay people as well as comparing different weather providers with each other. There is one important question

not resolved: Do the numerical weather prediction ensemble really represent the uncertainty of the weather?

Highlight KALLA working group:

Liquid metals are tested as heat transfer fluids in concentrating solar power systems in the SOMMER test facility (Fig. 1) at Karlsruhe Liquid Metal Laboratory KALLA. The excellent heat transfer properties of liquid metals allow building more compact and efficient receivers. The thermal receiver tubes in the focal point, which are heated by the concentrated solar power, can be cooled more efficiently than with the currently used molten salt mixture. In the SOMMER loop, the liquid lead-bismuth eutectic (LBE) is pumped through the spiral thermal receiver and is afterwards cooled down in an air cooler to enter the pump again. In 2019, experiments under sunlight conditions with heat flux densities of up to 4 MW/m² have been successfully performed in the SOMMER test facility. It was demonstrated that liquid metal can be handled under varying conditions and can efficiently cool the receiver pipes at extremely high heat flux densities.

Figure 5: SOMMER test facility; left: parabolic mirror; right: liquid metal loop with thermal receiver in the focal point (Foto: F. Fellmoser)

Hydrogen from Natural gas without CO2 Emissions

Figure 6: Methane pyrolysis by means of a bubble column reactor allows for the climate-friendly use of fossil natural gas.

In the current energy debate, hydrogen is increasingly considered a key to the success of the energy transition. Hydrogen is a clean source of energy and can be used for the production of electricity and heat and in the mobility sector or in industrial processes, such as for the production of steel. Experts of the International Energy Agency IEA calculated that admixture of 20% of hydrogen in the European gas grid could reduce CO_2 emissions by 60 million tons per year. This corresponds to about the amount emitted by Denmark in a whole year.

Direct thermal cracking of methane and other hydrocarbons can be a way to produce hydrogen from natural gas without direct CO_2 emissions. For this purpose, the KALLA team, in cooperation with the Institute for Advanced Sustainability Studies e.V. in Potsdam, started developing a process for the continuous decomposition of methane in a bubble column reactor filled with liquid metal to produce hydrogen and solid carbon some years ago. They continued research on the technology over the last years and have entered into a joint project with the industry partner WintershallDea in 2019, to further advance this technology towards use in industry.

Highlight SAR-group: JIMEC experiments for the EU-Project ESFR-SMART

To increase public acceptance of nuclear power in Europe and secure its future role, the significantly higher safety of new reactors compared to traditional reactors has to be demonstrated. The 4-year ESFR-SMART project (European Sodium Fast Reactor Safety Measures Assessment and Research Tools), launched in September 2017 aims to enhance the safety of Generation-IV Sodium Fast Reactors (SFR), in particular the commercial-size European Sodium Fast Reactor (ESFR).

In course of a less probable accident that a corium pool builds up in the core region, dedicated corium relocation measures with Corium Transfer Tubes will minimise the core melt mass in the core region to avoid recriticality.

A great safety concern in this case is the impingement of a high-temperature and high-momentum corium jet on the metallic core catcher material. Although both oxide corium and metallic corium can be relocated, metallic corium is considered to be more crucial on the core catcher ablation process due to its low solidifying temperature and therefore the less potential to build up a protecting crust layer.

The JIMEC (Jet Impingement on Metallic Core-catcher) tests performed by the Severe Accident Group (SAR) of IKET provided prototypical experimental data to quantify the risk. JIMEC tests are designed firstly to create a metallic jet with stainless steel composition and with designed superheat and fall height; and secondly to record the ablation process of a 40 cm thick substrate of the same material composition as the jet. The mass of the metallic melt is 1000 kg, and the jet velocity at the substrate surface is about 5 m/s.

The prototypical test data provided insights to a wide application range within and also beyond the nuclear safety research.

The main conclusion of the experiments is that the ablation process slows down after the melt

jet mass was firstly retained in the molten pool inside the ablated pit. The ablation velocity before and after this event was constant with an ablation velocity of less than 2 cm/s before and slowed down afterwards to less than 1 cm/s. This effect could be called "pool effect", which means that the deep melt pool prevents the direct energetic contact of the melt at the pit bottom.
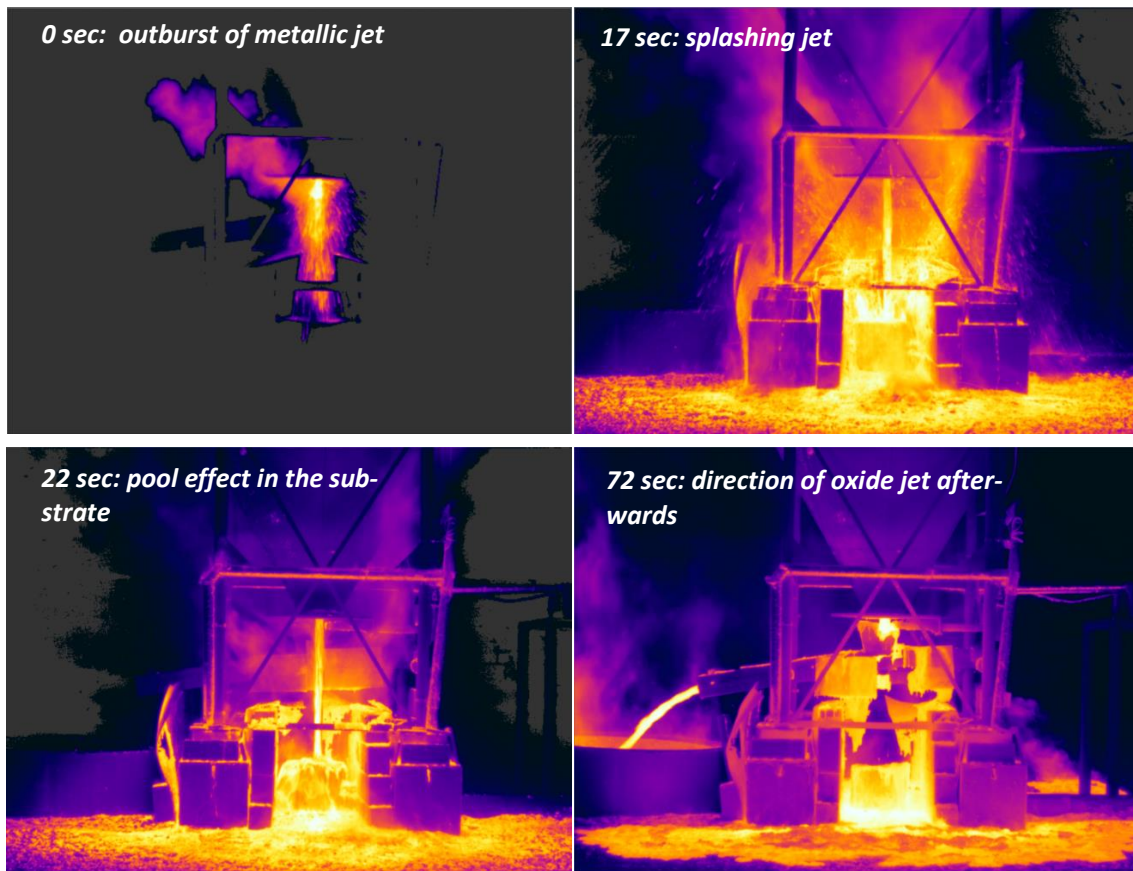

Figure 7: shows the impingement of a 40 mm diameter steel jet on a steel substrate: on the top, the jet has direct contact with the substrate during the initial period, while at the bottom, the jet falls into a molten pool and reduces its ablation effect after a certain depth reached in the ablated pit

.

Group: Magnetohydrodynamics

Magnetohydrodynamics for liquid-metal blankets

L. Bühler, H.-J. Brinkmann, C. Courtessole, V. Klüber, C. Köhly, C. Mistrangelo

Introduction

Liquid metal blanket concepts foreseen in a DEMOnstration nuclear fusion reactor or as test blanket modules (TBM) in the experimental reactor ITER use the lead lithium alloy PbLi as breeder, neutron multiplier, neutron shield and as coolant to remove the volumetrically generated heat. The movement of the electrically conducting fluid in the strong magnetic field induces electric currents responsible for strong Lorentz forces, high magnetohydrodynamic (MHD) pressure drop with implications on heat and mass transfer. The physical parameters characterizing the MHD flow are the Hartmann number and the Reynolds number,

$$Ha = BL\sqrt{\frac{\sigma}{\rho\nu}}, \quad Re = \frac{u_0 L}{\nu},$$

where B, L and u_0 denote magnetic field, typical length scale and velocity. The fluid properties are the density ρ, kinematic viscosity ν and electric conductivity σ. Ha^2 und Re stand for the ratio of electromagnetic to viscous forces and inertia to viscous forces, respectively. For problems, where buoyancy forces are important, the latter ones are quantified by the Grashof number

$$Gr = \frac{g\beta\Delta T L^3}{\nu^2},$$

where ΔT is a typical temperature difference, g stands for gravity and β is the thermal expansion coefficient of the liquid metal.

The MHD work at IKET KIT supports blanket engineering activities of the EUROfusion consortium and the test blanket program of Fusion For Energy (F4E) for ITER.

Numerical simulations for liquid metal MHD flows

Optimum grids for MHD simulations

Phenomena imposed by high transverse magnetic fields result in strong electric current density and steep gradients of velocity across extremely thin boundary layers. The later have to be spatially well resolved in numerical simulations since they determine essentially the flow in the entire duct. In contrast, the flow in the core shows only moderate or small gradients so that this part of the flow could be simulated with coarser grids. Computational grids based on cubic cells are favorable for finite-volume calculations of MHD flows in rectangular ducts. As shown in Figure 1, by stretching and compressing the grid independently in both transversal directions, block structured cells adapt perfectly to the duct geometry, while preserving a structural order, that benefits to numerical consistency.
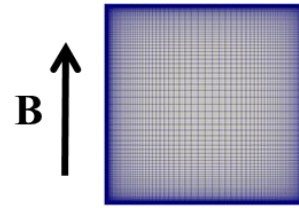
Figure 1: Computational grid for cross section of a rectangular duct MHD flow.

For more complex geometries block-structured grids might not be an optimal choice. Ongoing investigations therefore address the application of unstructured grids for simulations with an in-house-developed MHD code based on the finite-volume library OpenFOAM [1]. One example discussed in the following is the well-known MHD flow in an electrically insulating circular pipe.
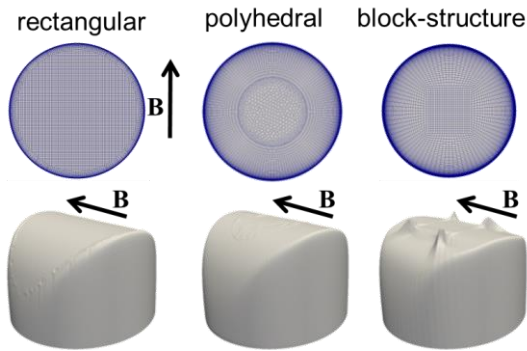
Figure 2: Three grid types for pipe flow and their respective impact on axial MHD velocity profiles (lower row).

Figure 2 shows different types of grids together with their resulting velocity profiles. All grids use hexahedral prisms in order to resolve thin boundary layers, while using rectangular, polyhedral or a block structure in the core. Rectangular and polyhedral based meshes show correct MHD velocity profiles for circular pipe flow. We observe only minor ripples at positions with locally unstructured cells. The block-structured configuration (standard O-grid), however, exhibits large singularities emerging from the corners of the quadratic central core grid. These strong perturbations propagate along grid lines into the fluid. This seems to be an intrinsic problem in finite volume calculations as reported in [1] and [2]. According to [3], locations of slope discontinuity, which are characteristic for the block-structured O-grids, lead to zero order errors, independent of the mesh refinement level. Computations of MHD flows and in particular, the strong coupling of hydrodynamic and electrodynamic phenomena amplifies this effect additionally. Consequently, rectangular or polyhedral grids should be the preferred choice for simulations of MHD flows in complex geometries.

3D MHD flows in fusion blankets

The dual coolant lead lithium (DCLL) blanket is one concept investigated in the frame of EU-ROfusion [4]. In the proposed design, PbLi serves as breeder and as coolant. Since the liquid metal flows at sufficiently large velocity

for efficient heat removal, pressure losses related to the occurrence of electromagnetic forces become significant. Magnetohydro-dynamic effects are coupled with thermal phenomena caused by the occurrence of temperature gradients in the fluid due to the presence of a volumetric neutronic heat load.

In order to reduce MHD pressure drop it has been proposed to use insulating flow channel inserts (FCI) to electrically decouple the PbLi flow from the well-conducting walls. Sandwich-type FCIs are considered as a feasible technical option [4] [5] [6] and their electrical conductivity (of the inner protecting sheet) has been taken into account in numerical simulations.
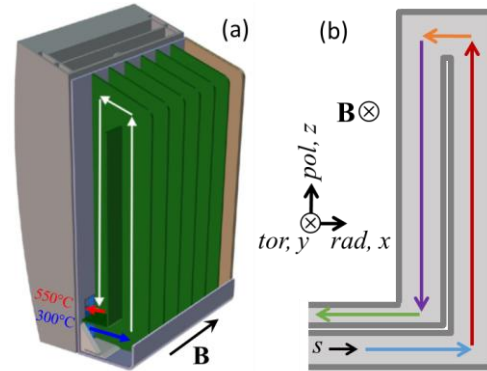
Figure 3: (a) Design of DCLL blanket module. (b) Model geometry for the numerical study.

From Figure 3, it can be noticed that the main characteristic geometric elements of a module area vertical rectangular ducts. Initial numerical simulations for pressure driven flow have been complemented by new 3D calculations for mixed convection of PbLi in the presence of a strong toroidal magnetic field. The flow is driven by an external pressure gradient and by buoyancy associated with the volumetric heating caused by neutrons. A model problem for mixed magneto-convective flow is considered, where a uniform volumetric heat source q in the fluid is assumed. The characteristic temperature difference is related to this heat source as $\Delta T = qL^2/k$, where k stands for the thermal conductivity of the liquid metal. At the entrance, the MHD flow is fully developed and

isothermal. In the inlet duct and in the entire blanket module, the fluid heats up along the flow path as a result of the volumetric heating.

Figure 4 shows results for mixed convection flow at Re= 8596, $Ha = 500$ and $Gr = 10^9$. The temperature distribution on the middle plane at $y = 0$ shows that a high-temperature region is present on the top of the module and in the upper part of the "downward" duct. Streamlines and contours of velocity magnitude depicted in the figure indicate the presence in the rear channel of a descending jet that moves downstream along the internal vertical wall that separates the two poloidal channels. Here the fluid is colder and therefore, due to its higher density, it tends to flow downwards. The downward jet is unstable and this may affect mixing and the heat transfer.

Figure 4: Results for $Re = 8596$ $Ha = 500$ and $Gr = 10^9$ on the plane $y = 0$; (a) contours of temperature and velocity streamlines; (b) contours of velocity magnitude.

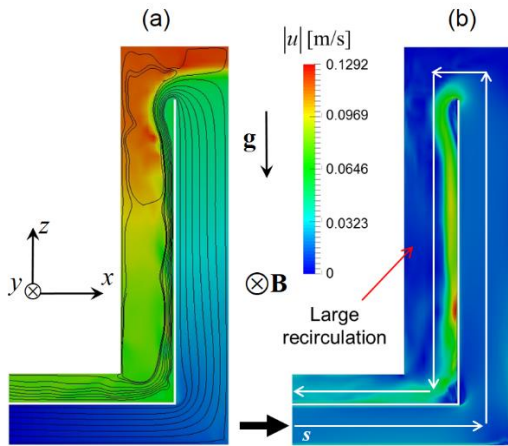Velocity profiles for forced and mixed convection at $Ha = 500$ and $Re = 8596$ are shown in Figure 5 for $Gr = 0$ and $Gr = 10^9$, respectively. The intensity of the downward jet flow at the internal wall can be seen. More details can be found in [7] [8]. Results for magneto convection in geometries related to water cooled lead lithium WCLL blankets are described in [9].
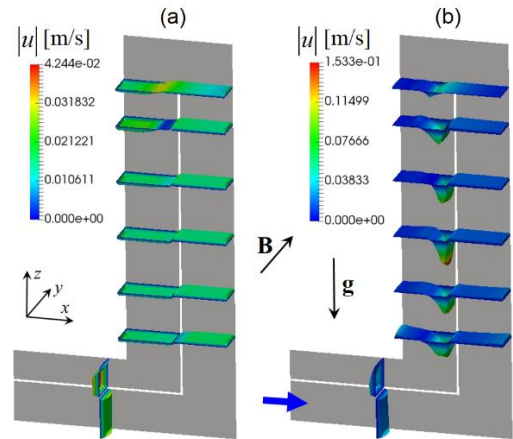
Figure 5: Velocity distributions at different positions along the flow path for MHD flow at $Ha = 500$, $Re = 8596$ for (a) isothermal flow $Gr = 0$, (b) magneto convection at $Gr = 10^9$.

Experimental study of liquid metal MHD flows at the entrance of FCIs

MHD pressure drop in ducts of fusion blankets results from the interaction of flow-induced electric currents with the plasma-confining magnetic field. The highest pressure drop in the flow is observed, when currents shortcut along the thick conducting blanket walls. For reduction of pressure drop, electrically insulating flow channel inserts (FCIs) are foreseen for electrically decoupling the liquid metal flow from the well-conducting channel walls. The preferred option for near-term applications in fusion blankets are sandwich-type FCIs, where the insulating ceramic material is protected from direct contact with the liquid metal by thin sheets of steel. For experimental investigations of 3D effects at the entrance into FCIs and at junctions between two FCIs, a test section has been manufactured and experiments have been performed in the MEKKA facility [10] using NaK as model fluid. The fabrication of FCIs for circular pipes required development of new fabrication strategies [6], since the technology proposed for rectangular ducts [5] did not apply. The experimental study shows the benefits of FCIs for pressure drop reduction in fully developed flows as predicted by theoretical analyses [11] and confirmed by experiments [12].

Details of the experimental test section are shown in Figure 6. The thickness $t_{FCI} = 0.5mm$ of the protection sheets has been suggested e.g. in [13]. The coordinate $x = 0$ corresponds to the position of the pressure tap that is located immediately in front of the FCI. As shown in Figure 6 and Figure 7, the FCI starts at $x = 5mm$ and the insulation inside the FCI at $x_i = 10mm$.

3D perturbations that occur when the flow enters the magnet decay quickly along the flow path as shown in previous investigations [14]. Therefore, the MHD pipe flow is fully developed before the fluid approaches the FCI. In the experiments, pressure and electric potential differences have been recorded and some typical results are discussed in the following.
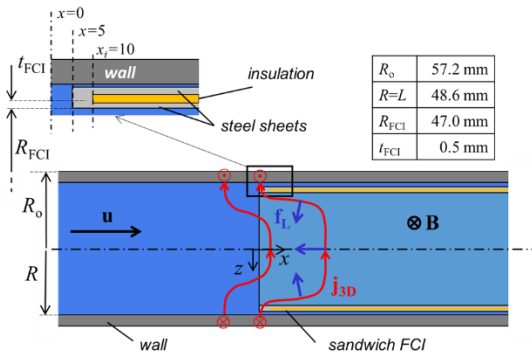
Figure 6: Geometry and principle sketch of current paths at the entrance of a FCI. The insulation inside the FCI starts at $x_i = 10mm$.

In experiments it is possible to observe a potential difference between both sides of the pipe $\Delta\phi = \phi\left(\alpha = -\frac{\pi}{2}\right) - \phi\left(\alpha = \frac{\pi}{2}\right)$. This quantity is used in the following to investigate the influence of 3D MHD effects at the entrance of the FCI. When potential results are scaled by characteristic values u_0BL, all curves collapse onto a single line as displayed in Figure 8, confirming the universal scaling law for potential over a wide range of Hartmann numbers investigated. Potential values are proportional to the strength of the applied magnetic field and the fluid velocity.

Far upstream, $\Delta\phi(x/L < -2)$ shows fully established conditions with uniform values along x in good agreement with theoretical predictions for fully developed MHD pipe flow [15]. Approaching the FCI, the potential starts monotonically decreasing. At downstream positions, where current paths into the wall are interrupted by the insulation of the FCI, values of $\Delta\phi(x/L)$ decay to zero. We observe that 3D effects, caused by recirculating currents inside the wall near the entrance of the FCI, extend upstream over more than $2L$ and downstream up to $5L$. The currents flowing in the downstream part of the wall are separated from those inside the fluid by the insulation in the FCI. The fact that $\Delta\phi$ vanishes as $x/L > 5$ confirms full functionality of the ceramic insulation inside the sandwich FCI.

Figure 7: Sketch of FCI position in pipe. The insulating layer inside the FCI (not visible in the sketch) begins at a downstream position of $x_i = 10mm$.

Figure 8: Variation of nondimensional transverse potential difference near the entrance of the FCI.

Pressure differences along the pipe and along the FCI entrance region have been measured for various values of flow rate and for different s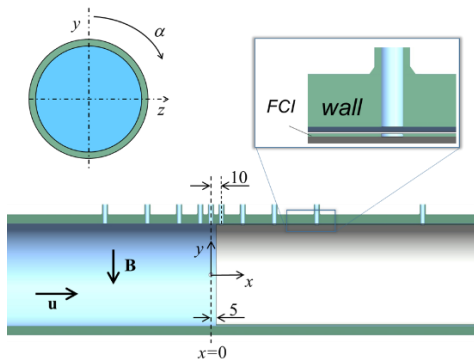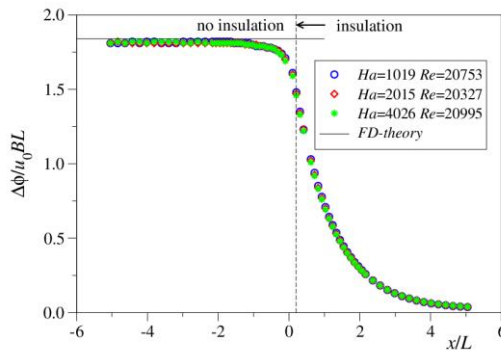trengths of the magnetic field. The reference value of pressure has been placed at position $x = x_i$, i.e. $p(x_i) = 0$. When scaled with characteristic quantities $\sigma u_0 B^2 L$, all results come close to a single line as shown in Figure 9. We observe a fast decay of pressure in the bare pipe without insulation and a slower decrease of pressure in the insulated region.
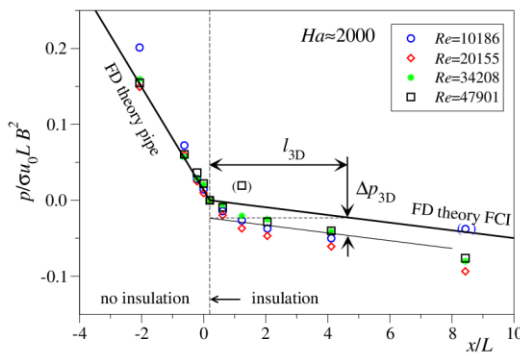

Figure 9: Nondimensional pressure along the axis for $Ha = 2000$ and different.

The pressure gradients in the bare pipe and in the part with FCI agree well with theoretical predictions [16] as indicated by the black solid lines in Figure 9. The FCI reduces the pressure gradient by a factor of about 13.3 compared to the value in the non-insulated pipe. Nevertheless, recirculating additional currents near the entrance of the FCI give rise to extra Lorentz forces that create some additional pressure drop Δp_{3D} caused by 3D effects. Even if the absolute value of Δp_{3D} appears acceptable one should keep in mind that it corresponds to a pressure drop in an ideal long FCI over more than 4 characteristic lengths L. Since similar pressure losses occur also at the exit of the FCI or at gaps between two FCIs [12], these 3D effects reduce the efficiency of FCIs by an amount that is not negligible. For stronger magnetic fields, i.e. higher Hartmann numbers, the behavior is similar. More details can be found in [17].

Design of a MHD mockup experiment of a water cooled lead lithium TBM for ITER

Another concept for an ITER TBM is the water cooled lead lithium (WCLL) blanket [18], where PbLi is employed as breeder and neutron multiplier. Pressurized water cools the first wall and breeding zone (BZ), and EUROFER steel is used as structural material [19]. The design of the WCLL TBM consists of 16 breeder units (BU) arranged in two columns with a complex structure of PbLi and water manifolds (see Figure 10). A system of water cooling pipes placed inside BUs removes the heat generated in the liquid metal. These water pipes are crossing the PbLi manifolds, and they occupy a significant fraction of the manifold cross section. In addition, stiffening plates inside the PbLi manifolds lead to repeated reduction of the cross section and redirect locally the liquid metal flow. The meandering and constricted flow paths increase the PbLi velocity and pressure drop in the manifolds.
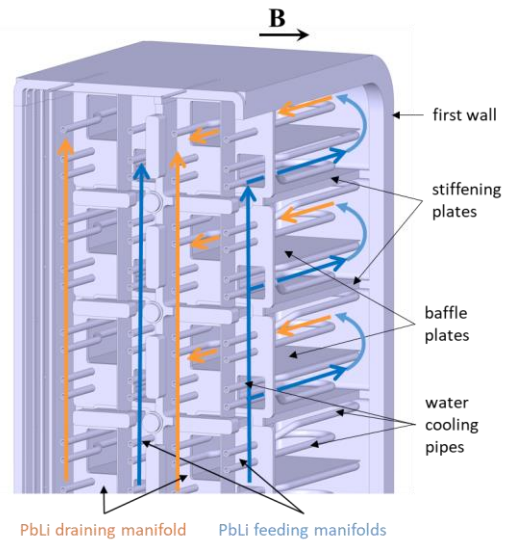

Figure 10: Design of the WCLL TBM as provided by CEA [18]. View on details such as liquid metal manifolds, water pipes, breeder units, baffle plates and stiffening plates.

Objective of the planned experiments is to achieve knowledge about pressure drop in the TBM of the WCLL blanket and to determine the

distribution of the PbLi flow from the manifold into the breeder units. With the aim to investigate the liquid metal flow in a blanket geometry that is most realistic and comparable to the original concept foreseen for ITER, a scaled MHD mockup has been designed on basis of the present WCLL TBM design [18]. In order to achieve high Hartmann numbers in a range relevant for the application, the mockup geometry should be as large as possible. Nevertheless, the mockup has to fit into the gap of the magnet available at the MEKKA facility. To keep the geometry as close as possible to the real design and as large as possible, one column of 8 BUs with distributing and collecting manifolds is considered. With a scale of 1:2.5, such a model geometry fits well into the magnet. It has all geometric features and details, which are necessary for performing meaningful MHD experiments.

For the experiments in the MEKKA laboratory, the WCLL mockup will be embedded with horizontal orientation into the magnet. Figure 11 shows a transparent view of the mockup for visualization of the PbLi flow path showing the main dimensions. The liquid metal is fed into the mock up and removed from it through circular pipes, which are connected to the existing loop in the laboratory. The PbLi is distributed and collected by two manifolds into and out of the BUs. Each BU is fed through a small window in the back wall of the manifolds. The PbLi flow is redirected at the first wall and guided back into the outlet manifold.
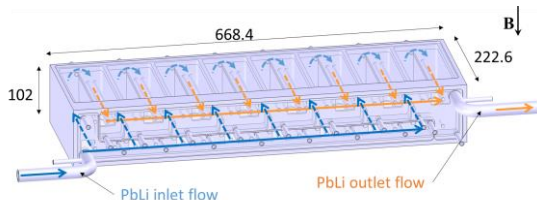
Figure 11: Transparent view of the WCLL MHD mockup design with main dimensions (in mm) and indicated PbLi flow paths.

The WCLL TBM mockup has been simplified to meet manufacturing concerns and to reduce fabrication costs, while keeping the geometry for the liquid metal flow as foreseen in [18]. The test section has been designed with the objective to reduce the number of parts and the number of welds, respectively. An optimized and well-placed number of electron beam welds minimizes welding distortions. Costs for fabrication remain moderate due to the low number of welds.

Details concerning the water flow inside the blanket walls have been omitted since it is expected that they will not affect the liquid metal flow. Water pipes, representing a partial blockage for the liquid metal flow in the manifolds are all present in the mockup.

An exploded view of the mockup in Figure 12 shows the major parts. The main body consists of a single piece, which forms the walls of all BUs, including first wall, stiffening plates, back plate and walls separating the two inlet and outlet manifolds for the PbLi flow. The breeder units are closed from both sides and the manifold is closed by two back plates. The water pipes blocking part of the liquid metal domain are simulated by dummy parts of solid material. All parts are made of 1.4571 austenitic steel that has good compatibility with the used model fluid NaK, and does practically not disturb of the magnetic field.
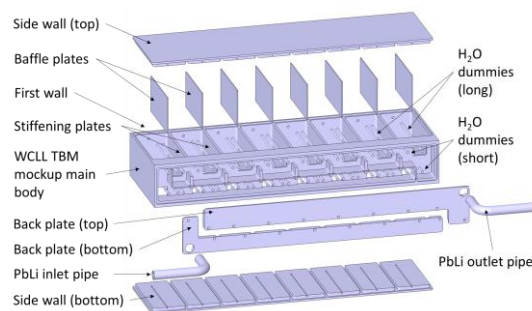
Figure 12: Exploded view of the WCLL MHD mockup with major components: main body, top and bottom walls, back plates as cover for the manifolds, and dummy parts that mimic the water pipes.

Pressure differences will be measured between several points of the mockup using a piping system between pressure taps and the

pressure transducers. The transducers are located outside of the magnet. The piping system is connected with an array of 30 computer-switched valves, which control the measuring sequence. To avoid additional pipes for draining and venting during the filling and emptying process, the positions of the pressure taps have been chosen to also satisfy the function of feeding, draining and venting. They are located at the lowest and highest positions of each breeding unit in the breeding zones and manifolds (see Figure 13).
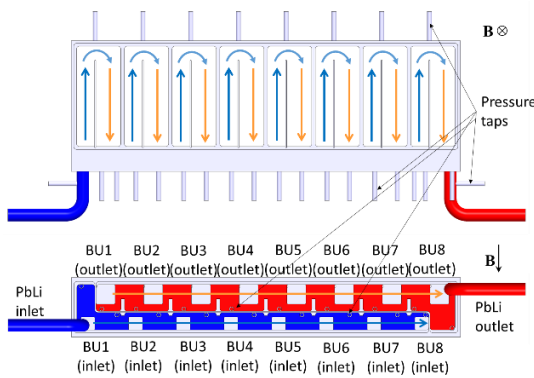

Figure 13: Connections with liquid metal loop and location of pressure taps.

The aim of the planned experiment is to assess MHD pressure losses when the liquid metal passes around obstacles (pipes) and through contractions and expansions. Flows in different parts of the module are electrically coupled since currents induced in one part may leak across electrically conducting walls into neighboring channels. Electromagnetic flow coupling and flow partitioning among BUs is investigated by measurements of the electric potential distribution on the walls.

First experiments in a test section related to magneto-convection in water-cooled lead lithium blankets

The numerous cooling tubes immersed in the liquid metal of a WCLL blanket module create large temperature gradients such that the liquid metal flow, which is partially obstructed by these obstacles, results from the combined interaction of electromagnetic force, buoyancy, and pressure gradient. To improve the understanding of magneto-convective flows, a simplified mockup is used to study buoyant MHD flows in cavities with internal obstacles and to provide a first experimental database for MHD flows with heat transfer in a WCLL-like geometry.
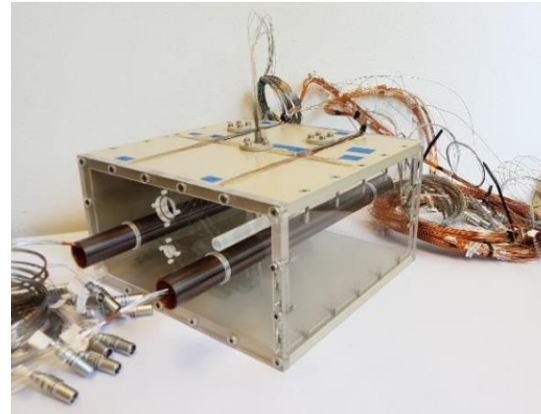
Figure 14: Instrumented test section with transparent walls for preliminary water experiments.

The experimental test section is shown in Figure 14. It was designed to be used with GaInSn as a model fluid and to fit within the gap of the electromagnet present in the MEKKA laboratory. It consists of a rectangular box made of PEEK plastic through which two parallel copper pipes serving as a heat source and a heat sink are inserted. Each pipe is connected to its own temperature-controlled circuit such that they can be kept at constant temperatures T_1 and T_2 during the experiments. This set-up provides the necessary differential heating to establish a horizontal temperature gradient that drives the buoyant flow. The pipes are coated with a 2 μm layer of silicon carbide to electrically insulate the copper from the liquid metal and protect them from corrosion. The test section is fully instrumented to record simultaneously local velocities, electric potential at the walls and temperature at several locations in the fluid. In particular, the temperature distribution in the center of the cavity is measured by

an 11-point thermocouple probe uniformly distributed across the height of the box. Further details are given in [20].

Before proceeding with the liquid metal experimental campaign, preliminary experiments have been performed with water to test the instrumentation and to obtain results for the hydrodynamic limit where no magnet field is applied. Besides, using a transparent medium also enables full flow visualization by optical techniques. For that purpose, two walls of the box were replaced by Plexiglas panels and the water was seeded with fluorescent tracers so that Particle Image Velocimetry can be applied (Figure 15).
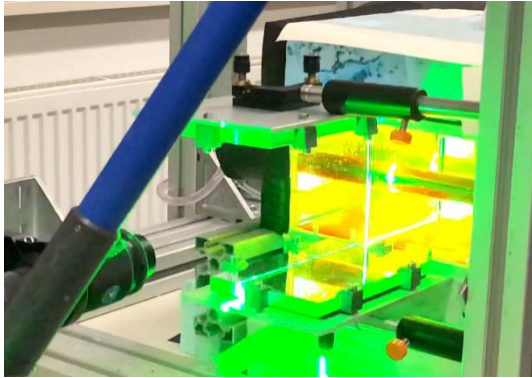
Figure 15: Laser sheet produced by a Nd:YAG laser illuminating the test section during PIV measurements.

Experiments have been performed at various temperature difference $\Delta T = T_2 - T_1$ imposed between the pipes. Results obtained show that the buoyant flow results in a thermal stratification with the hot fluid staying on the top and the cold fluid on the bottom as seen on the dimensionless temperature profiles measured at the central probe and plotted in Figure 16.

$$T^* = \frac{T - \bar{T}}{\Delta T / 2} \, .$$
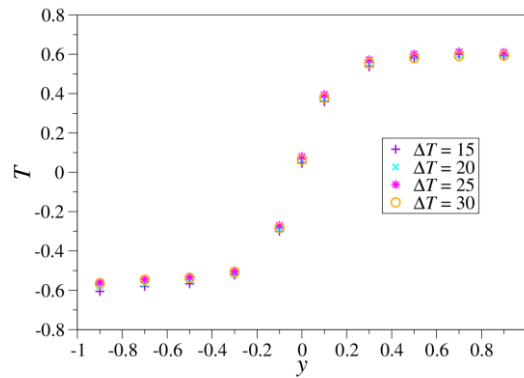
Figure 16: Non-dimensional temperature profile measured at the center of the cavity.

After finishing the preliminary water campaign, the test section will be filled with liquid metal and placed in the magnet to perform experiments for various magnetic fields and temperature differences.

Further work

In addition to the topics described above, the MHD group at IKET KIT contributed in the reporting period 2019 with scientific papers to the development of fusion technology [21] [22] and to fundamental studies of MHD flows [23] [24] [25] [26] [27] [28] [29].

References

[1] Mistrangelo C. and Bühler L.; "Development of a numerical tool to simulate magneto-hydrodynamic interactions of liquid metals with strong applied magnetic fields," Fusion Science and Technology, vol. 60, no. 2, pp. 798-803, 2011.

[2] Vantieghem S.; Albets-Chico X. and Knaepen B.; "The velocity profile of laminar MHD flows in circular conducting pipes," Theoretical and Computational Fluid Dynamics, vol. 23, no. 6, pp. 525-533, 2009.

[3]   Moukalled, F.; Mangani L. and Darwish M.; The Finite Volume Method in Computational Fluid Dynamics, vol. 113, Springer, 2016.

[4]   Rapisarda, D.; Consolidated design of the low temperature EU-DCLL, Presentation at 27th IEEE Symposium On Fusion Engineering (SOFE). 6 June, 2017.

[5]   Norajitra, P.; Basuki, W. W.; Gonzalez, M.; Rapisarda, D.; Rohde, M. and Spatafora, L.; "Development of sandwich flow channel inserts for an EU DEMO dual coolant blanket concept," Fusion Science & Technology, vol. 68, no. 3, pp. 501-506, 2015.

[6]   Koehly, C. and Bühler, L.; "Fabrication issues of sandwich-like flow channel inserts for circular pipes," Fusion Science and Technology, vol. 72, pp. 660-666, 2017.

[7]   Mistrangelo, C.; Büher, L. and Klüber, V.; "Three dimensional magneto convective flows in geometries relevant for DCLL blankets," in 14th International Symposium on Fusion Nuclear Technology, in Budapest, Hungary, September 22- 27, 2019.

[8]   Klüber, V. ; Bühler, L. and Mistrangelo, C.; "Numerical simulations of 3D magnetohydrodynamic flows in dual-coolant lead lithium blankets," Fusion Engineering and Design, vol. 146, pp. 684-687, 2019.

[9]   Mistrangelo, C.; Bühler, L. and Koehly, C.; "Considerations on magneto-convective flows in model geometries relevant for fusion applications," in Proceedings of the 11th International PAMIR Conference - Fundamental and Applied MHD, July 01 - 05, 2019, Reims, France, 2019.

[10]   Barleon, L. ; Mack, K.-J. and Stieglitz, R.; "The MEKKA-facility a flexible tool to investigate MHD-flow phenomena," 1996.

[11]   Bühler, L. and Mistrangelo, C.; "Pressure drop and velocity changes in MHD pipe flows due to a local interruption of the

insulation," Fusion Engineering and Design, vol. 127, pp. 185-191, 2018.

[12]   Bühler, L.; Brinkmann, H.-J. and Koehly, C.; "Experimental study of liquid metal magnetohydrodynamic flows near gaps between flow channel inserts," Fusion Engineering and Design, vol. 146, pp. 1399-1402, 2019.

[13]   Urgorri, F.; Smolentsev, S.; Fernandez-Berceruelo, I.; Rapisarda, D.; Palermo, I. and Ibarra, A.; "Magnetohydrodynamic and thermal analysis of PbLi flows in poloidal channels with flow channel insert for the EU-DCLL blanket," Nuclear Fusion, vol. 58, no. 10, p. 106001, 2018.

[14]   Bühler, L.; Brinkmann, H.-J. and Mistrangelo, C.; "Experimental investigation of liquid metal pipe flow in a strong non-uniform magnetic field," in Proceedings of the 11th International PAMIR Conference - Fundamental and Applied MHD, July 01 - 05, 2019, Reims, France, 2019.

[15]   Miyazaki, K.; Kotake, S.; Yamaoka, N.; Inoue, S. and Fujii-E, Y.; "MHD pressure drop of NaK flow in stainless steel pipe," Nuclear Technology/Fusion, vol. 4, pp. 447-452, 1983.

[16]   Miyazaki, V; Konishi, K. and Inoue, S.; "MHD pressure prop of liquid metal flow in circular duct under variable transverse magnetic field," Journal of Nuclear Science and Technology, vol. 28, no. 2, pp. 159-161, 1991.

[17]   Bühler, L.; Mistrangelo, C. and Brinkmann, H.-J.; "Experimental investigation of liquid metal MHD flow entering a flow channel insert," Fusion Engineering and Design, vol. 154, p. 111484, 2020.

[18]   Batal, T.; Assembly of WCLL TBM: CAD product and parts (by CEA)., personal communication November 27, 2019.

[19]   Tassone, A.; Nevo, A. D.; Arena, P.; Bongiovì, G.; Caruso, G.; di Maio, P. A.; di

Gironimo, G.; Eboli, V.; Forgione, N.; Forte, R.; Giannetti, F.; Mariano, G.; Martelli, E.; Moro, F.; Mozzillo, R.; Tarallo, A. and Villari, R.; "Recent Progress in the WCLL Breeding Blanket Design for the DEMO Fusion Reactor," IEEE Transactions on Plasma Science, vol. 46, no. 5, pp. 1446-1457, 2018.

[20]   Koehly, C.; Bühler, L. and Mistrangelo, C.; "Design of a test section to analyze magneto-convection effects in WCLL blankets," Fusion Science and Technology, vol. 75, pp. 1010-1015, 2019.

[21]   Utili, M.; Bassini, S.; Boccaccini, L.; Bühler, L.; Cismondi, F.; Nevo, A. D;. Eboli, M.; DiFonzo, F.; Hernandez, T.; Wulf, S.; Kordac, M.; Martelli, D.; les Valls, E. M. D;. Melichar, T.; Mistrangelo, C.; Tarantino, M.; Tincani, A. and Vala, L.; "Status of Pb-16Li technologies for European DEMO fusion reactor," Fusion Engineering and Design, vol. 146, pp. 2676-2681, 2019.

[22]   Bühler, L.; Mistrangelo, C. and Brinkmann, H.-J.; "Experimental investigation of liquid metal MHD flow entering a flow channel insert," in 14th International Symposium on Fusion Nuclear Technology, in Budapest, Hungary, September 22- 27, 2019.

[23]   Klüber, V.; Mistrangelo, C. and Bühler, L.; "Numerical investigation of liquid metal MHD flow in rectangular channels under inclined magnetic fields for fusion relevant parameters," in Proceedings of the 11th International PAMIR Conference - Fundamental and Applied MHD, July 01 - 05, 2019, Reims, France, 2019.

[24]   Klüber, V.; Mistrangelo, C. and Bühler, L.; "Numerical investigation of liquid metal MHD flow in rectangular channels under inclined magnetic fields for fusion relevant parameters," Magnetohydrodynamics, p. submitted, 2020.

[25]   Klüber, V.; Mistrangelo, C. and Bühler, L.; "Numerical simulation of 3D magne-tohydrodynamic liquid metal flow in a spatially

varying solenoidal magnetic field," in 14th International Symposium on Fusion Nuclear Technology, in Budapest, Hungary, September 22- 27, 2019.

[26]   Klüber, V.; Mistrangelo, C. and Bühler, L.; "Numerical simulation of 3D magne-ohydrodynamic liquid metal flow in a spatially varying solenoidal magnetic field," Fusion Engineering and Design, p. accepted, 2020.

[27]   Bühler, L.; Brinkmann, H.-J. and Mistrangelo, C.; "Experimental investigation of liquid metal pipe flow in a strong non-uniform magnetic field," Magnetohydrodynamics, p. submitted, 2020.

[28]   Arlt, T. and Bühler, L.; "Numerical simulation of time-dependent Hunt flows with finite wall conductivity," Magneto-hydrodynamics, vol. 55, no. 3, pp. 319-336, 2019.

[29]   Smolentsev, S.; Rhodes, T.; Yan, Y.; Tassone, A.; Mistrangelo, C.; Bühler, L. and Urgorri, C. M. F. R.; "Code-to-code comparison for a PbLi mixed-convection MHD flow," Fusion Science and Technology, p. submitted, 2020.

Group: Transmutation

3-D Simulation of Fuel Assembly Blockage in MYRRHA

Xue-Nong Chen*, Andrei Rineiski

Abstract

In the framework of the KIT and SCK•CEN R&D cooperation and as continuation of earlier studies performed for the EURATOM FP7 MAXSIMA project, accidental transients caused by a single fuel assembly (FA) blockage were simulated with the SIMMER-IV (3-D) code for the MYRRHA core, while assuming no power variation during the accident. A 7-FA model that includes mesh cells for inter-wrapper gaps between FAs was applied, with the blockage of the central FA. Sensitivity analyses on the gap flow rate, fuel chunk jamming fraction, insulator pellet material were performed in order to identify a conservative case that maximises the chance of damage propagation from the blocked FA to the neighbouring ones. All calculations with different options and parameters did show the same sequence in the blocked FA, including melting of pin cladding, fuel pellet failure, small can-wall break-up, steel particle and fuel chunk accumulation leading to additional blockages, and large can-wall break-up. Finally, fuel chunks are swept out from this FA through the inter-wrapper gaps. In the calculations performed for several tens of seconds and longer, no canwall break-up in the neighbouring FAs has been observed. Nevertheless, different options for simulation of the insulator break-up lead to significantly different results in the later phases of calculations. If the insulator pellet breaks up when the cladding is lost, a fuel/steel blockage is formed, which results in a large canwall break-up, but this blockage is dissolved as soon as the upper steel structure melts. If no insulator pellet breaks-up, the fuel/steel blockage is kept in place by the ceramic insulator, which has a very high melting temperature. This observation supports the use of an insulating material with low melting temperature; this option may prevent or reduce blockage of fuel/steel particles coming from failed pins that eventually may prevent or reduce the risk of damage propagation to the intact core.

Keywords

Introduction

The MYRRHA reactor designed and developed by the Belgian Nuclear Research Centre (SCK-CEN) was investigated in the European 7th framework project MAXSIMA [1] and earlier projects. The present work is dedicated to analyses of fuel assembly (FA) blockage accidents in MYRRHA studied at KIT in cooperation with SCK-CEN.

SIMMER-III/IV is a two-/three-dimensional, multi-velocity-field, multi-phase, multicomponent, Eulerian, fluid-dynamics code system coupled with a structure model including fuel pins, hexcans, etc., and a space-, time- and energy-dependent transport theory neutron dynamics model [2, 3]. The overall fluid-dynamics solution algorithm is based on a time-factorization approach, in which intra-cell interfacial

area source terms, heat and mass transfers, and the momentum exchange functions are determined separately from inter-cell fluid convection. In addition, an analytical equation-of-state (EOS) model is available to close and complete the fluid-dynamics conservation equations. The code was originally developed and applied for severe accident analyses of fast sodium cooled reactors. However, the philosophy behind the SIMMER development was to generate a versatile and flexible deterministic tool, applicable for the safety analysis of various reactor types with different neutron spectra and coolants, up to the new accelerator driven systems for waste transmutation. In particular, SIMMER was extended at KIT to studies of heavy-metal-cooled, gas-cooled and molten-salt reactors.

The SIMMER IV code, validated by KIT experimental KIT [6], see Fig. 1, was applied for the described studies.
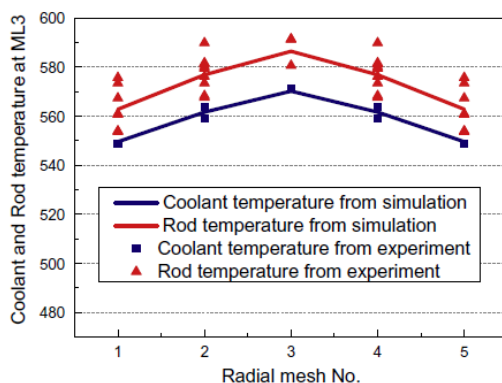

Figure 1: Comparison of the coolant and rod temperatures from SIMMER-IV simulation and experiment [6].

A geometrical model for the chosen 7-FA configuration of a recent design version of the MYRRHA critical reactor has been set up, where the interwrapper gaps have been explicitly taken into account. Central FA blockage accidents are studied, where the configuration of central blocked FA surrounded by other 6 FAs are asymmetric. Results are presented and analysed in this paper.

SIMMER-IV modeling for the 7-FA conficuration

Geometrical Modeling

The coolant flow through gaps (inter-wrapper flow) between FAs cools the FA canwall and therefore can delay or even prevent the FA canwall failure and its propagation. As SIMMER was developed initially for simulations of core disruptive accidents (CDAs) in sodium fast reactor and in simulations of such accidents explicit – i.e. via allocation of special meshes in plane - treatment of gaps between FAs is obviously not important, the the mainly used modelling approach with SIMMER was not to not consider gaps explicitly. However when the SIMMER code is applied to other scenarios than CDAs, the modelling of gaps may reduce the modelling uncertainties. In the past, the gaps were modelled explicitly in a 2D case providing quite different simulation results as compared to the implicit option [4, 5]. Moreover the gaps were explicitly modelled also in 3D with SIMMER-IV for an experimenat case [6]. Due use of the XYZ-geomtery in SIMMER-IV, the hexcan geometry is transformed into a rectangle cubic geometry. Taking 7 FAs as an example, the hexcan geometry could be converted into a rectangular one, as shown in Fig. 2. Each FA has to be divided into 2 parts with suitable parameters. The upper part ''(p)'' contains left, right, and back canwall. The lower part ''(q)'' contains left, right, and the front canwall. Additionally the gaps between the subassemblies need to be explicitly modelled as part ''(r)''. As long as the explicit meshes are set up in the computational system, SIMMER code treats the flow in the gaps with the hydraulic diameter based on the actual geometry, the heat transfer between the canwall (steel) and the flow (LBE) is calculated with the Nussult numbers based on empirical heat transfer correlations.

Power Amplitude and Distributions

The MYRRHA critical core has 108 FAs. 7 FAs have been selected for the study. The selected

7 FAs are numbered and their power peaking factors are indicated in Fig. 3. The selection of the central blocked FA is representative for a heterogeneous combination of subassemblies, with a maximum risk of a local failure of the canwall of the blocked FA. In this case the possible following fuel sweep-out is anisotropic with a high probability of damaging the neighboring FAs. The FA-wise and axial power distributions are imposed on each single assembly according to the reference results [7]. The power is assumed to be constant during the blockage transients. The thermal boundary conditions outside the system are adiabatic.
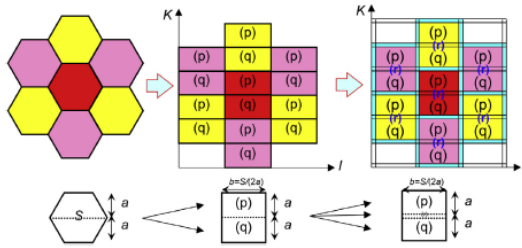

Figure 2: Explicit meshes for gaps flow between subassemblies using SIMMER-IV code.
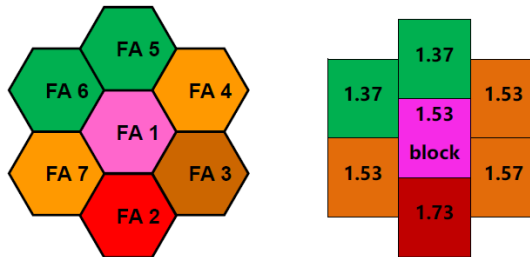
Figure 3: 7 fuel assembly arrangement with power peaking factors

The steady states at the BOC and EOC conditions are quite similar, where only the peaking factors at BOC are slightly higher than those at EOC, mainly due to different axial positions of CRs. Therefore, to be conservative, the BOC condition was used for steady state and transient analyses.

Key steady-state thermohydraulic parameters calculated by SIMMER-IV are calculated for every FA, which match the design values [8]. The coolant inlet temperature is 270 °C. The average thermal power per FA is 0.9259 MW. The pressure boundary conditions are set up and the orifice coefficients for the seven FAs and gaps (in the FA upper position) are adjusted, so that certain coolant flow rates (velocities) are achieved in FAs and gaps respectively. It is noticed that the flows in the gaps are heated up by the can wall.

FA Blockage Transients

FA blockage conditions and parametric studies

The FA blockage is a postulated envelope scenario that evolves from local pin failures which propagate at a FA scale. The blockage is simulated by a reduction of the FA inlet flow rate. Its flow rate is reduced from 72 kg/s to 3.2 kg/s (i.e. 95.6% blockage) for FA1, the central FA, as it is more realistic to assume a porous blockage, allowing a residual cooling flow. The fuel particle diameter is 5.6 mm. For these calculations the fission gas blowout model is deactivated, because we assume, the fission gases contained in the pin gap are all released before the blockage extends to the whole FA flow area.

Different parameters, such as gap velocity, insulator material, particle packing fraction limit in the particle jamming model, and other breakup model options, were employed, some results are given in the following. The reduction of the gap velocity has no signicant effects on the clad melting, but it causes a numerical instability problem. The simulations with different insulator materials as steel and B4C give very similar results. The increase of the particle packing fraction limit shows no significant differences in the calculated results except a slightly earlier canwall breakup and larger particle blockage coefficients.

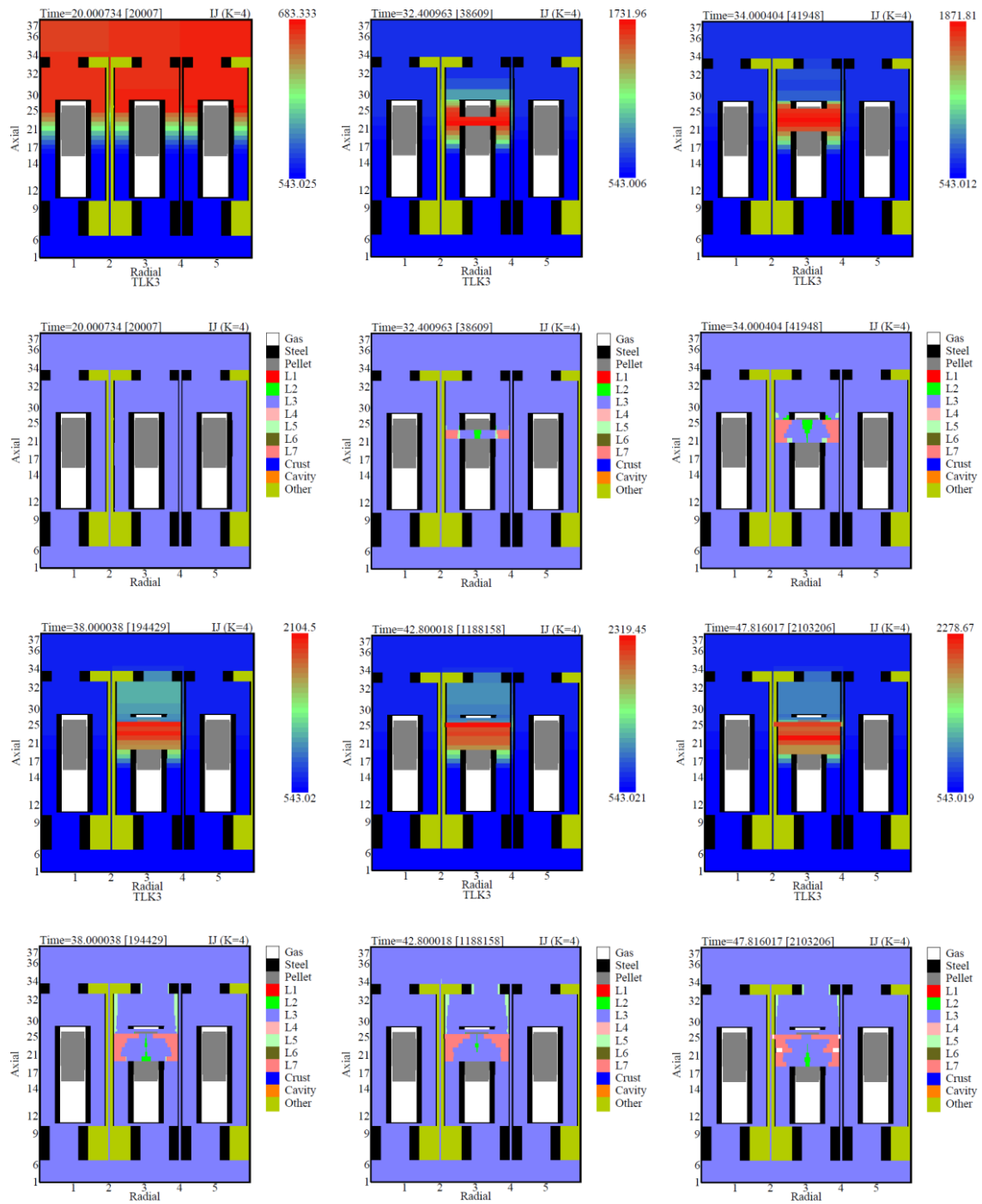Figure 4: Fuel pin breaks up and fuel chunk blockage: coolant temperature TLK3 and material distribution, where L1 liquid fuel, L2 liquid steel, L3 liquid sodium, L4 fuel particle, L5, steel particle, L6 control particle, L7 fuel chunks.

FA blockage transient results in a typical case

In this paper we just present the calculated blockage results in a typical case, i.e. gap velocity = 0.22 m/s, insulator material is B4C, the particle packing fraction limit APJ = 0.8.

Fig. 4 shows the fuel pin breaks up, coolant temperature (TLK3) and material distributions after 20 seconds, the starting time of the blockage. As long as the blockage occurs, the coolant temperature reaches about 1000 °C after less than 10 s. As the cladding temperature reaches the steel melting point limit (1430 °C), the cladding starts to melt. The fuel dispersion starts when the cladding is broken up after 12.4 seconds of instantaneous blockage. A large fuel chunk blockage takes place then aflter 14 seconds at the upper part of the active core. Then the canwall starts to break up after 16.2 seconds. The fuel chunk blockage is not dissolved during the transient calculated. The canwall breakup takes place only at the middle small FA cells. Afterwards, the fuel in this FA escapes from this break-up through the gap to the upper part of the core. No neighboring canwall break-up takes place, i.e. the neighboring FAs stay intact during the transient. Nevertheless, additional blockages in the interwrapper space cannot be excluded, as they cannot be detected with the current model. It is noticed that, if the blockage is a little bit smaller, the canwall in the blocked FA would not break up, thanks to the cooling provided by the flow in gaps, as reported in [9]. This means that the gap flow can prevent the canwall break-up and its break-up propagation.

Conclusions

Calculations with different options and parameters show the same sequences, i.e. the pin melting, the small canwall break-up, fuel/steel particle accumulation and its blockage and the canwall break-up in the blocked FA and finally fuel particle swept out from the blockage FA through the inter-wrapper gaps. The conservative calculations show there is no canwall break-up in the neighboring FAs, even if additional studies need to be carried out to exclude the formation of fuel blockages in the inter-wrapper space. The variation of the maximum packing fraction APJ shows that it has only slight effects on the later sequences of particle blockage, which does not change major results and conclusion. The variation of the interwrapper gap velocity shows that it has some effects on the clad melting time and later sequences.

References

[1]   Baeten, P.; "MYRRHA—Multipurpose hYbrid Research Reactor for High-tech Applications," SEARCH/MAXSIMA 2014 International Workshop, Location, Karlsruhe, Germany, 7-10 Oct. 2014.

[2]   Kondo, S.; Tobita, Y.; Morita, K.; Shirakawa, N.; "SIMMER-III: an advanced computer program for LMFBR severe accident analysis," Proceedings of the International Conference on Design and Safety of Advanced Nuclear Power Plant (ANP'92), vol. IV, Tokyo, Japan, Oct. 25–29, 1992, pp. 40.5.1–40.5.11 (1992).

[3]   Kondo, S.; Yamano, H.; Tobita, Y.; Fujita, S.; Morita, K.; "SIMMER-IV: a Three-Dimensional Computer Program for LMFR Core Disruptive Accident Analysis," Japan Nuclear Cycle, Development Institute, JNCTN9400 (2000).

[4]   Suzuki, T.; Chen, X.-N.; Rineiski, A.; Maschek, W.; "Transient analyses for accelerator driven system PDS-XADS using the extended SIMMER-III code," Nuclear Engineering and Design 235, pp. 2594-2611 (2005).

[5]   Li, R.; Chen, X.-N.; Rineiski, A.; Moreau, V.; "Studies of fuel dispersion after pin failure: analysis of assumed blockage accidents for the MYRRHA–FASTEF Critical Core," Annals of Nuclear Energy 79, pp. 31-42 (2015).

[6]   Li, R.; Chen, X.-N.; Andriolo, L.; Rineiski, A.; "3D numerical study of LBE-cooled fuel assembly inMYRRHA using SIM-MER-IV code," Annals of Nuclear Energy 104, pp. 42-52 (2017).

[7]   Sarotto, M.; et al., "The MYRRHA-FASTEF cores design for critical and sub-critical operational modes (EU FP7 Central Design Team project)," Nuclear Engineering and Design 265, pp. 184-200 (2013).

[8]   Castelliti, D.; "Comparison of MYRRHA RELAP5 mod 3.3 and RELAP5-3D models on steady state and PLOF transient," Proceedings of IRUG 2013 Meeting, Idaho, USA, 12-13 Sept. 2013.

[9]   Chen, X.-N.; et al., "Recent MYRRHA safety studies with the SIMMER code," NUT-HOS-11, Gyeongju, Korea, October 9-13, 2016, Paper N11A0234 (2016).

JIMEC experiments to investigate jet impingement on a core catcher bottom and LIVE2D 2-Layer experiment

Xiaoyang Gaus-Liu, Thomas Cron, Beatrix Fluhrer, Rene Stängle, Mike Vervoortz, Thomas Wenz

Introduction

In 2019, the research activities in IKET-SAR team were focused on several European projects. Some final work had to be done for the European SAFEST project, coordinated by IKET-SAR team, which ended officially at the end of 2018.

The main activities in 2019 were concentrated on the European ESFR-SMART project. Within this project two large-scale JIMEC experiments have been performed to investigate the thermal ablation kinetics of an internal core catcher material in a SFR reactor. Besides this, the planning work for LIVE-ESFR tests to study the interaction between the corium simulant and the sacrificial simulant of the core catcher started. It has been decided to construct and build a new test vessel with down-scaled geometries similar to SFR core catcher design.

Another activity is the finalization of LIVE2D 2-Layer experimental and analytical analysis, which is a main experimental task in the H2020 IVMR project, which ended in November 2019.

JIMEC experiments to investigate jet impingement on a core catcher bottom and ablation process

Background and Objectives

The actual safety design of a Sodium Fast Reactor (SFR) in the case of a postulated severe accident incorporates to remove the corium from the core by corium transfer tubes and to collect it in the lower head in an in-vessel core catcher. It is assumed that at first a metallic corium melt jet would impinge on the core catcher

surface and could ablate the core catcher material. Experimental data is needed to simulate this ablation behaviour of a long duration melt jet impinging the core catcher material. A particular behaviour can be studied when a molten pool is created ("pool effect") at the impact point that could reduce the heat transfer at the jet – material interface. This phenomenon has been studied very little in the past. Therefore, the IKET-SAR team has adapted the existing MOCKA test facility to perform two JIMEC (Jet Impingement on Metallic Core Catcher) experiments in the frame of the European ESFR-SMART project. JIMEC-1 and JIMEC-2 tests investigate the characteristics of the interaction of a metallic melt jet with the core catcher bottom plate material in a SFR reactor design with prototypical material. The objectives of the experiments are to deliver experimental data on the interaction of melt jet parameter and erosion dynamics. The melt jet parameters were jet temperature, jet velocity and jet diameter. The erosion dynamics in the core catcher bottom is the erosion velocity and the timing of pool effect. The experimental results will be used for developing new correlations which could be used in codes for simulation of the ablation kinetics for SFR core catcher concepts.

Experiments

The two JIMEC experiments have been performed in summer 2019 in the adapted MOCKA test facility, Figure 1. To simulate the core catcher bottom a test substrate was used composed of a cylindrical formed stainless steel block (1.4301) with 416 mm thickness and 425 mm in diameter. A matrix of thermocouples (TCs) was implemented into the test substrate to record the erosion by the melt jet. About 1000 kg of metallic melt was produced by thermite reaction in the separate reaction

crucible above the test substrate. The metallic melt is designed to have the same composition as the metallic test substrate. The outflow opening at the bottom of the crucible was 40 mm in diameter in JIMEC-1 and 30 mm in JIMEC-2. The thermite reaction produced also a lighter oxide melt consisting mainly of Al_2O_3, Cr_2O_3 and CaO. This melt was redirected by a pouring spout to an oxide melt collector.
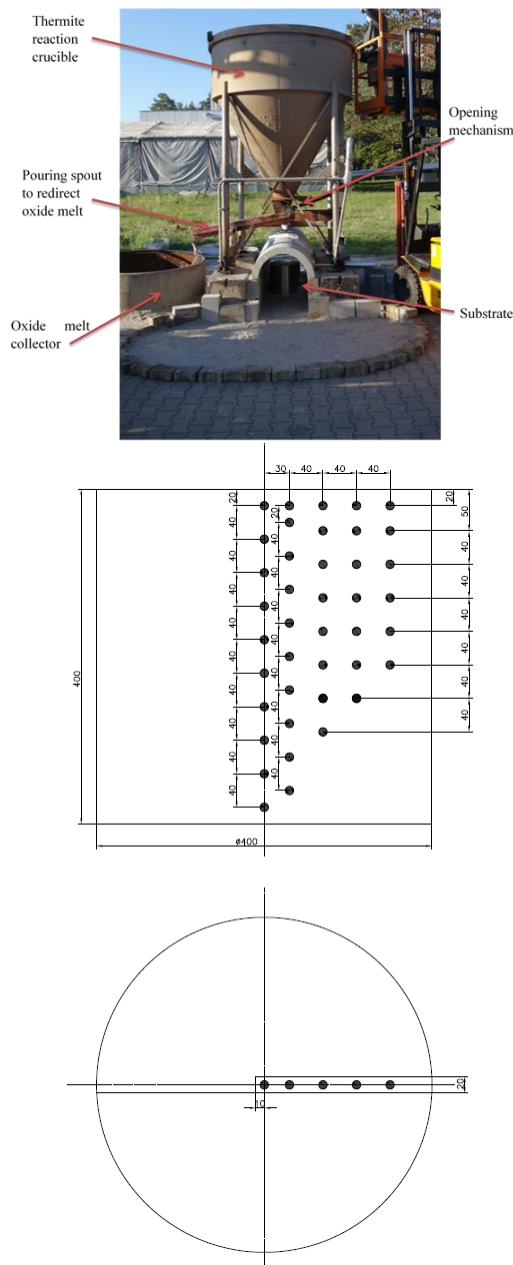
Figure 1: Picture of JIMEC-2 test set-up in top picture and the thermocouple instrumentation in the substrate in the bottom sketch.

For the jet outlet diameter of 40 mm in JIMEC-1, the duration of the metallic melt jet was about 31 s from start of outflow to the end of metallic melt jet. In JIMEC-2 the duration was 55 s due to the smaller jet outlet diameter of 30 mm. In JIMEC-1, the start of pool effect was about 18 s after the first melt reached the substrate indicated by the stop of splashing of the melt, Figure 2. In JIMEC-2, the start of pool effect was detected about 15 s after the first melt reached the substrate surface. Infrared pictures of JIMEC-2 before and after start of pool effect are shown in Figure 3. To protect the environmental apparatus in against the hot splashing melt in JIMEC-2 test, a half-cylinder concrete pipe was positioned upon the substrate with an opening at the jet flow position.
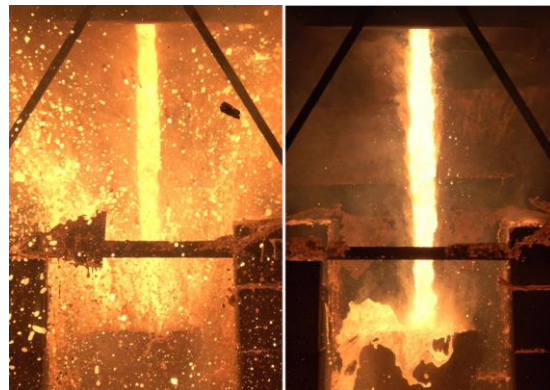
Figure 2: Video pictures of melt jet before and after start of pool effect in JIMEC-1
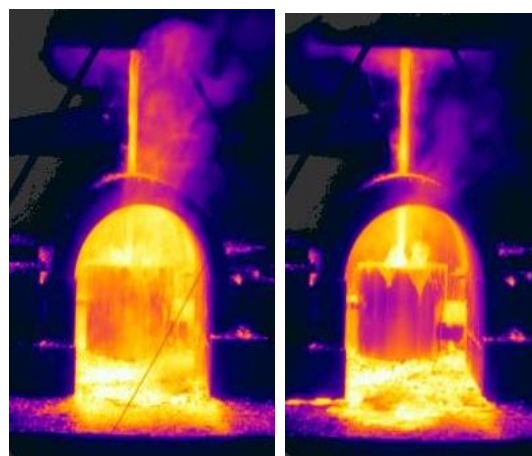
Figure 3: Infrared pictures of JIMEC-2 before and after start of pool effect.

The shape of the jet remained in both tests most time coherent, which means there was no breakup of the jet flow. The jet outflow diameter enlarged during the jet release process since the outlet nozzle made of ZrO_2 was gradually ablated by the metallic and also by the oxide melt. The post-test diameter is 54 – 58 mm for JIMEC-1 and about 46 mm for JIMEC-2. Analysis from high-speed video of JIMEC-1 shows that before the pool effect the melt jet velocity is 4.3 - 4.6 m/s and after the pool effect about 5.0 m/s. The theoretical velocity is about 4.4 m/s at the outlet nozzle. The large velocity at the later phase could be an effect of the enlarged outlet diameter. The metallic melt jet temperature in both tests was in the range of 2000 – 2100 °C measured by a pyrometer. The ablation velocity in the substrate can be obtained based on the thermocouple signals. Figure 4 shows the ablation depth in the substrate versus time for JIMEC-1 and JIMEC-2.
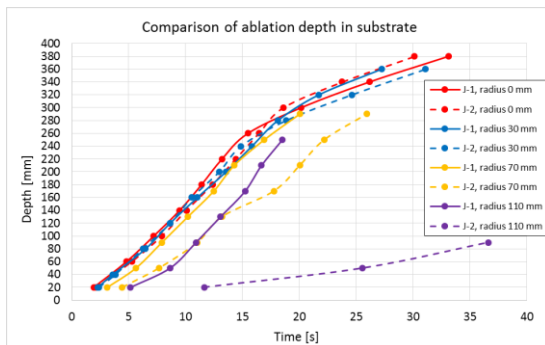
Figure 4: Comparison of ablation depths for JIMEC-1 and JIMEC-2

The ablation rates within 30 mm diameter in the substrate are almost identical for both experiments. The ablation velocity in the center of the substrate is about 17 - 18 mm/s before start of pool effect and decreases to about 7 mm/s after start of pool effect. An influence of the different jet diameter on the ablation behaviour is then detected in the outer regions of the test substrate. For JIMEC-1 with 40 mm jet diameter at the beginning, the radial ablation proceeds faster than for JIMEC-2 with 30 mm jet diameter.

According to the ablation velocity, the contour of ablated pit vs. time can be roughly estimated, as shown in Figure 5. Due to the lacks on measuring position at the outer bottom part, the contour up from 23 seconds can only be partially illustrated. The forms of the contours indicates the initiation of pool effect in17 sec, leading to a slowdown of the axial ablation, however a high radial erosion rate at the lower part, and thus this led to a gradual transformation of a conic pit to a cylindrical pit.
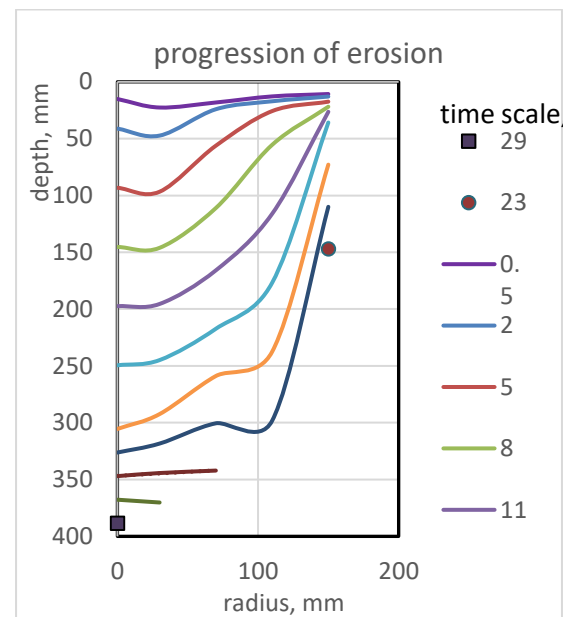
Figure 5: Progression of ablation contour in the JIMEC-1 substrate

The test substrates for JIMEC-1 and JIMEC-2 have been cut after the tests, as shown in Figure 6. The test substrates of JIMEC-1 and JIMEC-2 are molten through by the metallic melt jet. In JIMEC-1 a hole was formed in the lateral wall above a height of ~132 mm from the bottom. Up to the same height, a solidified metal melt has built in the cavity. The mass of both substrates before the tests was about 460 kg. The remaining mass of the test substrate of JIMEC-1 is ~ 240 kg including the solidified metal melt pool. For JIMEC-2, the remaining mass is about 214 kg. Therefore, about 246 kg of the substrate has been molten in IMEC-2 substrate.

Figure 6: Cut of the test substrates of JIMEC-1 and JIMEC-2

Analyses of the LIVE-2D two-layer test series on the heat flux focusing effect and the thermal-hydraulic character in the upper melt layer

Two series of LIVE2D two-layer tests with 3 upper layer thicknesses and different surface boundary conditions were carried out in 2017. The experiment reveals major thermos-hydraulic characteristics of the upper light melt layer during the transient and steady states as well as the strong dependence of the heat flux focusing effect on the upper boundary cooling condition. The final analysis of the two test series comprises the study the heat flux focusing effect upon different boundary conditions and

the characterization of the thermal-hydraulic feature of the upper layer.

Strong heat focusing effect was observed at the wall in the upper melt layer in LIVE2D-SO1 test, which had a hot upper atmosphere. And no heat flux focusing effect appeared when the melt upper surface was rigidly cooled, which was the upper boundary condition of the second test series (LIVE2D-SOTC). Figure 7.
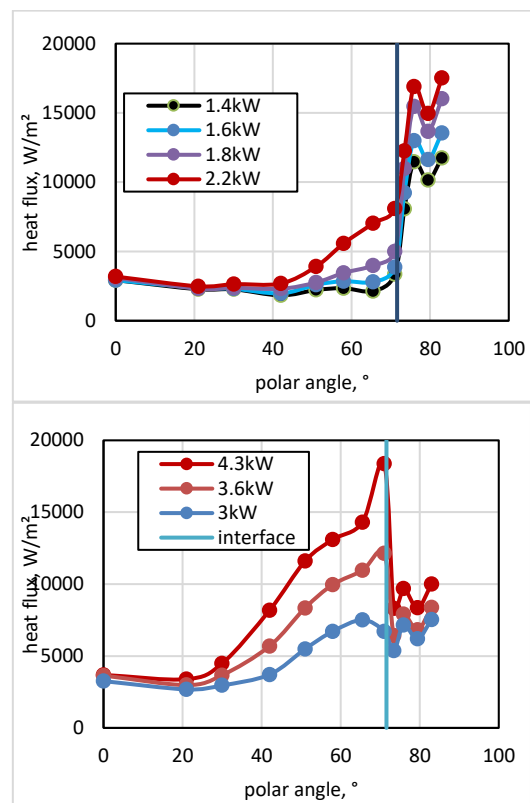
Figure 7: Heat flux at the vessel wall with 110 mm upper layer. Top: during SO1 test; bottom: during SOTC test.

The experiment results demonstrate further that without effective cooling at the upper boundary, the melt circulates globally from the hot central region radially toward the cooled wall boundary, resulting a large diversion of bottom boundary temperature, as shown in Figure 8. Whereas dimensionless temperature $\theta' = (T - T_{min})/(T_{max} - T_{min})$, z: distance to the bottom and L: the layer thickness. Upon this turbulent flow character, the generally applied Globe&Dropkin correlation, describing convective heat transfer upon a uniform hot

bottom plate to the cold bulk melt in vertical direction, is not suitable for the upper layer heat transfer with limited upper heat transfer rate.
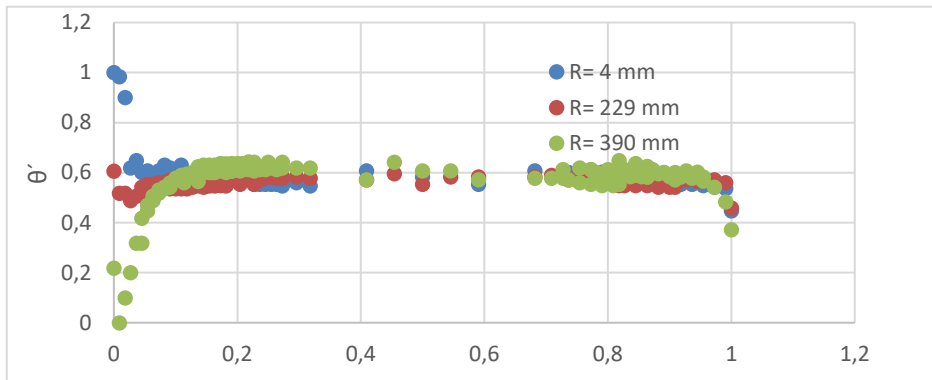
Figure 8: Dimensionless temperature vs. vertical position of a 110 mm upper layer inSO1 test

In addition, the specific boundary combination of the upper layer without strong top cooling doesn´t exactly correspond the sidewall heat transfer situation of the widely applied Churchill&Chu correlation, which describes the heat transfer of a heated vertical wall to the cold environment. In Figure 9 the LIVE2D experimental results are plotted in comparison with the two Churchill&Chu correlations, and the experimental results show a considerably lower convective heat transfer capability than the Churchill&Chu correlations.
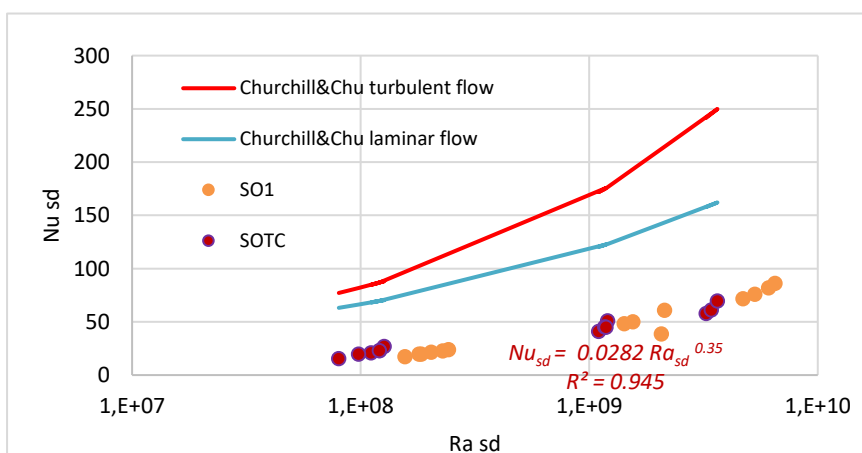
Figure 9: Comparison of Nu at the heat transfer at the upper layer sidewall

Group: Multi Phase Flow

Detailed investigations on flow boiling of water up to the criticalheat flux

Stephan Gabriel, Giancarlo Albrecht

Introduction

Multiphase flows occur in various fields of process engineering and energy technologies. Highly complex phenomena such as flow boiling up to the critical heat flux (CHF) or counter current flow limitation CCFL arise from a whole series of phenomena such as convection, bubble formation, evaporation, condensation, drop/bubble fragmentation or coalescence and many more. In order to to understand the behaviour of two-phase flows in real technical systems in detail, it is necessary to consider both the individual phenomena and the more complex phenomena in the experiment and to advance the development of simulation programs with detailed data sets.

The Group Multiphase Flows (MPF) works therefore on investigations at different scales from experiments on single effects [4] to experiments on complex phenomena like CHF. Since the required measurement technology is in many cases not commercially available, the development of suitable sensors, for example for the acquisition of detailed phase distributions, is also part of the task.

Results

In 2019, the focus of work was on the construction of the high-pressure test facility COSMOS-H on the one hand, and on the other the completion of measurements on a rod bundle test section of the low-pressure test facility COSMOS-L. As a further important work package, extensive work was carried out on modernizing and upgrading the laboratory infrastructure in view of the upcoming commissioning of COSMOS-H. This includes the procurement or re-commissioning of laboratory equipment such as tensiometers, microscopy and measuring instruments for determining water quality for the tests and as a precondition for the tests the upgrading of the crane technology for the new test track. In addition, the dismantling of the meanwhile 20-year-old test facility DISCO was carried out to create urgently needed space for COSMOS-H.

COSMOS-L

At the COSMOS-L test facility in 2019, further measurements were made to complete a dataset on a rod bundle and then a new test track with a flat vertical heater was developed. A measurement data set for the rod bundle consisting of 5 Zircalloy tubes, which was created within the framework of the joint project NUBEKS [2,3], was supplemented by further measurement points and measured variables. The measurements characterize the behaviour starting from flow boiling up to the boiling crisis (CHF). As can be seen in Figure 1, the test section has a rod bundle consisting of five separately heatable cladding tubes. During the tests, either all tubes were heated in order to obtain the most realistic phase distribution around the central tube, or only the central tube was heated in order to concentrate the instrumentation there. The results presented below were obtained by experiments with only one heated tube.

The test results presented in the following refer to a static pressure of 1200 mbar, a mass flow density of 50 kg/(m²s) and a test track inlet temperature of 80°C. This corresponds to an inlet subcooling of approx. 25°C. As shown in Figure 2, bubble boiling already occurs at a

heating power of 4 kW, which becomes more and more intensive with increasing heat flux. The critical heat flux is reached at this boundary conditions at a heating power of approximately 10.8 kW.
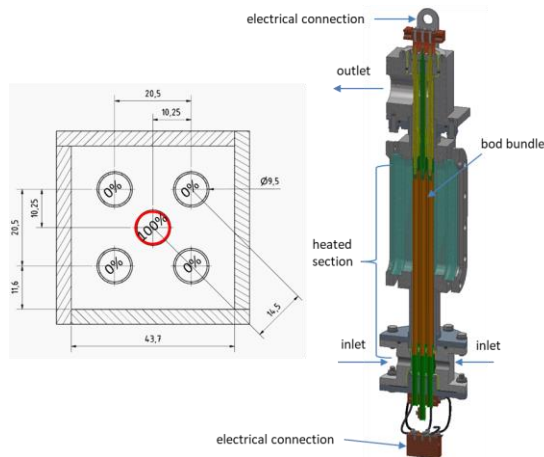
Figure 1: Experimental setup of the bundle measurements

Analogous to the previous experiments 2018, the experiments were repeated several times, here a total of 29 times, and a frequency distribution of the CHF value was generated (see Figure 3). The measured values related to the heated surface thus result in a critical power of $CHF_{mean} = 1.1257$ MW/m² with a standard deviation of $\sigma = 0.013$ MW/m².
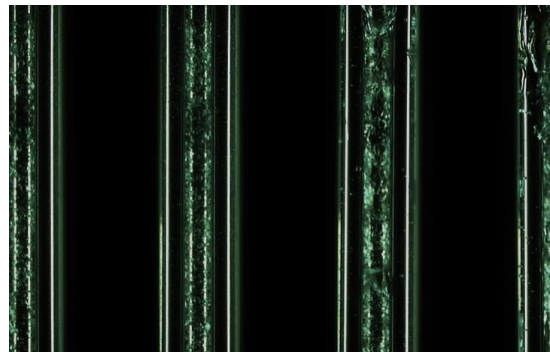
Figure 2: Flow pattern as a function of heat output

In addition, the locations where the CHF occurred on the cladding tube could be calculated by correlation of the three thermocouples closest to the hotspot [5]. For this purpose, the heated pipe in the test section is divided into triangles between each three thermocouples. The measured temperature values show different signals depending on how close they are to the location of the CHF. Characteristic here are on the one hand the waiting time, i.e. the running time of the signal, and on the other hand also the temperature gradient.

After the basic function of the principle was demonstrated on a sheet metal of 40 × 40 cm² with a propane gas burner as heat source, the CHF events of the COSMOS-L measurements were evaluated concerning the frequency distribution shown above. It is evident that the
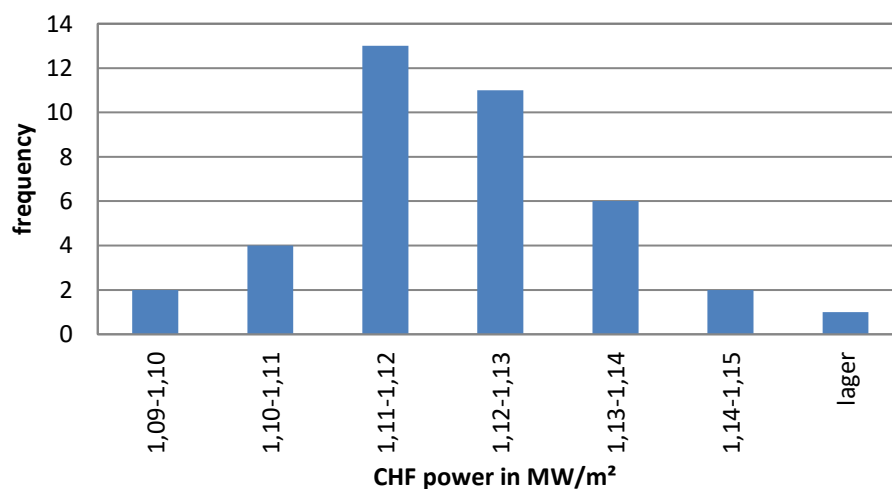
Figure 3: Frequency distribution of the critical heat flux after 29 tests

method has room for improvement in terms of precision. However, it can certainly be used to determine during a test whether the CHF events always occur at the same location, which would be an indication of damage to the heating tube.

As expected, most CHF events could be identified at the upper end of the 326 mm long heated tube. It was found that although there are accumulations of CHF events but they rarely occur directly one after the other [5].

Following the rod bundle experiments, the design and construction of a new test arrangement for experiments within the project KEK-SIMA was started, in which, together with the Institute of Applied Thermofluidics (IATF), the effects of transient mass flows on the critical heat flow density will be investigated. For this purpose, a test section with a plate-shaped heating element was constructed in 2019 (see Figure 5). In addition to a powerful heater, the test section also has three window elements for observing the flow and numerous sensors for recording all relevant boundary conditions. A precondition for the upcoming tests is an increase in performance and an extension of COSMOS-L by numerous pressure, temperature and mass flow sensors. In addition, a by-pass to the test track will be installed in the coming year in order to ensure stable system operation and thus reproducible test boundary

conditions even with fluctuating mass flows in the test track.
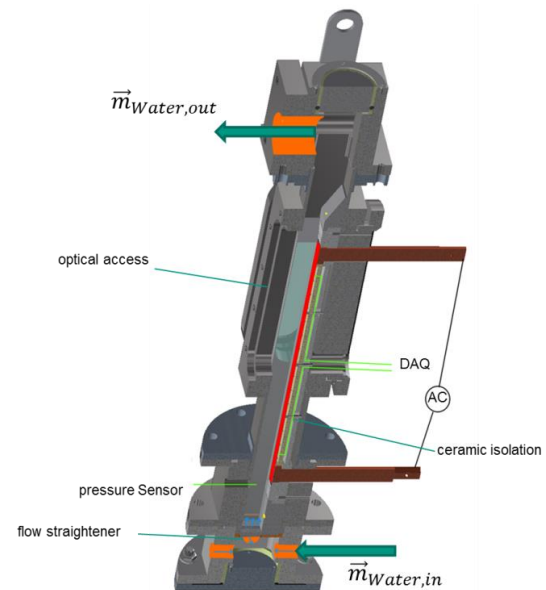
Figure 5: New test section concept with flat heater to investigate the critical heat flow density with flucuating mass flows

COSMOS-H

The thermohydraulic test facility COSMOS-H is a high pressure high temperature water loop being built for the investigation of boiling phenomena and other flow phenomena that can occur in thermal power plants. In contrast to COSMOS-L, the loop will achieve non-scaled test conditions comparable to a boiling water
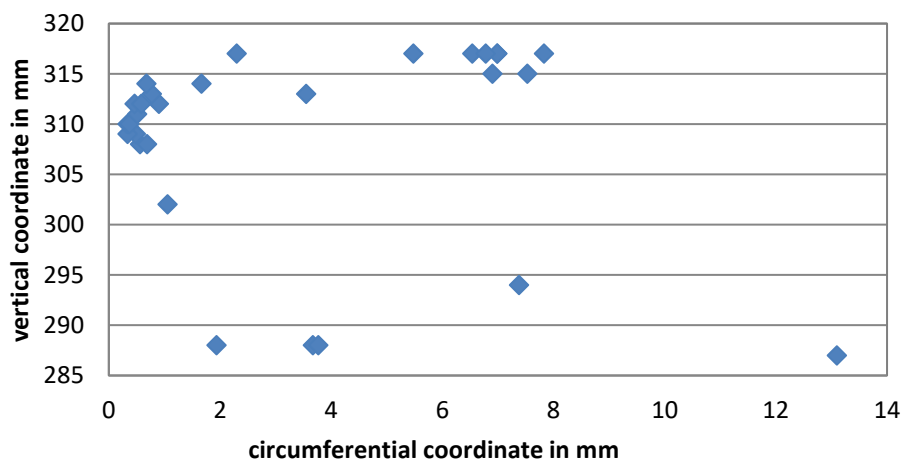
Figure 4: Local distribution of CHF events on the middle pipe [5].

31

reactor or pressurized water reactor (up to 170 bar, 360°C) during test operation. The work on the construction of the COSMOS-H test facility was continued as planned in 2019. Numerous subsystems were completed and some have already been commissioned (see Figure 6). These include, for example:

- The power supply for the control system and all electrical consumers was completed

- The two cooling loops of the facility were completed (cooling capacity 1.8 MW)

- The compressed air supply to drive the automatic valves is completed, including the emergency supply system.

- The hardware of the digital control system (SPS) as well as the technology of the control station is completed.

- The pumps and valves of the plant are now functional.

- The crane technology for the assembly and installation of the test track, consisting of assembly crane, transport trolley, crane traverse and hall crane, has been completed.

Further work is now concentrating on completing the high-pressure loop and the necessary safety systems.

Acknowledgement

Figure 6: Images of various subsystems of the plant under construction

References

[1]   Tromm, Th. W.; Kaiser, F.; Gabriel, S.; Heiler, W.; Albrecht, G.; "Investigations on Flow Boiling under forced Convection on Zircaloy Tubes up to Critical Heat Flux" (NENE2019) 9-12.9.19 Portoroz Slovenia

[2]   Kaiser, F.; Dietrich, B.; Gabriel, S.; Wetzel, T.; „Final Report Project NUBEKS Experimentelle Ermittlung von kritischen Wärmestromdichten bei reaktortypischen Bedingungen als Validierungsdaten" 27.02.2019 (BMWi 1501473B)

[3]   Lifante, C.; Ben Hadj Ali, A.; Eickenbusch, H.; Bruder, M.; Kaiser, F.; Gabriel, S.; "PREDICTION OF CONVECTIVE BOILING UP TO CRITICAL HEAT FLUX (CHF) CONDITIONS FOR TEST FACILITIES WITH VERTICAL HEATERS", 27th International Conference on Nuclear Engineering, May 19-24, 2019, Ibaraki, Japan

[4]   Albrecht, G.; Heiler, W.; Büttner, F.; Gabriel, S.; "Experimental investigation of air entrainment by a vertical jet plunging into a liquid

pool", 10th International Conference on Multi-phase Flow, ICMF 2019, Rio de Janeiro, Brazil, May 19 – 24, 2019

[5]   Bernez, V.; "Measurement of bubbles dynamics in a five-strand bundle", MASTER THESIS, KIT, 2019

Group: Karlsruhe Liquid metal LAboratory (KALLA)

Concentrating Solar Power with Liquid Metals as Heat Transfer Fluids

Frank Fellmoser, Jonathan Flesch, Markus Daubner, Franziska Müller-Trefzer, Julio Pacio, Klarissa Niedermeier, Leonid Stoppel, Harald Piecha, Neele Uhlenbruck, Kurt Wittemann, Thomas Wetzel

Introduction

Liquid metals are investigated as heat transfer fluids in concentrating solar power systems due their excellent heat transfer properties [1,2]. In the SOMMER test facility at KALLA, lead bismuth eutectic (LBE) is used as heat transfer fluid in a so-called thermal receiver in the focal point of the solar furnace [3]. During 2019, the SOMMER test facility has been put up into operation and tests were performed under direct concentrated sunlight conditions. The thermal receiver – efficiently cooled by LBE – withstood maximum heat flux densities of 4 MW/m² without any failure.

Thermal receiver tests in the SOMMER facility

At the location of the SOMMER facility, peak DNI values of up to 950 W/m² have been measured. The sunlight is reflected by the heliostat mirror (32 m²) and onto the parabolic mirror (16 m²) inside the SOMMER laboratory, where the solar power is concentrated. The solar furnace arrangement without the liquid metal loop is shown in Fig. 1. The installed shutter blinds in front of the parabolic mirror can be adjusted for tests under part-load conditions. For safety reasons, a curtain has been installed that drops into the light passage driven by gravity in case of a power outage or other irregular conditions. Additionally, the heliostat mirror is moved automatically into stow position if there is a power outage.

Figure 1: Solar furnace arrangement consisting of a heliostat mirror (front, outside) and a parabolic mirror (back, inside the laboratory) (Foto: J. Flesch).

The liquid metal LBE can be pre-heated in an electric heater before entering the thermal receiver to allow for a wide measuring matrix. After leaving the thermal receiver, the heated liquid metal is again cooled down before entering the pump tank. The pump is a submerged mechanical gear pump delivering 0.1 L/s at 1000 turns/min and is designed to operate up to a temperature of 380 °C. It is located at the highest point of the SOMMER liquid metal loop. During down time or in case of an emergency, the fluid flows down into the sump tank due to gravity. The sump tank has capacity for 130 L of lead-bismuth (Fig. 2).
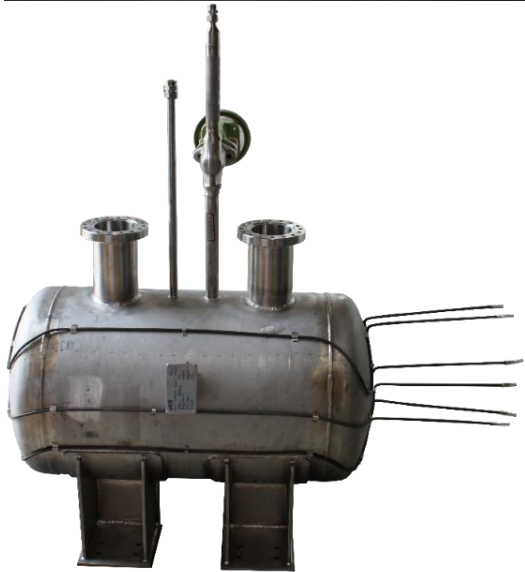
Figure 2: The sump tank of the SOMMER test facility; top: insulated (Foto: Amadeus Bramsiepe/KIT); bottom: before insulation with electric trace heating (Foto: F. Fellmoser).

The thermal receiver, which is cooled by the LBE flow, is installed in the focal point of the parabolic mirror. It is designed as a spiral tube of 10 mm outer diameter with a wall thickness of 0.5 mm. The area being heated by the sun

is 100 mm x 100 mm. The inlet and outlet temperatures of the receiver are measured with thermocouples to determine the thermal power that is absorbed by the liquid metal flow. In total, the thermal receiver has a thermal power input of max. 13 kW. Figure 3 shows the thermal receiver connected to the liquid metal loop. The tubes are coated with Pyromark 2500 to improve the absorption of the sunlight. A large copper plate is installed around the receiver to prevent damages on other components in case of a tracking error of the heliostat. The copper plate will then absorb the heat and the light source can be cut off in this time.

Figure 3: The thermal receiver of the SOMMER test facility with copper shield (Foto: Amadeus Bramsiepe/KIT)

In order to determine the incoming solar power on the receiver a heat flux measurement device was developed [4–6]. It uses a heat flux micro sensor that moves across the focal area on a circular path superimposed with a linear motion. In the SOMMER test facility, the liquid metal loop's position – and thus the thermal receiver's position – is fixed. The parabolic mirror, however, can move along a distance of 0.5 m driven by a linear motor and thus, the focal area can be shifted for the heat flux measurement. Heat flux density (q') values of up to 4 MW/m² were measured and successfully cooled by the lead-bismuth flow, as shown in Fig. 4.
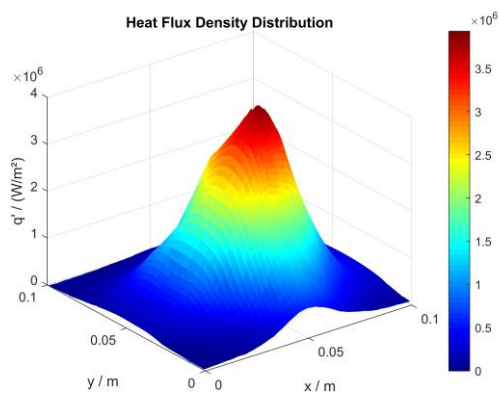
Figure 4: Heat flux distribution measured 28.06.2019 with open shutter blinds

In addition to the experimental investigation in the SOMMER facility, thermal energy storage options for liquid metal were compared [7] and a dual-media thermocline storage system was theoretically investigated in detail [8]. High-temperature thermal energy storage with liquid metals was also investigated regarding the application in energy-intensive industries with waste heat at high temperatures [9, 10]. Experiments for such high temperature thermal storage and liquid metal based process technology are ongoing in KALLA [11].

References

[1]   Pacio, J., Wetzel, T. (2013), Assessment of liquid metal technology status and research paths for their use as efficient heat transfer fluids in solar central receiver systems. Solar Energy, 93,11–22.

[2]   Flesch, J., Niedermeier, K., Fritsch, A., Musaeva, D., Marocco, L., Uhlig, R., Baake, E., Buck, R., Wetzel, T. (2017). Liquid metals for solar power systems. Conf. Series: Materials Science and Engineering, 228, 012012.

[3]   Flesch, J., Fritsch, A., Cammi, G., Marocco, L., Fellmoser, F., Pacio, J., Wetzel, Th. (2015) Construction of a test facility for demonstration of a liquid lead bismuth-cooled 10kW thermal receiver in a solar furnace arrangement – SOMMER. Energy Procedia, 69, 1259–1268.

[4]   De Geus, J.; System zur Flussdichtemessung in einem Sonnenofen, M.Sc. thesis. Karlsruhe Institute of Technology (KIT), 2015

[5]   Albrecht, C.; Messung der Leistung konzentrierter Solarstrahlung in einem Sonnenofen, M.Sc. thesis. Karlsruhe Institute of Technology (KIT), 2016

[6]   Jipa, A.; Messung der Leistung konzentrierter Solarstrahlung in einem Sonnenofen, M.Sc. thesis. Karlsruhe Institute of Technology (KIT), 2017

[7]   Niedermeier, K., Flesch, J., Marocco, L., Wetzel, Th. (2016) Assessment of thermal energy storage options in a sodium-based CSP plant. Applied Thermal Engineering, 107, 386–397.

[8]   Niedermeier, K. Numerical investigation of a thermal storage system using sodium as heat transfer fluid, PhD thesis. Karlsruhe Institute of Technology (KIT), 2019

[9]   Pacio, J.; Niedermeier, K.; Wetzel, T., „High-temperature thermal energy storage concepts based on liquid metal technology", Eurotherm Seminar 112 (2019): Advances in Thermal Energy Storage (2019), Lleida, Spanien, 15.–17. Mai 2019

[10]   ] Laube, T., Marocco, L., Niedermeier, K., Pacio, J., Wetzel, T. (2019) Thermodynamic Analysis of High-Temperature Energy Storage Concepts Based on Liquid Metal Technology. Energy technology, 1900908.

[11]   Heidelberger, M. Alleskönner Flüssigmetall: Metallschmelzen ermöglichen klimafreundliche Energietechnologien. lookKIT, 0119, 38-41 (2019).

Group: Accident Management Systems

Multi Criteria Decision Analysis: Uncertainties and Combining Decision Making Methods

T. Müller, S. Möhrle, S. Bai, W. Raskob

Introduction

Support of decision making is a form of data transformation by analysing complex circumstances and processing large amounts of data with the goal to present helpful information to decision makers in a simplified and better understandable way. Within the terms of this broad definition, many methods, algorithms, and visualisation means qualify as decision support. However, there is no best method in a general sense, as all these methods have their pros and cons in respect to the specific situation they are applied to. In addition, different methods can be combined to improve the overall performance of decision support.

Originally, decision support methods used deterministic data and thus their output was deterministic as well. Consequently, such information leads to binary thinking and hard decision making, e.g. if a countermeasure strategy is to be chosen, deterministic decision support forces the view that one specific strategy is unconditionally the best and superior to all other available strategies. However, depending on the method used for decision support, minor changes in the input data can have a huge impact and can cause a different outcome. As input data is in general not deterministic but affected by uncertainties, this may result in recommendations of suboptimal strategies in emergency management. Therefore, it is necessary to consider uncertainties in decision making methods to improve the overall decision support.

Uncertainty influencing decision making

Many forms of uncertainty can be identified that have an influence on the assessment of an emergency and its development over time. The following list is certainly incomplete but gives an impression of uncertainty types: stochastic uncertainties in form of physical randomness, epistemological uncertainties by lack of scientific knowledge, endpoint uncertainties when the desired goal endpoint is ill-defined, judgemental uncertainties by defining personal preferences as facts, and computational uncertainties by e.g. inaccuracy through numerical instability or modelling errors as models are always a simplification of the real world and therefore limited in one way or the other [1]. Sometimes the errors introduced by these uncertainties may be small, but as they add up they could lead to choosing inferior strategies in the end.

The CONFIDENCE project

The European project CONFIDENCE (2017-2019) aimed to analyse uncertainties and to improve the support for emergency management, especially focussing on nuclear accidents [2]. CONFIDENCE investigated the influence of uncertainties on the different phases of the full chain of managing a nuclear accident beginning with the assessment of data (weather, source term), continuing with simulation of the situation development (dispersion, food chain), over analysis of possible countermeasure strategies (decision support) up to the communication of situation development and strategies to the public (social science). Within this project the Accident Management

Systems (AMS) group of ITES had a leading role as coordinator of the project and as leader of work package 6, which investigated the influence of and coping with uncertainties in decision making. The work package especially focussed on enhancing the existing Multi Criteria Decision Support (MCDA) tool to handle uncertainties as well as Agent Based Modelling (ABM) to analyse and better understand the effects of uncertainties on the decision making process. A special issue of the Radioprotection Journal is dedicated to the CONFIDENCE project and will be available in the second half of 2020.

Multi Criteria Decision Analysis as decision support

Multi Criteria Decision Analysis (MCDA) covers various decision support methods, that in general provide a ranking on a set of alternatives by integrating (contradictory) decision criteria of different scale according to given (personal) preferences [3]. The ranking helps decision makers to choose the best suited alternative, which is frequently, but not necessarily, the highest ranked alternative. Considering emergency management, MCDA syste-matically combines the pros and cons of feasible actions to be aggregated into a single numeric value, which makes them easily comparable between each other. The higher the value, the better the according action is rated. In managing nuclear emergencies, the actions are in general a set of countermeasure strategies like "Evacuate people and clean surfaces before they return".

Each action is assigned a ranking value $A_1,\cdots,A_n$. The criteria are either quantitative values like "Estimated dose" or qualitative values like "Public acceptance". The criteria values $C_1,\cdots,C_m$ are either simply measured or determined. For numerical evaluation, qualitative value ranges like {"low","high"} have to be mapped to quantitative value ranges like {1,2}. Since the criteria are typically of different units and

scales, the criteria values have to be normalised onto a unified scale before combining them. For this purpose, normalisation functions $N_1,\cdots,N_m$, such as e.g. min-max normalisation, have to be defined for every single criterion. The personal preferences of each criterion are represented through weights. The relative importance of a criterion is reflected in a specific normalised weight $w_1,\cdots,w_m$. The normalised values of criteria are aggregated in a ranking value by using an aggregation method according to their weight. One of the most popular aggregation methods is the computation of the weighted sum, which for each alternative requires the following computation:

$$A_i = \sum_{k=1}^{m} w_k \cdot N_k\big(C_{k,i}\big) \quad \forall\, i \in n$$

The actions are sorted according to their ranking values, indicating their order of recommendation. Ranking and results can be presented in multiple ways like e.g. charts, graphs, textual report, and others depending on the specific requirements of the decision makers (e.g. Figure 2, Figure 3).

Though from the mathematical point of view the method is plain and straightforward, there are several catches to consider when applying it. Firstly, the actions to rank are not generated but determined externally, either by another tool or by the decision makers themselves. Secondly, the determination of feasible criteria is also up to the decision makers. As emergency management is in general subject to a group of decision makers respectively advisories they have to agree on such a set of criteria as a group, finding a common consensus. The same holds for determination of qualitative criteria values, which may be based on personal assessment. Finally, the weights are dependent on personal preference and therefore need to be agreed upon within the group. This leads to a time consuming setup and intense discussions among the group members, making the MCDA method preferable in situations where time is available, e.g. in preparation, training or long term recovery decision making. On the

other hand, as a benefit, the intense discussions result in transparency and documentation how the ranking and therefore the decision was justified.

Considering uncertainties in MCDA

The MCDA as described above will process deterministic parameters, yet most, if not all, scenarios of decision making are affected by uncertainties, which requires processing of probabilistic parameters. The following section describes how this limitation can be overcome.

Two obvious parts of MCDA can be affected by uncertainty: the criteria values and the criteria weight values. Such uncertain values can be described probabilistically: either as functions or histograms. Histograms can be easily achieved by binning and counting according values, e.g. for a histogram of a criterion weight let all decision makers provide an integer weight value between 1 and 10 according to their preference and accumulate the values. On the other hand, determining distribution functions for criteria values like the "Estimated dose" is rather difficult. Yet the important part is not to achieve higher accuracy, but to introduce the potential variety of values into the ranking, thus sensitising decision makers to rather look for the most robust solution in all circumstances instead of the best solution for one specific case.

MCDA cannot process distribution functions or histograms as input values. For this reason, ensemble evaluation is applied to overcome this limitation. Simply put, from the probabilistic MCDA a number of deterministic MCDA are generated and evaluated one by one. The deterministic results are combined back into one probabilistic result. Because of its simplicity several thousand MCDA can be generated and evaluated within a second, allowing for large sample sets.

The MCDA tool has been enhanced in that way to define probabilistic input, to perform ensem-

ble evaluation, and to present probabilistic results [4]. Figure 1, Figure 2, and Figure 3 give an impression on the implemented enhancements.
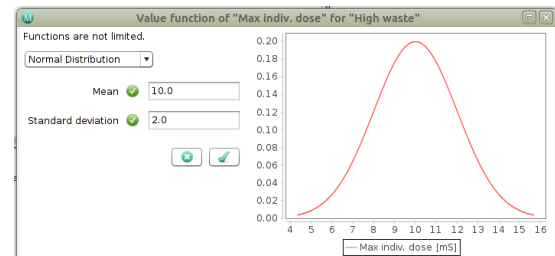

Figure 1: Definition of a criterion value as normally distributed.
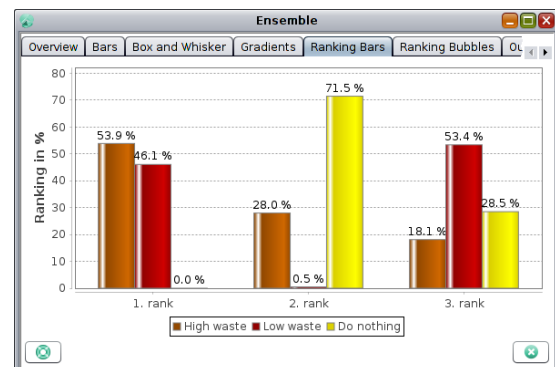

Figure 2: Overview on probabilistic ranking of 3 alternatives. In this example "High waste" was ranked first place in 53.9 percent of all evaluations of the ensemble set.
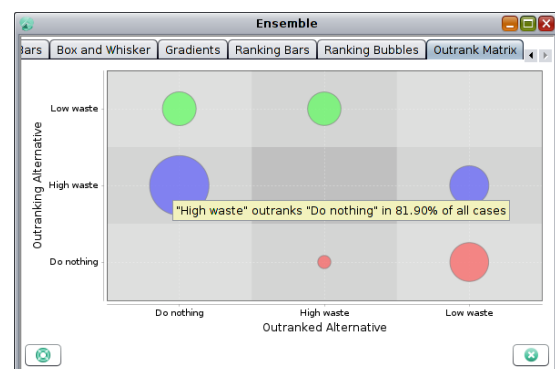

Figure 3: An outranking matrix indicating how often an alternative was ranked better than another one.

Agent Based Modelling of the decision making process

The decision making process of stakeholders is much more complicated than one would expect at first glance, as not only plain numbers are considered but also personal preferences, experience, prognosis of situation development and behaviour of affected people, etc. The decision makers involved in emergency management may have different backgrounds and may belong to different organisations, which is reflected in their individual personality and their assessment of the emergency situation, thus introducing uncertainties in the decision making process.

To consolidate their different personal decisions into a single one they have to work together, share thoughts, negotiate, and finally find a compromise that is acceptable for everyone. The best way to understand this process would be to interview and observe the decision makers while they are confronted with a large number of different scenarios. However, this would take a considerable amount of time, especially of the stakeholder's time, and therefore is not feasible in praxis. A practicable approach to address this is to model the behaviour of decision makers and the process of decision making. Such a model allows for simulation and analysis of a large number of different scenarios, leading to a better understanding of the underlying uncertainties.

Agent Based Modelling (ABM) is a programming paradigm that allows for simulation of (intelligent) individuals, so called agents, and the complex interactions between them. More specific, a software agent is defined as a computer system (program) that is situated in some environment, and that is capable of autonomous actions in this environment in order to achieve its delegated objectives [5]. ABM is therefore inherently predestined to model and analyse decision makers as individuals and their interaction and hence was chosen for this task in CONFIDENCE.

Figure 4 displays the concept of a software agent in more detail. The agent to the right interacts with the environment and also other agents on the left. It perceives observations on the environment by its sensors. The same way it is capable to perform actions on the environment with its actuators. Agents are capable of evaluating their environment and of decision making by means of simple rules up to artificial intelligence.
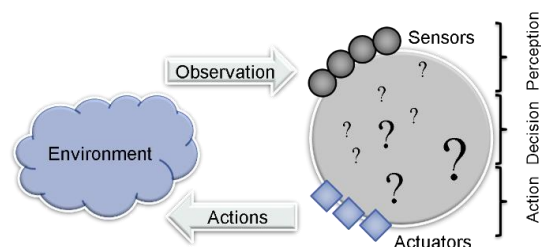
Figure 4: Structure of an autonomous (software) agent interacting with its environment.

It is obviously the decision making, that defines an agent in the end. In the context of modelling nuclear emergency management, an agent has to select the best countermeasure strategy from a set of strategies on the basis of parameters. In CONFIDENCE we interviewed emergency managers from different countries by questionnaires, on how they make their decision, what rules they follow, etc. From this information a set of agent types was modelled and implemented as well as methods for negotiation between agents to find to a common consensus. An intelligent strategy evaluation system based on the agent-based negotiation simulation has been introduced in order to simulate the decision making process of stakeholders on computationally tractable assumptions. In the framework of the system, agents can score the recommended strategies before negotiation and negotiate them by using different negotiation skills [6,7]. Moreover, one indicator was introduced to describe how much the agents can compromise in each negotiation [7]. This parameter may also reflect the degree of selfishness behaviour of agents. Figure 5 displays a chart of the demonstrator, where

agents negotiate on the ranking value of a strategy.

Figure 5: A group of 12 agents agreeing on a ranking value for a one strategy within 14 iterations.

Combining methods

Decision making methods have their own specific upsides and downsides, e.g. an upside of MCDA is that it is simple and increases transparency, while as downside the alternatives to rank have to be known beforehand. Carefully combining decision making methods can greatly improve the overall usability as well as the quality of results. In the following two combinations of methods are presented that can benefit from each other.

Evolutionary Algorithms, ABM, and MCDA

Evolutionary Algorithms (EA) are constructive optimisation methods, i.e. they search for an optimal, or in praxis close to optimal, solution within given parameter ranges, especially if no knowledge is available how to construct the optimal solution [8]. Regarding emergency management this means existing countermeasure strategies are modified in a way that they fit to the current emergency situation.

The basic idea of EA is to encode a solution respectively countermeasure strategy as a ge-

nome of an individual and to have a large population of individuals evolve in the desired way. For this, each individual is evaluated in respect to its survivability, called fitness. The least fit individuals are removed and the population is filled up with new child individuals derived from the ones that survived by combining and modifying the genes of some parents in a process called crossover and mutation. The process is repeated until some criterion to stop is reached. While the method is straightforward the challenge is obviously the encoding of a strategy as genome and the evaluation of the fitness of the individuals.

In a complex decision support system based on ABM, e.g. for simulation of power supply management of a city, the EA can be introduced as a "super-agent" that constructs strategies and interacts with the agents for fitness evaluation. In addition to the negotiations with other agents, the agents as autonomous individuals have their personal preferences on the suggested strategies. Therefore, it seems evident to model such individual behaviour by MCDA. That way the advantages of the three methods can be combined into a more efficient decision support system. Currently we follow this approach in the framework of the HGF portfolio security for evaluating power distribution management in future cities.

Case Based Reasoning and MCDA

As mentioned above, one integral and challenging part of MCDA is to define alternative actions to be evaluated. An EA is one opportunity to construct strategies to be further analysed according to different criteria. Another approach is prepare a database with different scenarios and strategies beforehand to be used in a decision situation. This approach was particularly pursued in CONFIDENCE where Case Based Reasoning [9], a problem-solving paradigm, was applied to select strategies to be negotiated in the framework of ABM of the decision making process [6].

Hence, for defining decision alternatives, CBR can be applied to limit the set of possible options. Originating from cognitive science, CBR utilizes specific knowledge of previously experienced problem situations to solve a new problem. The main assumption is that similar problems have similar solutions. Hence, a possible set of decision alternatives is based on experiences of similar and solved problems, which in our context, correspond to simulation results. This approach and especially the determination of suitable criteria have been further elaborated in the framework of nuclear emergencies, where MCDA is applied to assess several possible disaster management strategies [10]. The objectives have been to rank different strategies in a transparent manner, to provide a broad discussion basis, and to preserve flexibility to account for the variability of disasters and users' preferences. In particular, the contributions of the different criteria to the overall assessment are revealed.

The basic idea for assessing strategies is to integrate commonly discussed approaches that refer to performance measures and investigating robustness. Furthermore, CBR related values that reflect the trustworthiness of the solutions proposed are respected as well. The multi-criteria assessment considers current conditions, possible future developments, utilizes simulations of strategies to account for current constraints and uncertainties with regard to time, for example, and facilitates users' trust and understanding in the mechanism of the decision support method by integrating confidence values. These different perspectives are summarized (Figure 6) where the overall objective is to protect public and environment being decomposed into the criteria 'effectiveness', 'resources', 'robustness' and 'confidence'. Specifically oriented towards nuclear emergencies, the effectiveness is measured according to (i) the factor of dose reduction (ii) the amount of waste, and (iii) public acceptance, taking into account non-radiological quantities as well. The criterion 'resources' states through which means the objectives are achieved and hence which resources and to what extent they are utilised. These results are gained by simulating the strategies considered and analysing them according to duration and uncertainties in respect of potential delays during the implementation possibly causing a reduced resource utilization. Here, a strategy mo-del that is based on Petri nets is used allowing to capture combinations of measures, their order of implementation, the objects
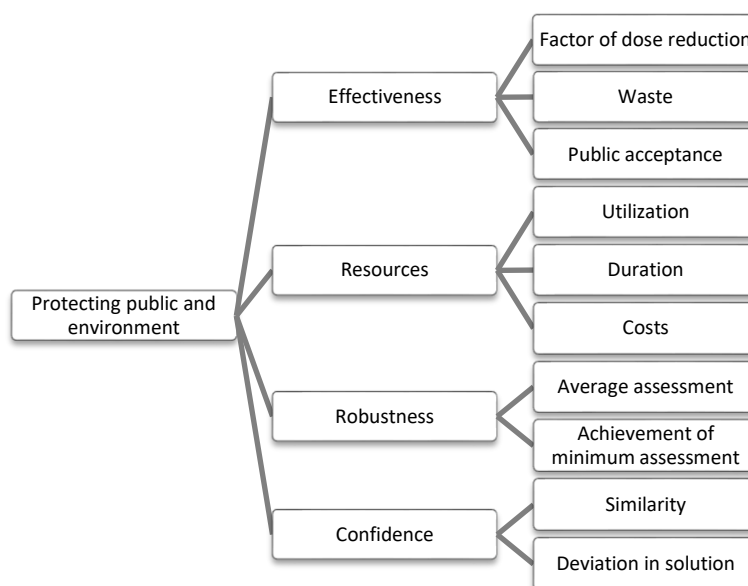

Figure 6: Hierarchy of criteria for strategy assessment [10, Figure 6.6]

measures are targeted at, and resources [11]. Simulation results of JRodos [12] particularly provide costs of strategies. The criterion 'robustness' considers uncertainties with regard to the extent of a disaster, changing environmental conditions, or insufficient information. For judging how robust a strategy is, a scenario-based approach [13] is pursued, investigating different scenarios and determining corresponding effectiveness values under these varying conditions. The criterion 'confidence' is related to CBR and can be made measurable by similarity values and deviations in the different solutions.

The multi-criteria assessment helps to structure the decision problem, reduces its complexity, and promotes discussions of the stakeholders involved by, for instance, visual support (Figure 7). In particular, different views on strategy assessment are integrated addressing various preferences that need to be respected in the final decision. Furthermore, different strategies can be discussed and analysed according to their sensitivity in respect of weights (Figure 8) or criteria values. The strategy assessment particularly respects different temporal dimensions and hence current conditions as well as future uncertainties taking into account characteristics of the underlying decision support method.
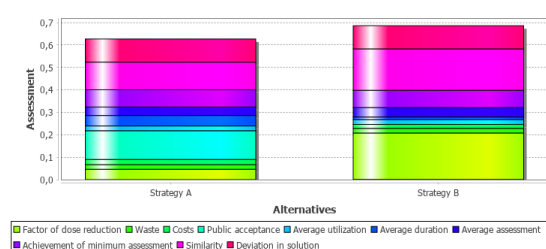
Figure 7: Assessment of strategies illustrated as stacked-bar chart depicting the contributions of criteria values to the overall assessment [10, Figure 6.8]
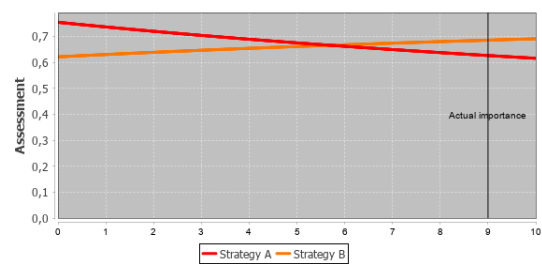
Figure 8: Stability of result according to changes in the weight of 'factor of dose reduction' [10, Figure 6.10]

Summary and Future Work

Multi Criteria Decision Analysis has proven to be a valuable tool for decision making in various interactive workshops. MCDA is relatively easy to apply once the criteria and preferences are agreed upon. It is fast in computation and therefore very interactive in its handling. The setup forces discussions among decision makers and leads to clarity as well as transparency in the decision process. Considering uncertainties in the input improves the interpretation of the results and allows to determine more robust solutions compared to the hitherto existing approach. As a drawback applying MCDA requires knowledge on the method and the consequences of choosing specific criteria or normalisation methods. The setup takes some time as discussions are required among the decision makers to reach a consensus. Therefore, it is best suited for preparation or late phase emergency management where time is less pressing.

Combining MCDA with other decision supporting methods like Agent Based Modelling, Evolutionary Algorithms, or Case Base Reasoning can improve the performance of a decision support system, especially for complex problems like the management of power distribution in urban areas. The growing complexity of dependencies between critical infrastructures and the ongoing urban transformation towards smart cities, challenge crisis management. In particular, there is a lack of knowledge on possible disruption scenarios, the range and se-

verity of cascading effects as well as appropriate management strategies. In the framework of the HGF portfolio security, we are working on robust and comprehensible solutions for crisis management, specifically for maintaining security of supply and protecting critical infrastructures in complex crisis situations. This especially requires an understanding of emergences resulting from numerous interacting system components in an urban area. We have developed an agent based optimisation framework that will be further enhanced by, for example, multi criteria analysis capabilities for agents. Besides global strategies and objectives, individual agents aim at self-preservation and demand-driven supply of services, challenging the assessment of potential strategies and opening up various research possibilities in the context of MCDA.

References

[1]   Müller, T., Duranova, T., van Asselt, E., et al. "D9.36, Report from stakeholder panels and workshops related to the application of the methods and tools developed in ST 9.1.6, Appendix A." CONCERT - Publications, 2019. https://www.concert-h2020.eu/en/Publications.

[2]   Access to Infrastructures for Radiation protection Research, Special Issue 5, Confidence.   https://www.concert-h2020.eu/-/media/Files/Concert/AIR2/Infrastructures_AIR2_Bulletin_Special_issue_Feb_2020.pdf.

[3]   Triantaphyllou, E. "Multi-Criteria Decision Making Methods: A Comparative Study." Dordrecht, The Netherlands: Kluwer Academic Publishers (now Springer), 2000.

[4]   Müller, T. and Raskob, W. "D9.34, Improved MCDA tool for decision making under uncertainty for panels." CONCERT - Publications,   2018.   https://www.concert-h2020.eu/en/Publications.

[5]   Weiss, G. "Multiagent Systems. A Modern Approach to Distributed Artifical Intelligence." MIT press, 2013.

[6]   Bai, S. and Raskob, W. "Agent-based Negotiation Simulation." In 5th NERIS Workshop. Roskilde, Denmark, April 3-5, 2019.

[7]   Bai, S., Mueller, T., and Raskob, W. "D9.35, ABM tool with artificial intelligence: Automated negotiation simulation." CONCERT - Publications,   2018.   https://www.concert-h2020.eu/en/Publications.

[8]   Back, T. "Evolutionary Algorithms in Theory and Practice: Evolution Strategies Evolutionary Programming Genetic Algorithms." Oxford University Press, USA, 1996.

[9]   Aamodt, A. and Plaza, E. "Case-based reasoning: Foundational issues, methodological variations, and system approaches." AI Communications, 7, 1 (1994), 39–59.

[10]   Moehrle, S. "Case-Based Decision Support for Disaster Management." KIT Scientific Publishing, 2020.

[11]   Moehrle, S. and Raskob, W. "Reusing Strategies for Decision Support in Disaster Management – A Case-based High-level Petri Net Approach." In S.Y. Yurish, ed., Advances in Artificial Intelligence: Reviews, Vol. 1. IFSA Publishing, S.L. (Barcelona, Spain), 2019.

[12]   Ievdin, I., Trybushny, D., Zheleznyak, M., and Raskob, W. "RODOS re-engineering: aims and implementation details." Radioprotection, 45, 5 (2010), S181–S189.

[13]   Comes, T., Hiete, M., Wijngaards, N., and Schultmann, F. "Enhancing Robustness in Multi-criteria Decision-Making: A Scenario-Based Approach." In 2nd International Conference on Intelligent Networking and Collaborative Systems, INCoS 2010. Thessaloniki, Greece, November 2010, pp. 484–489.

[14] Ottenburger, S.S. and Ufer, U. "Smart Space and Conrete Risks." In 24th International Conference on Urban Planning and Regional Development in the Information Technology (24th REAL CORP). Karlsruhe, Germany, April 2-4, 2019.

[15] Ottenburger, S.S., Bai, S., and Raskob, W. "MCDA-based Genetic Algorithms for Developing Disaster Resilient Designs of Critical Supply Networks." In ICT-DM 2019: The 6th International Conference on Information and Communication Technologies for Disaster Management. Paris, France, December 18-20, 2019.

[16] Raskob, W., Haller, C., Hasemann, I., Schichtel, T., and Trybushnyi, D. "Source term reconstruction module in JRODOS." In 5th NERIS Workshop. Roskilde, Denmark, April 3-5, 2019.

[17] Raskob, W. and Münzberg, T. "Schmutzige Bomben und ihre möglichen Folgen für die Bevölkerung." Crisis Prevention, Fachportal für Gefahrenabwehr, Innere Sicherheit und Katastrophenhilfe, 2019. https://crisis-prevention.de/feuerwehr/schmutzige-bomben-ihre-moeglichen-folgen-fuer-die-bevoelkerung.html.

[18] Walsh, L., Ulanowski, A., Kaiser, J.C., Woda, C., and Raskob, W. "Risk bases can complement dose bases for implementing and optimising a radiological protection strategy in urgent and transition emergency phases." Radiation and environmental biophysics, 58, 4 (2019), 539–552.

[19] Ottenburger, S.S. "Continuous and Urban Resilient Power Supply During Critical States." In Resilient Cities 2019 : The 10th Global Forum on Urban Resilience and Adaptation. Bonn, Germany, June 26-28, 2019.

[20] Ottenburger, S.S. "Smart Urban Resilience - Implementing Sustainability in a Sustainable Way!" In DAAD Workshop on Sustainable Urban Development in Europe and North Africa. Tunis, University of Carthage, Tunisia, November 22-24, 2019.

[21] Ottenburger, S.S. "Smart Urban Resilience -Smart Grids and Critical Infrastructure Protection." In Conference on Smart Cities and Resilient Infrastructure. Washington D.C., USA, October 3, 2019.

[22] Ottenburger, S.S., Mohr, S., Daniell, J., and Kunz, M. "Integrated Risk Analysis for Safe and Resilient Operation of Dams - Early Warning System for Risk Reduction." In DAMAST (Dams and Seismicity), BMBF-FONA Project - Initial Meeting. Sugdidi, Georgia, October 15, 2019.

[23] Ottenburger, S.S. and Ufer, U. "Quartierspeicher für mehr urbane Resilienz : Ein Blick über den Tellerrand technischer Risiken bei der Energiewende." Transforming Cities 2, 2019, 66–69.

[24] Ottenburger, S.S. "Stromversorgung und urbanes Kontinuitätsmanagement, Versorgungssicherheit 2.0 - Smarte Konzepte zur Erhöhung der Resilienz moderner Städte in Zeiten dezentraler Strombereitstellung." *Transforming Cities 4*, 2019, 60–63.

Group: Hydrogen

Fundamental Behaviour of Hydrogen to Applied Accident Consequence Analysis for Hydrogen as a Safe Energy Carrier

Qingxin Ba, Andrei Denkevits, Guang Hu, Olaf Jedicke, Fan Jiang, Thomas Jordan, Birgit Kaup, Alexei Kotchourko, Mike Kuznetsov, Alexander Lelyakin, Jonas Mohacsi, Frank Prestel, Maria Stassen, Jianjun Xiao, Zhanjie Xu, Yu Zhang, Zhi Zhang

Introduction

In 2019 the Hydrogen Group continued to develop the in-house specialized CFD codes, GASFLOW and COM3D, and conducted several experimental programs to deepen the understanding of the mixing behavior and the transient combustion phenomena, flame acceleration and deflagration-detonation-transition, of accidentally released hydrogen. Members of the group are actively transferring their insights and expertise into the respective IEA Hydrogen Task 37, the standards committees of ISO (TC 197), CEN/CENELEC (TC 6) and in the European Hydrogen Safety Panel. Among other third party funded projects the Hydrogen Group has been conducting ambitious experimental programs for the European Fuel Cell and Hydrogen Joint Undertaking (FCH JU) funded projects PRESLHY - Pre-normative research for the safe use of liquid hydrogen - and HyTunnel-CS - Pre-normative research for safety of hydrogen driven vehicles and transport through tunnels and similar confined spaces. The report for 2019 will focus on some highlights provided by the Hydrogen Group in the field of hydrogen safety in tunnels and confined spaces.

Hydrogen Fire Suppression in Traffic Tunnels

The Hydrogen Group supported by the Pro-Science team has performed more than 600 tests to investigate the effect of mechanical ventilation on hydrogen jet structure and dispersion. The experiment was integrated in the huge test vessel V220, see Figure 1a,b. A powerful fan was installed in one of the two main ports of the vessel. Between the ports a 6 m long test domain was arranged to mimic a scaled down cut-out of a tunnel with an accidental release of hydrogen. Thirty different configurations were examined by changing the H_2 mass flow rate from 1 to 5 g/s and the air flow velocity in the range 1.5- 5 m/s with co-aligned, opposite and tranversal direction of the ventilation flow in relation to the hydrogen jet direction.
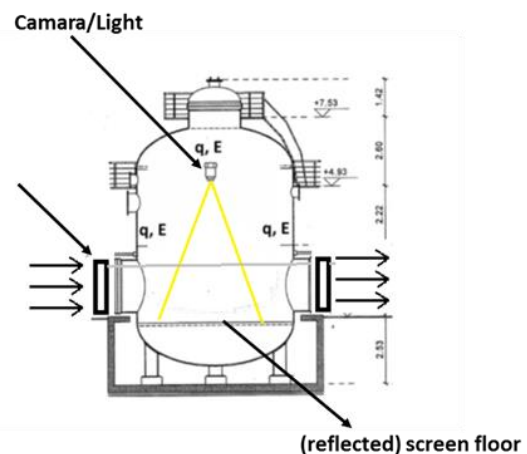

Figure 1: a Experimental set-up of tunnel ventilation experiments in HYKA V220 test vessel;

Figure 1: b View from downstream on the ventilated tunnel segment with central fan

The aim of the experimental campaign was to determine the hazard distances as function of hydrogen mass flow rate, ventilation air flow velocity and relative release direction. It was found that for all examined configurations, the mechanical ventilation led to a considerable size reduction of the pre-mixed cloud defined by the flammable mixture.

Relevant tests have been selected for uploading of the corresponding result files on the Hy-Tunnel-CS open data repository. These data will be further used for code validations.

Hydrogen Fire Suppression in Traffic Tunnels

Fires are representing typical hazards in tunnels and some devastating fire accidents where initiating the development of the European tunnel safety directive [https://eur-lex.europa.eu/legal-content/EN/TXT/PDF/?uri=CELEX:32004L0054&from=en]. As hydrogen fires show some quite distinct characteristics and different behavior compared to conventional fires and the current version of the European tunnel safety directive does not address hydrogen as an alternative fuel, the applicability of conventional mitigation technology has to be evaluated. The suppression effects of installed fire safety systems and the special accidental conditions have been

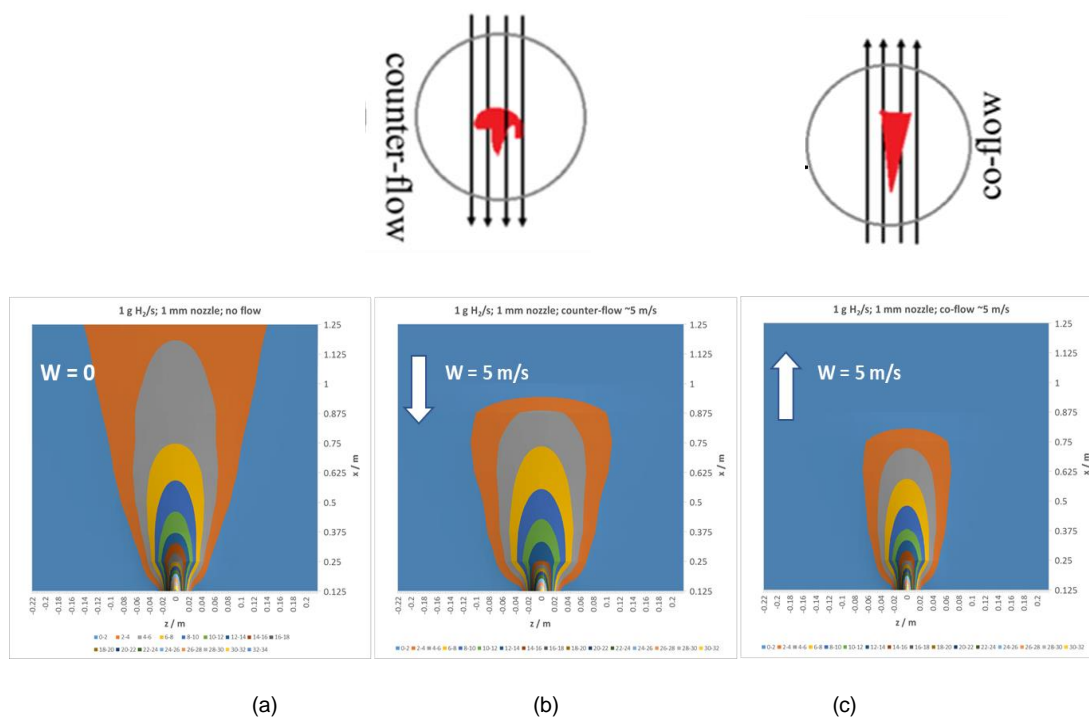(a)   (b)   (c)

Figure 2: Measured concentrations in horizontal plane at height of release nozzle; (a) without ventilation, (b) with counterflow ventilation (c) with co-flow ventilation

studied experimentally and theoretically by numerical simulations.

The CFD code Fire Dynamics Simulator (FDS) [https://www.nist.gov/services-resources/software/fds-and-smokeview], developed by the US NIST and widely used in the fire safety community, has been adopted to analyze the hydrogen fire generated from an accidental release of hydrogen. The simulations account for the effects of water sprays and/or in oxygen starving conditions. The main variations concern the leaking mass flow rates of the hydrogen source, the mass flow rates of water injection, and /or different droplet sizes.

Figure 3 shows the simplified 3D tunnel section which is modeled geometrically together with three cars. One of the cars releases its high pressure hydrogen inventory via a nozzle on the lower rear side, as a primary fire is assumed to open the temperature activated pressure release device (TPRD). The release nozzle pointing backwards from the concerned car, is marked with red color in Figure 3.

(a) Longitudial view
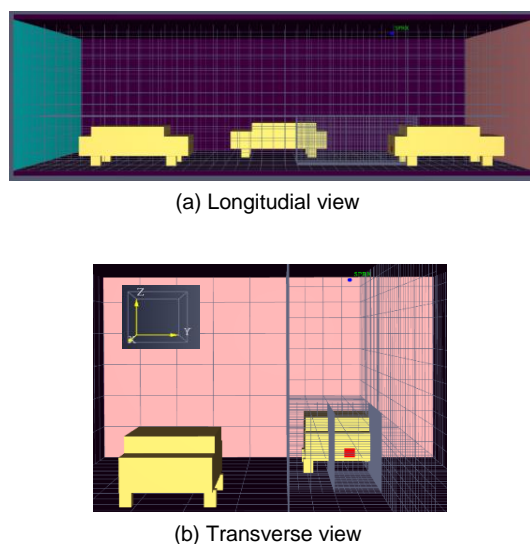

(b) Transverse view

Figure 3: Numerical mesh of the simulated road tunnel segment with 3 cars,
one of them (on the right hand side) releasing hydrogen through a nozzle (red dot)

The gas temperature and gas compositions have been computed with and without water spray and with a variation of oxygen depletion in the concerned tunnel segment, i.e., less than 21 vol. % in normal air. The simulation cases are put together into the following table. The transient thermal state of the gas in the control volumes, e.g., temperature and steam fraction, have been calculated. The results are used to derive recommendations whether the environment in the tunnel is suitable for fire control, evacuation and rescue operations under the heat release rates of the hydrogen fire and for the selected water spray and oxygen depletion conditions.

The following preliminary results are obtained by the FDS simulations. The temperatures of as shown in Figure 4 indicate a cooling effect of the water spray on the fire, although the temperature decrease is not that much due to the relatively low mass flow rate of water in that simulation case. It is interesting that for some cases the gas temperature with spray is higher than without spray (compare black and blue line in Figure 4). The reason for this surprising behavior is, that the hydrogen combustion is intensified by the turbulence and mixing effect induced by the spray droplet momentum.
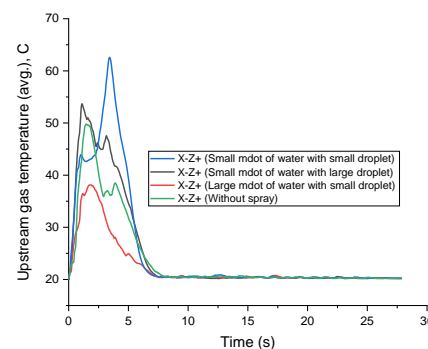

Figure 4: Gas temperature changes in upstream caused by water spray

The humidity (steam fraction) is also computed as it is a classical indicator for the impact on human beings. Obviously, the humidity at tunnel exit is increased due to the operation of water spray. It means that some droplets must evaporate and remove tangible heat of hydrogen fire. However, although this might have an

Table 1.1: Calculation cases of hydrogen fires suppressed by water sprays or oxygen depletions

	Water spray				Oxygen depletion		
	Small mass flow rate of water		Large mass flow rate of water		Slight starving of O_2	Medium starving of O_2	Serious starving of O_2
	Small droplet	Large droplet	Small droplet	Large droplet			
Small mass flow rate of H_2	1	3	5	7	a	c	e
Large mass flow rate of H_2	2	4	6	8	b	d	f

impact on first responders strategies, there is practically no effect of the increased humidity on the reaction kinetics. Another observation is, that a higher water spray mass flux does not further improve the situation.

So, it may be concluded that up to a certain limit a larger mass flow rate of spray brings better cooling effect and produces a higher steam fraction in the gas mixture. In certain conditions the spray may increase turbulence levels and promote faster combustion. The simulations with high degree of oxygen depletion show that even under extreme conditions hydrogen is always burnt almost completely and no flammable mixture is leaving the simulation domain. So a transfer of unburnt hydrogen into another segment or into the ventilation ducts is very unlikely.

Consequence analysis of hydrogen explosions in tunnels

In the more unlikely case of late ignition of released and pre-mixed hydrogen in the tunnel, fire phenomena become less relevant and mitigation of the potential explosion effects becomes more important. Without proper mitigation, the blast waves generated in a local hydrogen combustion event might travel a much longer distance in the tube like tunnel structures than in a free environment. To pro-

vide a reference scenario a typical tunnel accident with late ignition was analysed with the in-house code GASFLOW-MPI [1]. This reference scenario consisted of a tunnel segment with two parallel lanes in the same direction (two separate tubes), with a very mild inclination, but without ventilation or spray activation, i.e. without accounting for any active mitigation technology.
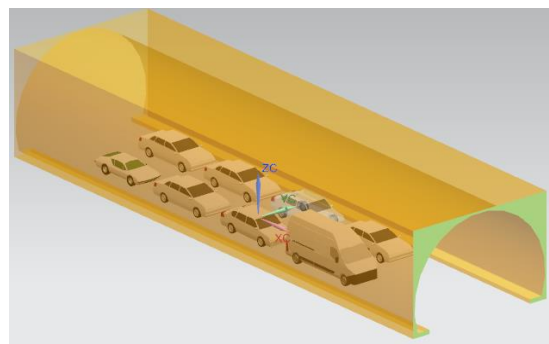
Figure 5: Tunnel segment modeled for late ignition / explosion scenario

It was assumed that the inventory of 5 kg stored at one hydrogen driven car under high pressure is released via the TPRD at the rear of the car, similar as for the fire simulations above. For the release phase GASFLOW-MPI determines the time dependent mass of hydrogen included in the flammable cloud and the potential for a deflagration-to-detonation transition (DDT) in this premixed system (see Fig-

ure 6 top). This information was used to determine the most conservative location and timing for an ignition. So ignition was assumed for maximum flammable mass at about 12.5 s after start of the release in a central position of the premixed cloud with a hydrogen concentration close to stoichiometry (about 30%). The ignition location close to the central ceiling maybe easily motivated, as in tunnels with such a horse-shoe shaped cross-section the electric supply lines for light and ventilation are installed typically there. However, an accidental ignition by a spark is considered a weak ignition source, as it won't initiate a detonation directly.

After the weak ignition GASFLOW-MPI determines the transient pressure loads generated in the deflagration. Although a DDT may not be ruled out, because of the high degree of confinement and obstruction, it is difficult to determine the exact location and further developments of a detonation. However, the loads generated by the deflagration, with local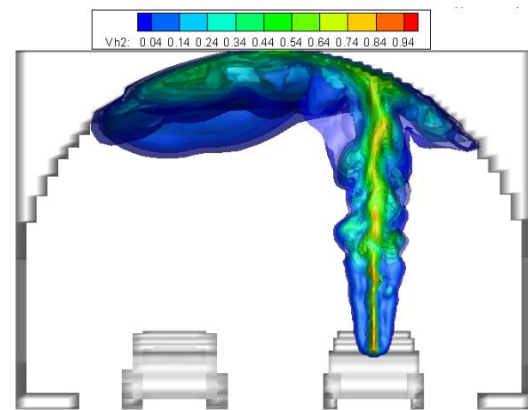 maxima in the order of 3 bar (see Figure 7), are strong enough to damage all involved vehicles seriously and eventually to destroy the tunnel structure.

b) Y-z-cut of hydrogen concentration and the location of ignition

Figure 6: b) vertical cut of flammable cloud at critical ignition time (12.5 s) and critical ignition location (red dot)
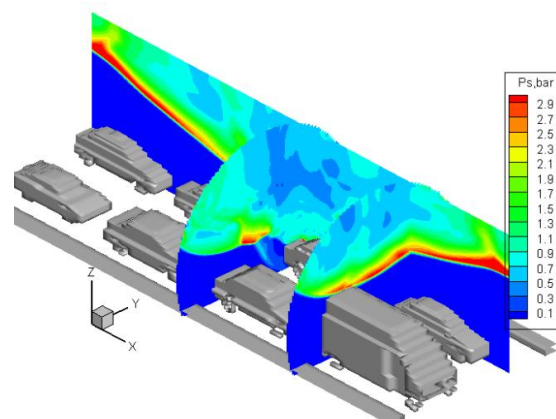
Figure 7: Blast wave caused by hydrogen deflagration reaches the car roofs

a) Hydrogen integral mass and λ criterion in the area

Figure 6: a): time evolution of flammable mass and relative diameter of DDT capable cloud;

It has to be stressed, that this scenario is assumed to have very low probability. It is mainly used as a reference for evaluating the effectiveness of mitigation measures against explosion scenarios. The next chapter describes such an evaluation for water sprays, which are typically installed in larger tunnels.

Study of attenuation effect of water droplets on blast waves

To gain a better understanding, first the different attenuation mechanisms, like momentum

absorption, thermal absorption, reflection and droplet breakup, were systematically assessed with simplified analytical models. Influencing parameters, such as droplet size and liquid phase concentration were analysed. A literature survey provided an overview of similar research and allowed to identify high quality validation data generated in well instrumented experiments.

A suitable droplet model, addressing the main phenomena droplet drag forces and droplet breakup, has been developed and implemented in the COM3D code. The correlations and parameters needed for the drag coefficient and for the breakup time and secondary droplet size have been tuned to reproduce the results published in [A. Chauvin et al. "Investigation of the attenuation of a shock wave passing through a water spray". In: *International Symposium on Military Aspects of Blast and Shock (MABS) 21* (2010). Figure 8 depicts the channel used in these experiments with the high pressure driver region, a low pressure blast wave travel zone and the droplet cloud zone.

The results achieved with the COM3D implemented model are compared to the experimental results in Figure 9. The simulations reproduce the results qualitatively and quantitatively reasonably well. In particular the early

critical phase of droplet atomization is captured very well.
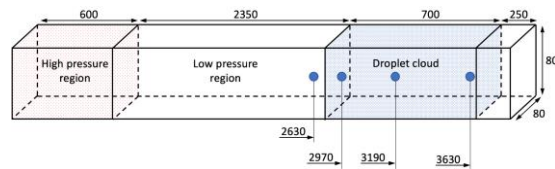
Figure 8: Experimental set-up for the Chauvin experiments

Subsequently, using the developed model, simulations have been conducted to plan middle sized water spray / shock wave interaction experiments in the hydrogen test facility V220 of the hydrogen test center HYKA. Hydrogen is detonated in a combustion unit, what induces a shockwave. The pressure propagation in the absence and presence of a droplet cloud has been computed. The results will be used to tune the experimental layout.

Finally, it is planned to use the COM3D code with these new extensions to assess the mitigating effects of conventional water sprays and modern mist system for hydrogen explosion scenarios in traffic tunnels, as described above.
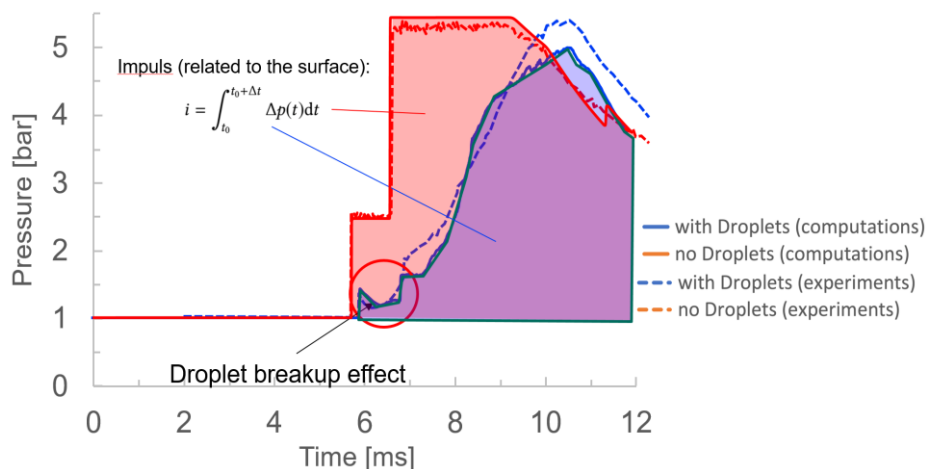
Figure 9: Comparison of COM3D results and measured pressure at point 3190 without (red lines) and with droplet cloud (blue lines)

References

[1]   Li, Y.; Xiao, J.; Zhang, H.; Breitung, W.; Travis, J.; Kuznetsov, M.; Jordan, T.: ANALYSIS OF TRANSIENT HYDROGEN RELEASE, DISPERSION AND EXPLOSION IN A TUNNEL WITH FUEL CELL VEHICLES USING ALL-SPEED CFD CODE GASFLOW-MPI, 8th International Conference on Hydrogen Safety, Adelaide, Australia, 24-26 September 2019.

Group: Energy and Process Engineering

Study of a liquid air energy storage system

Mathieu Champouillon, Elisabeth Schröder, Dietmar Kuhn

With the emergence of renewable energies, the grid becomes more and more complicated to manage. The intermittency of these new means of production increases the need for energy storage solutions.

Against this background the idea of an innovative energy storage system arises which uses electrical energy to liquefied air, then store the liquid phase in a tank in order to compensate the electricity surplus of the grid, and expand it through a turbine when electricity is needed on the network.

The principle of function is given in the following diagram, Fig. 1.
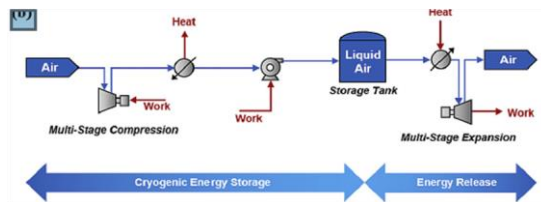

Figure 1: Operating principle of an energy storage system based on air liquefaction.

In the liquefaction part, we need electrical energy to run the compressors and the pumps. During this process, thermal energy could be extracted from the compression (losses), and from the cooling of air to its boiling temperature. For the expansion part, heat is needed to evaporate the liquid air and to improve the expansion in the turbine.

For this study, only the liquefaction part will be investigated. The feasibility and efficiency consideration of the evaporation system will be examined in a future work.

The liquefaction of air goes back to Carl von Linde and W. Hampson who both registered a patent for gas separation in 1895. It is the easiest cycle and contains one or two heat exchangers for cooling the compressed air by the recirculating cold gaseous phase below the inversion temperature.

Later, many other circuits were developed to improve energy efficiency through additional cooling and compression stages upstream of the expansion valve [1-9]. The Claude Cycle for instance uses three heat exchangers in a row. After the first heat exchanger, the compressed air flow is devided in two flows. One air stream passes through the liquefaction line, the second stream is expanded in a turbine and after mixing the turbine exhaust air with the recirculating cold air of the liquefaction line it is used as cooling media in heat exchanger two. Some of the compression energy can thus be recovered but additional plant components are necessary. Another variant of the Claude Cycle is the Kapitza Cycle, whereby the third heat exchanger is removed. Although both cycles are more efficient than the Linde-Hampson Cycle this study deals with the latter for simplicity. In order to find out if the air liquefaction process can be coupled to power generation processes, for instance ORC-Cycles, the influence of parameter variations on a Linde-Hampson process is studied.

In Fig. 2 the Linde-Hampson Cycle is illustrated and the process steps are numbered.
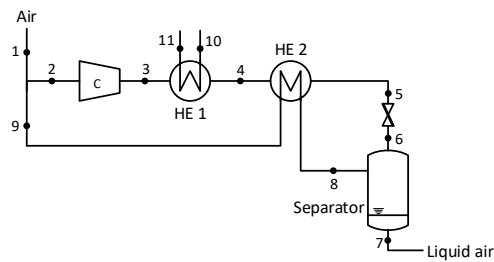
Figure 2: Linde-Hampson cycle

At ambient pressure, fresh air (1) is mixed with the recirculating cold air (9) to the inlet air (2) of the compressor (C). The mass flux at position (2) is m. After the compressor, the air pressure is enhanced to 200 bar (3). The compressed air is then cooled in an externally chilled heat exchanger to state (4). A second heat exchanger, operated by internal heat exchange, reduces air temperature close to air condensation temperature (5). After isenthalpic expansion in the throttle valve air pressure is reduced to ambient pressure (1.015 bar) thus causes the temperature to be lowered to the condensation temperature of -194.3°C (6). In the separator, gaseous (8) and liquid phase (7) are separated and the gaseous air (8) is further used in heat exchanger 2.

The air states can be calculated as follows based on mass flux m at point 2, whereby x is the mass fraction of gaseous air:

Ambient condition:	$T_1 = 293.15K$, $p_1 = 1.015$ bar, fixed values
Ideal mixing of fresh and recirculated air	$T_2 = xT_9 + (1 - x)T_1$, $p_2 = p_1$, whereas x corresponds to mass fraction of recirculating air
Isothermal compression:	$T_3 = T_1$, $p_3 = 200$ bar, fixed values
Cooling in HE 1:	$h_4 = (1 - \eta_{cool}) \cdot h_3$ with efficient coefficient η_{cool} T_4 can be calculated from h_4 by using REFPROP database for instance, $p_4 = p_3$

Isenthalpic expansion at valve:	$h_5 = h_6$, $p_5 = p_3$
Boiling point at ambient pressure:	$T_6 = -194°C$, $p_6 = 1.015$ bar
Gaseous phase at boiling point	$T_7 = T_6$, $p_7 = p_6$, $m_7 = (1 - x) \cdot m$
Liquid phase:	$T_8 = T_6$, $p_8 = p_6$, $m_8 = m \cdot x$
Adiabatic cooling in HE 2	$T_9 = T_8 + (T_4 - T_5) / x$, $p_9 = p_6$

What can be seen from the formulas above, x and η_{cool} cannot be varied independently. Some physical limitaions have to be considered. In both heat exchangers, the cold fluid cannot be hotter than the hot one. That leads to following restrictions in HE 2: $T_4 > T_9$ and $T_5 > T_8$. This could not be respected when x or η_{cool} are too low. In Fig. 3 temperatures T_4 and T_9 are shown as function of η_{cool} for given x=0.5.
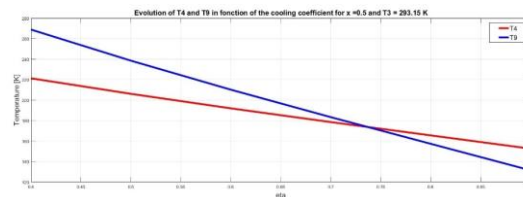
Figure 3: Temperatures T_4 and T_9 depending on η_{cool} for given x = 0.5

As shown in Fig. 3 for x = 0.5, η_{cool} has to be higher than 0.74 which means that the efficiency of HE 1 is restricted in order to provide a minimum cooling rate. Depending on the amount of liquid air (1-x), the first stage cooling in HE 1 is predefined. In addition following criteria for HE 1 has to be fulfilled as well: $T_4 > T_{10}$ and $T_3 > T_{11}$. Therefore, a specific external cooling process must be adapted to the specific temperature level.

In order to understand the behaviour of the system, the influence of the liquid rate (1-x) and the cooling coefficient η_{cool} on the temperatures and the enthalpies of each point are analysed. The interesting values are:
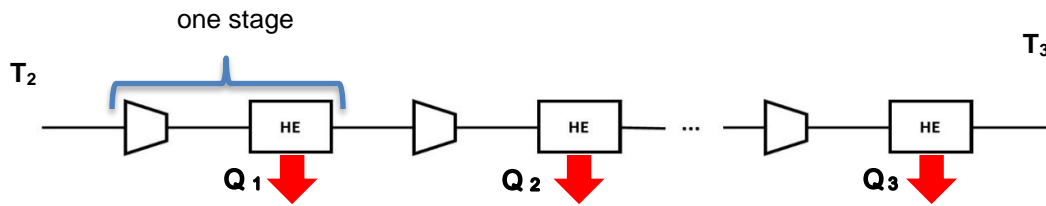
Figure 4: Multi-stage compression with heat extraction

- Temperature at point 4 (T_4)

- Temperature at point 9 (T_9)

- Enthalpy extracted between 3 and 4 (Δh_{34}) in HE 1

- Maximal temperature of the compressor, like if there were not any cooling (T_{comp})

- Enthalpy that could be extracted by the compressor cooling system

The respective parameters are varied in order to examine how much heat can be extracted by combining air liquefaction with external processes. Possible combinations are identified. First, compression heat is used for warming up the working fluid of an external ORC-process of a geothermal energy plant. For this purpose the air compression must be operated in several stages in order not to overheat the compressor. Second, the influence of liquid air ratio (1-x) on the efficiency of HE 1 (η_{cool}) and third, the extraction of gaseous air prior to mixing are investigated.

Influence of parameters

In order to study the influence of parameter variation like x or η_{cool} the isothermal compression is supplemented by a multi-stage adiabatic compression for both enhancing the total energy extraction from the circuit and avoiding overheating of the compressor during adiabatic operation, as shown in Fig. 4. This method allows to increase the released energy

yield and to use it technically in another process.

For each stage, we consider an adiabatic compression and then an isobaric heat exchange. The heat exchange can be effected by another system (ORC p.e.). The compression ratio is the same for each compressor:

$$\frac{T_{i+1}}{T_i} = constant\ at\ each\ stage. \qquad (1)$$

It is important to notice that the temperature after each heat exchanger (including T_3) depends on the system used to cool down the air, because its minimal value is the temperature of the inlet of the cooling fluid. After the last stage, it is assumed, that T_3 remains at 20°C like in the isothermal case. The total heat which can be used in external processes is defined as heat extracted in the compression stages and heat released in HE 1. As described below the total heat release depends on x and η_{cool} and is shown in Fig. 5.

Influence of η_{cool} on heat extraction in HE 1

In this examination the liquid air ratio is kept constant at (1-x) = 0.1 whereas η_{cool} is varied between 0 and 0.7. The efficiency of HE 1 is determined by the value of η_{cool} whereby η_{cool} = 0 indicates that no heat is extracted in HE 1. Both a one-stage and two-stage compression is regarded and the total heat, provided by adiabatic compression and by HE 1 is shown in Fig. 5
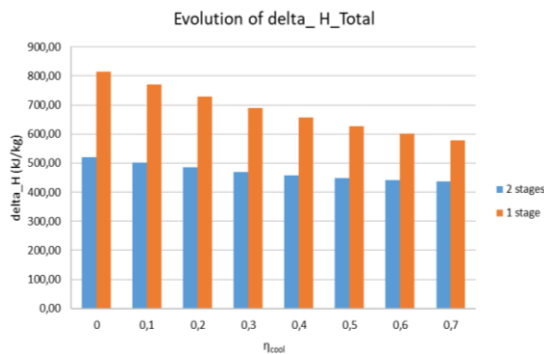
Figure 5: Evolution of the total recovered enthalpy for different values of η_{cool}

ature limit of 500°C for the compressor into account, a one-stage compression cannot be realized.
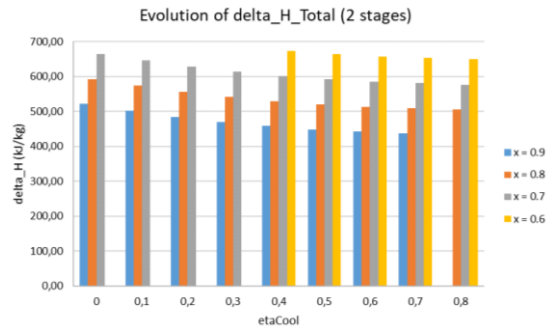
Figure 6: Total enthalpy recovered as function of x and η_{cool}.

Here we can see that when η_{cool} is increasing, the total enthalpy recovered by cooling systems Δh_{total} is decreasing. While the enthalpy between 3 and 4 that is extracted in the HE 1 is higher, the compression enthalpy is even lower because T_2 is decreasing a lot, until 111 K for $\eta_{cool} = 0.7$.

If η_{cool} were greater than 0.7, the temperature T_9 would be lower than the boiling temperature, which is impossible because we need gaseous air in this part.

When the number of compression stages increases, the total enthalpy recovered by cooling systems is lower (-36% for 1 to 2 stages), because the maximum temperature of the compression is lower. But the influence of η_{cool} is also reduced: for a one-stage compression, the difference of total enthalpy recovered is 230 kJ/kg for $0 < \eta_{cool} < 0.7$, but only 80 kJ/kg for a two-stage compression.

The choice of η_{cool} depends on the type of cooling system. If the user prefers to give a lot of energy through HE1, he will have better to increase η_{cool}, but if he wants to recover as much energy as possible, he will have to decrease η_{cool} to take advantage of the compression. It has to be mentioned here, that a one-stage adiabatic compression leads to unreasonable high temperatures of 773°C which cannot be tolerated because which would lead to the destruction of the compressor. Taking a temper-

As a consequence of the increasing yield of liquid air, the recirculated cold air (indicated as x) decreases, whereby the mixture temperature T_2 is increased. Therefore, more energy is released, in the compression heat exchangers and in HE 1, so that the total enthalpy (delta_H_total) increases, as shown in Figure 6. One more time, it is important to notice that some values are physically impossible: $\eta_{cool} < 0.4$ for x = 0.6 and $\eta_{cool} > 0.7$ for x = 0.9.

The goal of this storage system is to liquefy air in order to store energy. When x decreases, more liquid air can be produced. The previous results are therefore good news since the system allows to create more liquid air, while recovering more energy in the cooling systems. But the main problem of decreasing x is the significant limitation of the operating ranges for many parameters. For example, η_{cool} must be between 0.4 and 0.8 for x=0.6.

Influence of temperature T_3 (entrance of HE 1)

This temperature corresponds to the minimum temperature of the compressor cooling system and the maximal temperature for the HE 1. This means that the value of T_3 will be decisive concerning the choice of the system used to cool down the air in the compressor and the first heat exchanger.

Figure 7: Influence of T_3 on recovered enthalpy from compressor cooling system and HE 1

Figure 8: Influence of air extraction ratio y prior to mixing on total recovered enthalpy

The temperature of 60°C corresponds to the minimum temperature of a district heating system, and the temperature of 120°C has been chosen arbitrarily to see the behaviou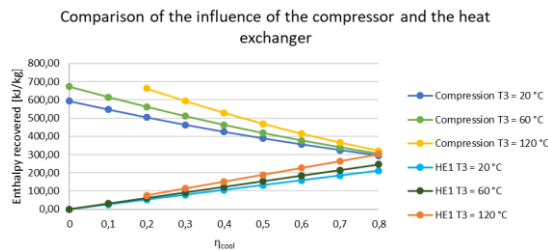r of the enthalpy at high temperature. It can be seen from Fig. 7 that the higher the temperature T_3, the higher the total enthalpy recovered in the compressor and in the HE1. The second effect of the increase of temperature is the tightening of the range of η_{cool} values, for instance: with $T_3 = 120°C$, η_{cool} must be higher than 0.2. From Fig. 7 it can further be seen the impact of the enthalpy recovered during the compression. For low values of η_{cool}, the difference of the total enthalpy recovered is mainly due to the compression, with increasing impact of HE 1 for higher values of η_{cool}.

Influence of cold air extraction between point 8 and 9

At the point 9, we have got cold air with a mass flow rate of x that could be used for another application instead of being recycled in the cycle at the point 2. The idea is to extract a certain amount of air at the point 9, with a mass flow rate of y. This modification has not a significant impact on the system because it modifies only the temperature 2, which tend to $T_{ambient}$ when y tend to x.

The main result as can be seen from Fig. 8, is that the enthalpy extracted during the compression and in the HE1 is increasing with y and η_{cool}. This happens because the temperature T_2 is increasing when the remaining mass flow rate of the point 9 decreases, so the energy released by the compression will be higher.

Conclusion

This study provides a more detailed insight into the Linde-Hampson cycle for the liquefaction of air as an energy storage medium. Many parameters were varied to investigate their influence on the overall process. As a result of this study, coupling possibilities to other power generation processes, e.g. ORC cycles, are easier to identify.

References

[1]   E. Borri, A. Tafone, A. Romagnoli, G. Comodi: A preliminary study on the optimal configuration and operating range of a "microgrid scale" air liquefaction plant for Liquid Air Energy Storage, Energy Conversion and Management 143 (2017) 275–285

[2]   R. Morgan, S. Nelmes, E. Gibson, G. Bret: Liquid air energy storage – analysis and

first results from pilot scale demonstration plant, Applied Energy 137 (2015) 845–853

[3]   I. Lee, J. Park, I. Moon: Conceptual design and exergy analysis of combined cryogenic energy storage and LNG regasification processes: Cold and power integration, Energy 140 (2017) 106-115

[4]   R.F. Abdo et al.: Performance evaluation of various cryogenic energy storage systems, Energy 90 (2015) 1024-1032

[5]   X. Peng, X. She, Y. Li, Y. Ding: Thermodynamic analysis of Liquid Air Energy Storage integrated with a serial system of Organic Rankine and Absorption Refrigeration Cycles driven by compression heat, Energy Procedia 142 (2017) 3440-3446

[6]   M. Antonelli, S. Barsali, U. Desideri, R. Giglioli, F. Paganucci, G. Pasini: Liquid air energy storage – Potential and challenges of hybrid power plants, Applied Energy 194 (2017) 522–529

[7]   T. H. Cetin, M. Kanoglu, N. Yanikomer: Cryogenic energy storage powered by geothermal energy, Geothermics 77 (2019) 34–40

[8]   S. Hamdy, T. Morosuk, G. Tsatsaronis: Cryogenic-based energy storage: Evaluation of cold exergy recovery cycles, Energy 138 (2017) 1069-1080

[9]   A. Sciacovelli, A. Vecchi, Y. Ding: Liquid air energy storage with packed bed cold thermal storage – From component to system level performance through dynamic modelling, Applied Energy 190 (2017) 84–98

Group: Framatome Professional School

Blockage formation experiments in a water rod bundle

Karsten Litfin, Jasmin Klupp, Andreas Class

Introduction

Solid particles flowing into (or within) the core of a nuclear reactor can block one or more sub-channels of a fuel assembly. As they do not affect substantially the outlet conditions (temperature, pressure), they can go unnoticed by the global instrumentation. However, they lead to local heat transfer degradation and the corresponding increase of the cladding temperature. Under certain conditions, depending among others on the size, location and porosity of the blockage, this can result in local fuel cladding failure. Thus, a deep understanding of the formation and main characteristics of these blockages is essential for the development and safety assessment of innovative reactor concepts based on heavy liquid metal coolant, i.e. with particles, that have usually lower density than the coolant.

Former intensive test programs on particle formation in sodium and water-based systems [1], [2] cannot or can only limited be transferred to heavy liquid metal (HLM) cooled reactors, as they are based on particles with higher density than the coolant [3]. For this reason, dedicated experiments with the proper density ratio are mandatory.

For these tests, a 19-pin hexagonal fuel bundle mock-up in a transparent flow channel subjected to a water flow seeded with buoyant particles of relevant density, size, shape and wetting properties has been set up at the Karlsruhe Liquid Metal Laboratory corresponding to the dimensions of the Lead-Bismuth (LBE) cooled MYRRHA research reactor projected in Mol, Belgium.

The nature of the blockage as well as the formation is characterized by optical measurements, supplemented by flow rate, pressure drop and temperature measurements. For the handling of the particles, both an injection (upstream of the test section) and extraction (downstream) subsystem has been implemented into the existing facility. The density ratio liquid/particle was to fulfil the applicable scaling laws between the water tests and the HLM reactor.

Experimental Setup

The KALLA water loop was originally used for water rod bundle experiments in the framework of EU-Project DEMETRA. A complete description of the experiments and the loop design can be found here [4].

The maximum flow rate of the loop is 130m³/h with a pressure head of 14.7 bar. The active loop inventory is 80l, the maximum total inventory is about 8m³. The loop is equipped with a heat exchanger to keep a constant fluid temperature and a cleaning system to remove used particles. Due to the PMMA test section the temperature is limited to 50°C. The flow rate is measured by a commercial flow-meter.

Rod bundle test section

The geometrical details of the 19-pin rod bundle for the blockage formation and growth experiment is shown in Figure 1, the comparison between the experimental setup and the conditions in the MYRRHA reactor rod bundle in Table 1. A detailed figure and a picture of the test section including the particle injection is given in Figure 2.
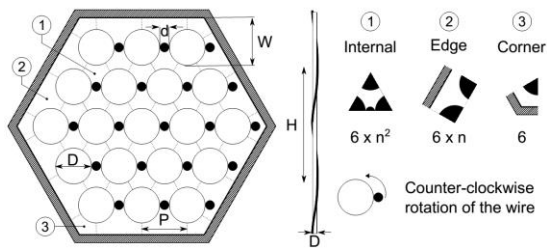
Figure 1: Water rod bundle geometry

Table 1: Geometric parameters used for the test section compared with MYRRHA reactor core geometry

Parameter	Symbol	MYRTE test at KALLA	MYRRHA	Ratio
Number of rods, -	N	19	127	0.15
Rod outer diameter	D, mm	6.55	6.55	1
Distance between rod centers (pitch)	P, mm	8.378	8.378	1
Pitch-to-diameter ratio	P/D, -	1.279	1.279	1
Flat-to-flat distance	FF, mm	39.5	97.55	0.4049
Wall distance	W, mm	8.5139	8.5166	≈ 1
Wall distance-to-diameter ratio	W/D, -	1.2998	1.3002	≈ 1
Wire diameter	d, mm	1.80	1.80	1
Wire pitch	H, mm	262	262	1
Wire pitch-to-diameter ratio	H/D, -	40	40	1
Total length	L, mm	655	1400	0.467
Total length-to-wire pitch ratio	L/H, -	2.5	5.4	0.467
Flow area (complete bundle)	A_{bdl}, mm²	662.6	3638.6	0.1821
Hydraulic diameter (complete bundle)	$d_{h,bdl}$, mm	4.173	3.966	1.052
Flow area (internal sub-channels)	A_{sch}, mm²	12.273	12.273	1
Hydraulic diameter (internal sub-channels)	$d_{h,sch}$, mm	3.743	3.743	1

Figure 2a: Detailed drawing of the foot part of the test section with the particle insertion (left) and the optical parts of the MYRTE test section (right).

Figure 2b: Picture of the mounted test section

Instrumentation

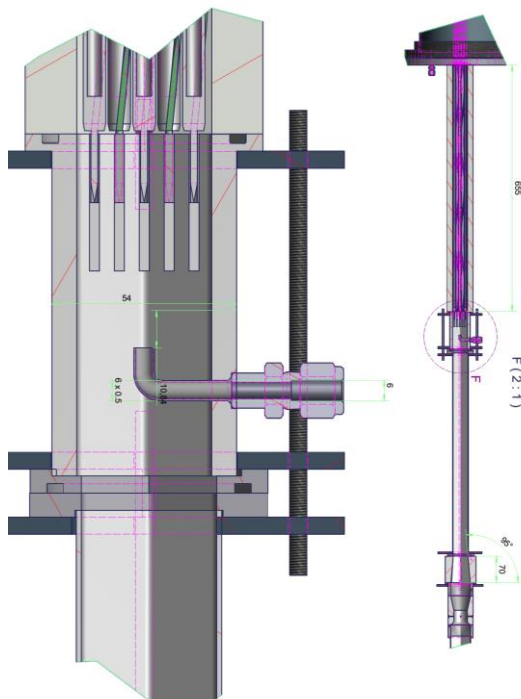The PMMA housing offers direct optical access to the blockages through the PMMA casing of the rod bundle. However, this access is restricted to the outer sub channels only as shown in Figure 3.

Figure 3: Picture of a blockage in the wall sub channel through the PMMA casing

The blockages of the inner sub channels are optically detected by an endoscope that is inserted in one of the PMMA tubes of the rod bundle as depicted in Figure 4. As the endoscope is equipped with it's own light source, further illumination of the investigated part of the rod bundle is not necessary.

The use of this endoscopic system is a result of a comparison of different measurement techniques for the detection of the expected blockages by J. Biernath in his Master thesis [5]. It turned out that acoustic measurements are not suitable for this experiment as the complicated movement of the UDV (ultrasonic doppler velocimetry) sensor heads and the expected interference signals prohibit a reliable detection of the blockage. From the optical measurements the endoscope was the easiest and most reliable option.
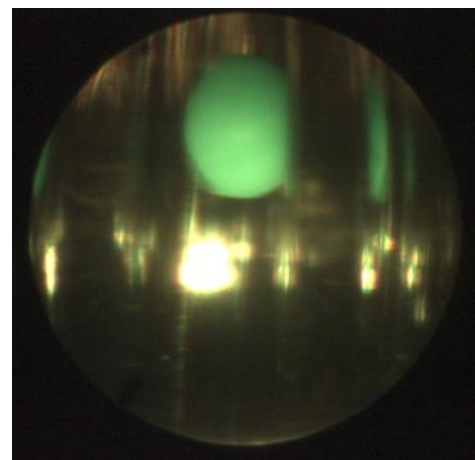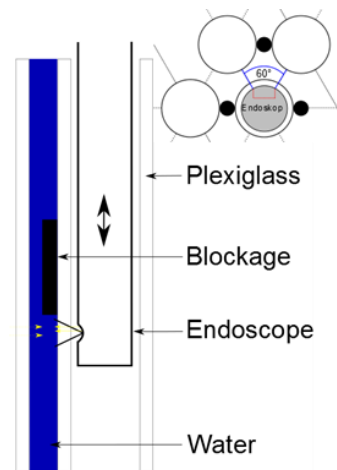
Figure 4: Scheme of an endoscope inserted into the rod-bundle mockup for blockage investigation (top) and a detected particle (bottom)

Experiments

For the blockage experiments, polypropylene particles with the density of 0.946g/cm³ were used to simulate possible blockage formation of Lead oxide in LBE as the density ratio is very similar as shown in Table 2.

Table 2: Density of blockage material for the experiment

Material	Observation	$\rho_{p,MYRRHA}$ kg m^{-3}	$\frac{\rho_{p,MYRRHA}}{\rho_{LBE}}$	$\rho_{p,MYRTE}$ g cm^{-3}
Stainless steel (DIN 1.4571)	At 270°C [20]	7756	0.7474	0.746
Lead oxide (PbO)	At 20°C [7]	9530	0.9184	0.917
Iron oxide (magnetite, Fe_3O_4)	At 20°C [7]	5180	0.4992	0.498
Oxide fuel (MOX, 5% porosity)	At 20°C [3]	10565	1.0181	1.016

In total 4 different experimental series have been performed with particle sizes from 1.5mm to 4.0mm diameter:

- particles that cannot pass the pin fixer followed by smaller particles

- particles that pass the pin fixer but are likely to get stuck in the sub channel

- high amount of irregular shaped particles that get stuck at the pin fixer and cause a noticeable pressure loss

- one pre blocked sub channel and small particles that should not cause a blockage formation.

The first experiment of the series is presented in this report where in 3 steps 180 particles with 3.0mm diameter followed by 70 particles with 2.0mm diameter were inserted into the flow upstream the rod bundle test section.
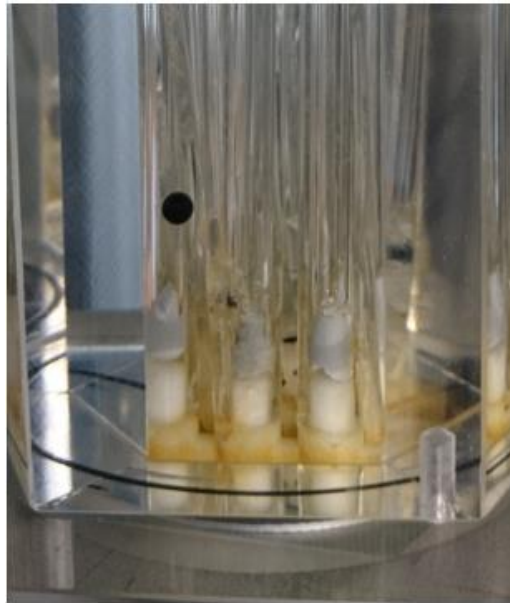
Figure 5b: One particle in a wall sub channel

Insertion of 20 particles with 3.0mm diameter

Figure 5 shows the test section after insertion of the first 20 particles (black spheres). Most particles are captured in the pin-fixer as the diameter is too big for the inner sub-channels. One particle passed the pin fixer and finally was captured in a wall sub channel. During the 20 minutes of insertion the flow rate decreased by 3% and the pressure loss of the test section increased by 1%. None of the particles was able to pass the test section.

Insertion of 160 more particles with 3.0mm diameter

During the second run, 160 more particles (white spheres) of 3.0mm diameter are inserted into the primary flow. Again, most particles are captured in the pin-fixer and a small fraction of 15 particles go into the wall sub channels. In total 3 wall sub channels are affected and blockages with an axial extension of up to 9 particles are visible as shown in Figure 6. Further decrease of flowrate and increase of pressure loss is depicted in Table 3.

Figure 5a: 19 particles of 3.0mm diameter in the pin fixer

Figure 6a: Insertion of 160 more 3.0mm particles. Pin fixer
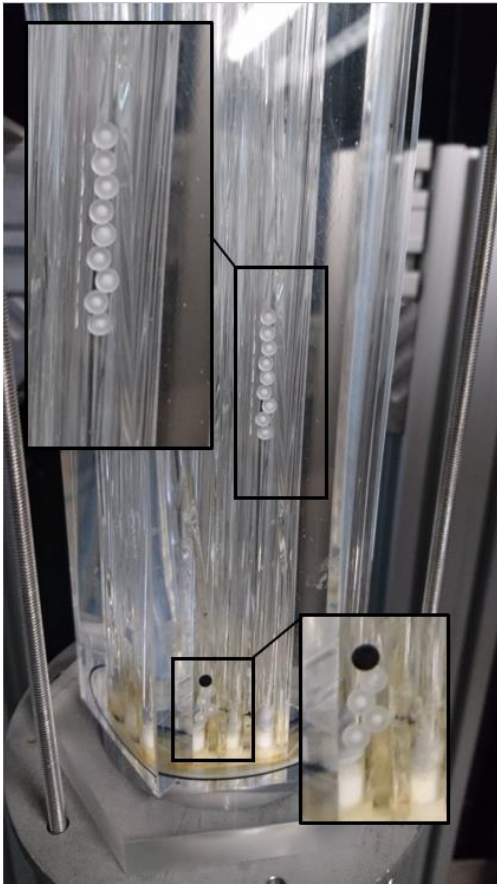
Figure 6b: Insertion of 160 more 3.0mm particles. Affected wall sub channels

Insertion of 70 particles with 2.0mm diameter

After the pin fixer and the wall sub channels have been blocked with a total of 180 particles with 3.0mm diameter, the blockage was probed with the insertion of particles with 2.0 mm diameter.

Most of the smaller particles are captured in the pin-fixer by the present 3.0mm particles. 4 particles moved into a pre-blocked wall sub channel and 1 particle was able to enter an inner sub channel and got blocked there. This is shown in Figure 7. During the complete run, a further flow rate decrease and pressure loss increase was measureable and is shown in Table 3. After the run, the complete test section was dismounted, cleaned and investigated. No particle was able to pass the test section. The

set up of the experiment as well as the complete 1st run was part of a Bachelor Thesis and is described more detailed elsewhere [6]. The other experimental runs are also described in detail elsewhere [7].

Figure 7: Insertion of 2.0mm particles in green into the pre-blocked test section. Pin fixer (top), wall sub channels (middle) and inner sub channel (bottom)

Table 3: Flow rate and pressure loss during the first experiment

Particles	20 @ 3.0	160 @ 3.0	20 @ 2.0	∑
Flow rate decrease	3,5%	19,5%	2,5%	25,5%
Pressure loss increase	1,5%	9%	2,5%	13%

Concluding remarks

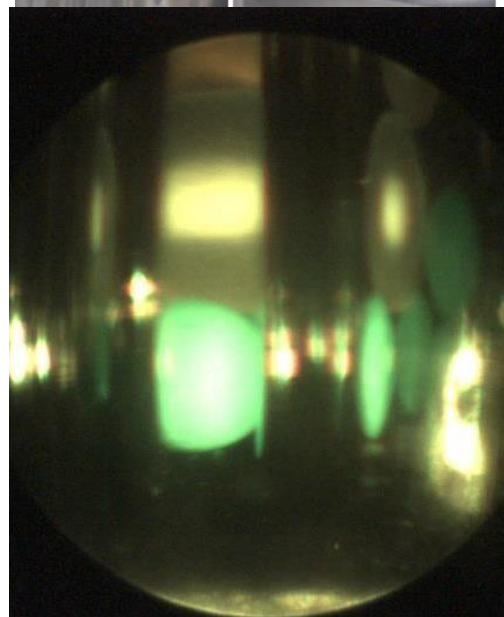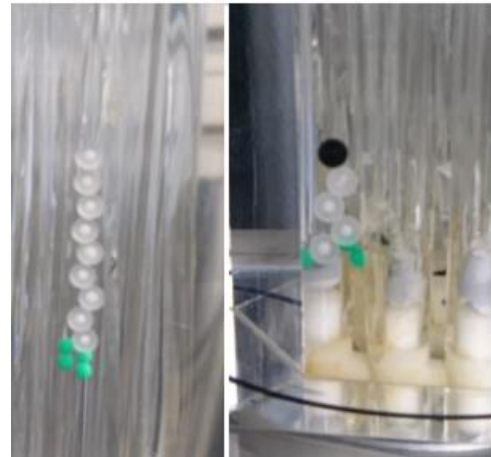The 4 performed experimental series show some predictable but also some new results and insights into the blockage formation in wire wrapped rod bundles.

The first experiment, a blockage using 3.0mm particles that attach at the pin fixer and the wall sub channel followed by smaller 2.0mm particles shows that even with 180 particles not all sub channels are blocked and still smaller particles can pass by. However, they are very likely to attach to the existing big particles. The changes in pressure loss and flow rate are even for this large amount of particles very low.

The second experiment was a blockage using 2.0mm particles that theoretically should be able to pass the pin fixer and the test section. In contrast to the geometrical preconditions several blockages with almost half of the inserted particles was observed.

The third experiment was a blockage using a huge amount of particles that mainly blocked the pin fixer but also formed large axial extended blockages in the wall sub channels. Here, a high influence on flow rate and pressure drop was detected.

The fourth experiment was the use of small 1.5mm particles that easily should pass the pin fixer and the test section but could attach to an existing blockage. Here, it was observed that on the one hand they form temporary blockages that disappear and on the other hand, that no particle attaches to the existing blockage even as the particles were inserted into the same sub channel.

Finally we can conclude from the experiments:

- Most of the measured blockages have a quite small axial extension.
  The probability of blockage agglomeration with a large axial extension is not very high as the particle size must be large enough not to be able to follow the enhanced crossflow upstream the blockage on the one hand but also must be small enough to meet the geometrical restraints at the pin fixer to enter the sub channel.

- All particle sizes from 1.5mm form blockages

- Existing Blockages enhance crossflow and reduce agglomeration of small particles

- 1.5mm particles are able to follow the sub channel crossflow, the 2.0mm particles aren't and agglomerate on a excising blockage.

Acknowledgements

References

[1] Schultheiß, G. (1976). Analyse der Bildung lokaler Kühlungsstörungen in schnellen natriumgekühlten Brutreaktoren. Technical Report KFK 2331, Gesellschaft für Kernforschung mbH., Karlsruhe.

[2] Schultheiß, G. (1977). Model for formation and growth of local blockages in grid spaced fast sodium cooled breeder fuel elements. Nuclear Engineering and Design 43 (2), 329 – 341.

[3]   Van Tichelen, K. (2012, December). Blockages in LMFR fuel assemblies. Literature review. Technical Report SCK•CEN-R-5433, SCK•CEN.

[4]   Litfin, K. (2009) Final report for the fuel bundle experiment in KALLA, EU-Project EU-ROTRANS, Contract no.: FI6W-CT2004-516520, Domain DM4 DEMETRA, Deliverable D4.68

[5]   Biernath, J. (2015) Bildung von Hindernissen durch Ansammlung von Partikeln in einer Strömung entlang eines Stabbündels: Planung eines experimentellen Aufbaus zur Charakterisierung der Messtechnik. Masterarbeit, Karlsruhe Institute of Technology

[6]   Klupp, J. (2018) Charakterisierung von Partikelablagerungen in einem Stabbündel. Bachelorarbeit, Duale Hochschule Baden-Württemberg, Karlsruhe

[7]   Litfin, K. (2019) Final report on the KALLA blockage formation test results, EU Project Myrte, Contract no.: 662186, Deliverable D3.24

List of Publications

[1]   Albrecht, G.; Gabriel, S.; Detailed investigations on flow boiling of water up to the critical heat flux. Annual Report 2017-2018 of the Institute for Nuclear and Energy Technologies. Ed.: T. Schulenberg, 37–42, KIT Scientific Publishing, Karlsruhe. Volltext der Publikation als PDF-Dokument

[2]   Albrecht, G.; Heiler, W.; Büttner, F.; Gabriel, S.; Experimental investigation of air entrainment by a vertical jet plunging into a liquid pool. 10th International Conference on Multiphase Flow, Rio de Janeiro, BR, May 19-24, 2019, Paper No: OC.134.

[3]   Albrecht, G.; Meyer, L.; Zhang, R.; Ex-Vessel Fuel Coolant Interaction Experiment with the Geometry of an AP1000 Reactor. 18th International Topical Meeting on Nuclear Reactor Thermal Hydraulics (NURETH-18), Portland, Oregon, USA, August 18-23, 2019., 4004–4017, ANS, LaGrange Park, Ill.

[4]   Ami, T.; Schulenberg, T.; Prediction of wetting phenomena of a microlayer of gas bubbles. International journal of heat and mass transfer, 133, 769–777. doi:10.1016/j.ijheatmasstransfer.2018.12.143

[5]   Bai, S.; Staudt, C.; Raskob, W.; Knowledge Database and Regionalization of JRODOS in the HARMONE Project. 4th NERIS Workshop Proceedings, CERN, Fontenay-aux-Roses.

[6]   Bai, S.; Raskob, W.; Agent-based Negotiation Simulation. 5th NERIS Workshop (2019), Roskilde, Dänemark, 3.–5. April 2019.

[7]   Batta, A.; Class, A.; CFD validation of fuel assembly flow. Annual Report 2017-2018 of the Institute for Nuclear and Energy Technologies. Ed.: T. Schulenberg, 77–83, KIT Scientific Publishing, Karlsruhe. Volltext der Publikation als PDF-Dokument

[8]   Batta, A.; Class, A.; Thermalhydraulic CFD Validation for Liquid Metal Cooled 19-Pin Hexagonal Wire Wrapped Rod Bundle. 18th International Topical Meeting on Nuclear Reactor Thermal Hydraulics (NURETH-18), Portland, Oregon, USA, August 18-23, 2019, 655–665, ANS : LaGrange Park, Ill.

[9]   Batta, A.; Class, A. G.; Pacio, J.; Validation for CFD Thermalhydraulic Simulation for Liquid Metal Cooled Blocked 19-Pin Hexagonal Wire Wrapped Rod Bundle Experiment Carried out at KIT-KALLA. 50. Jahrestagung Kerntechnik (AMNT 2019), Berlin, Deutschland, 7.–8. Mai 2019.

[10]   Bechta, S.; Ma, W.; Miassoedov, A.; Journeau, C.; Okamoto, K.; Manara, D.; Bottomley, D.; Kurata, M.; Sehgal, B. R.; Stuckert, J.; Steinbrueck, M.; Fluhrer, B.; Keim, T.; Fischer, M.; Langrock, G.; Piluso, P.; Hozer, Z.; Kiselova, M.; Belloni, F.; Schyns, M.; On the EU-Japan roadmap for experimental research on corium behavior. Annals of nuclear energy, 124, 541–547. doi:10.1016/j.anucene.2018.10.019

[11]   Breitung, W.; Halmer, G.; Kuznetsov, M.; Xiao, J.; Analysis of transient supersonic hydrogen release, dispersion and combustion. International journal of hydrogen energy, 44 (17), 9089–9099. doi:10.1016/j.ijhydene.2018.04.158

[12]   Bubelis, E.; Chauvin, N.; Davies, U.; Gianfelici, S.; Gicquel, S.; Krepel, J.; Lainet, M.; Lavarenne, J.; Lindley, B.; Mikityuk, K.; Murphy, C.; Perrin, B.; Pfrang, W.; Ponomarev, A.; Schubert, A.; Shwageraus, E.; Stopher, M.; Van Uffelen, P.; Zhao, X.; A 2-D correlation to evaluate fuel-cladding gap thermal conductance in mixed oxide fuel elements for sodium-cooled fast reactors. International Nuclear Fuel Cycle Performance Conference / Light Water Reactor Fuel Conference (GLOBAL / TOP FUEL 2019), Seattle, WA, USA, 22.–27. September 2019.

[13]   Bühler, L.; Brinkmann, H.-J.; Klüber, V.; Köhly, C.; Mistrangelo, C.; Magnetohydrodynamics for liquid-metal blankets. Annual Report 2017-2018 of the Institute for Nuclear and Energy Technologies. Ed.: T. Schulenberg, 9–18, KIT Scientific Publishing, Karlsruhe. Volltext der Publikation als PDF-Dokument

[14]   Bühler, L.; Brinkmann, H.-J.; Köhly, C.; Experimental study of liquid metal magnetohydrodynamic flows near gaps between flow channel inserts. Fusion engineering and design, 146 (Part B), 1399–1402. doi:10.1016/j.fusengdes.2018.11.034

[15]   Bühler, L.; Brinkmann, H.-J.; Mistrangelo, C.; Experimental Investigation of Liquid Metal Pipe Flow in a Strong Non-Uniform Magnetic Field. Proceedings of the 11th PAMIR International Conference, Fundamental and Applied MHD, Reims, F, July 1-5, 2019, 157–161.

[16]   Cai, J.; Ip, K. F.; Eze, C.; Zhao, J.; Cai, J.; Zhang, H.; Dispersion of radionuclides released by nuclear accident and dose assessment in the Greater Bay Area of China. Annals of nuclear energy, 132, 593–602. doi:10.1016/j.anucene.2019.06.045

[17]   Chauvin, N.; Capriotti, L.; Gianfelici, S.; Harp, J.; Kim, J. H.; Lainet, M.; Lee, C. B.; Ogata, T.; Ohta, H.; Ozawa, T.; Schubert, A.; Van Uffelen, P.; Cornet, S.; Benchmark Study on Innovative Fuels for Fast Reactors with Fuel Performance Code. International Nuclear Fuel Cycle Performance Conference / Light Water Reactor Fuel Conference (GLOBAL / TOP FUEL 2019), Seattle, WA, USA, 22.–27. September 2019.

[18]   Chen, X.-N.; Gabrielli, F.; Rineiski, A.; Schulenberg, T.; Boiling water cooled travelling wave reactor. Annals of nuclear energy, 134, 342–349. doi:10.1016/j.anucene.2019.06.037

[19]   Coupe, P.; Denkevits, A.; van Dijk, N.; Jedicke, O.; Jordan, T.; Kaup, B.; Kotchourko, A.; Kuznetsov, M.; Lelyakin, A.; Prestel, F.; Stassen, M.; Xiao, J.; Xu, Z.; Zhang, H.; Hydrogen Risk Assessment for Nuclear Applications and Safety of Hydrogen as an Energy Carrier. Annual Report 2017-2018 of the Institute for Nuclear and Energy Technologies. Ed.: T. Schulenberg, 65–70, KIT Scientific Publishing, Karlsruhe. Volltext der Publikation als PDF-Dokument

[20]   Ding, H.; Tong, J.; Raskob, W.; Zhang, L.; An approach for radiological consequence assessment under unified temporal and spatial coordinates considering multi-reactor accidents. Annals of nuclear energy, 127, 450–458. doi:10.1016/j.anucene.2018.12.024

[21]   Fluhrer, B.; Gaus-Liu, X.; Miassoedov, A.; Journeau, C.; Piluso, P.; Bechta, S.; Ma, W.; Manara, D.; Hózer, Z.; Kiselova, M.; Keim, T.; Langrock, G.; Belloni, F.; Kurata, M.; Bottomley, D.; Okamoto, K.; Main Outcomes of the European SAFEST Project towards a Pan-European Lab on Corium Behaviour in Severe Accidents. The 9th European Review Meeting on Severe Accident Research (ERMSAR2019), Prague, Czech Republic, March 18-20, 2019, 1–12.

[22]   Foit, J. J.; Cron, T.; Fluhrer, B.; Melt/Concrete Interface Temperature Relevant to MCCI Process. The 9th European Review Meeting on Severe Accident Research (ERMSAR2019), Prague, Czech Republic, March 18-20, 2019.

[23]   Friedrich, A.; Grune, J.; Sempert, K.; Kuznetsov, M.; Jordan, T.; Hydrogen combustion experiments in a vertical semi-confined channel. International journal of hydrogen energy, 44 (17), 9041–9049. doi:10.1016/j.ijhydene.2018.06.098

[24]   Gabrielli, F.; Maschek, W.; Li, R.; Boccaccini, C. M.; Flad, M.; Gianfelici, S.; Vezzoni, B.; Rineiski, A.; Probabilistic evaluation of the energetics upper bound during the transition phase of an unprotected loss of flow accident for a sodium cooled fast reactor by using a

Phenomenological Relationship Diagram. Nuclear engineering and design, 341, 146–154. doi:10.1016/j.nucengdes.2018.11.004

[25] Gaus-Liu, X.; Impact of vessel geometry and boundary condition on the heat transfer of liquid corium in LWR lower head. 27th International Conference on Nuclear Engineering: Nuclear Power Saves the World!, ICONE 2019; Tsukuba International Congress CenterTsukuba, Ibaraki; Japan; May 19-24, 2019, American Society of Mechanical Engineers (ASME), New York (NY).

[26] Gaus-Liu, X.; Albrecht, G.; Cron, T.; Fluhrer, B.; Foit, J.; Madakoro, H.; Stängle, R.; Vervoortz, M.; Wenz, T.; Analysis of Severe Accidents. Annual Report 2017-2018 of the Institute for Nuclear and Energy Technologies. Ed.: T. Schulenberg, 29–36, KIT Scientific Publishing, Karlsruhe. Volltext der Publikation als PDF-Dokument

[27] Gaus-Liu, X.; Cron. T.; Fluhrer, B.; Experimental Studies on Two-Layer Corium Heat Transfer in Light Water Reactor Lower Head in LIVE2D Facility. 18th International Topical Meeting on Nuclear Reactor Thermal Hydraulics (NURETH-18), Portland, Oregon, USA, August 18-23, 2019., 796–809, ANS : LaGrange Park, Ill.

[28] Gaus-Liu, X.; Cron, T.; Fluhrer, B.; Wenz, T.; Miassoedov, A.; Experimental Study on the Behaviour of In-Vessel Two-Layer Melt Pool in LIVE2D Facility. The 9th European Review Meeting on Severe Accident Research (ERMSAR2019), Prague, Czech Republic, March 18-20, 2019, 72/1–14, AF POWER agency, Prag.

[29] Gaus-Liu, X.; Miassoedov, A.; Journeau, C.; Cassiaut-Louis, N.; Chen, P.; Zhang, H.; Liao, Y.; Hu, P.; Kuang, B.; Zhang, Y.; Tian, W.; Deng, J.; Gong, H.; Sheng, F.; The Outcome of the ALISA Project: Access to Large Infrastructures for Severe Accident in Europe and in China. 9th European Review Meeting on Severe Accident Research (ERMSAR

2019), Prag, CZ, 18.-20.03.2019, 90/1–19, AF POWER agency, Prag.

[30] Grune, J.; Sempert, K.; Kuznetsov, M.; Jordan, T.; Experimental Investigation of Unconfined Spherical and Cylindrical Flame Propagation in Hydrogen-Air Mixtures. 8th International Conference on Hydrogen Safety (ICHS 2019), Adelaide, Australia, 24.–26. September 2019.

[31] Hartig, M.; Numerical Simulation of Fluid-Structure Interaction during the Expansion Phase in Sodium Cooled Fast Reactors. Dissertation. Karlsruhe. doi:10.5445/IR/1000099792

[32] Haste, T.; Barrachin, M.; Fichot, F.; Repetto; G.; Miassoedov, M.; Steinbrück, M.; Stuckert, J.; Buck, M.; Bechta, S.; Le Belguet, A.; Hollands, T.; Journeau, C.; Pontillon, Y.; Lind, T.; Birchley, J.; Hozer, Z.; Horvath, G. L.; Bottomley, P. D. W.; CoreSOAR Core Degradation State-of-the Art Report Update: Conclusions. 9th Conference on Severe Accident Research (ERMSAR2019), Prague, Czech Republic, March 18-20, 2019, paper 022.

[33] Holbein, B.; Theoretische und Experimentelle Kältemittel- und Dichtungsauswahl und Komponentenentwicklung zur Langzeitkühlung von Elektronik in Untertagewerkzeugen. Dissertation. Karlsruhe. doi:10.5445/IR/1000094597

[34] Ji, Y.; Zhang, H.; Sun, J.; Shi, L.; Thermal performance optimization of a fuel element in particle bed reactors for nuclear thermal propulsion. Nuclear engineering and design, 355, 110316. doi:10.1016/j.nucengdes.2019.110316

[35] Jordan, T.; Wasserstoff - Sicherheitsthemen. Wasserstoffworkshop des KIT (2019), Karlsruhe, Deutschland, 17. September 2019. Volltext der Publikation als PDF-Dokument

[36] Jordan, T.; Numerical analytical code development at Karlsruhe Institute of Technology KIT. Fukushima Research Conference –

Workshop on Nuclear Hydrogen Safety (FRCHS 2019), Fukushima, Japan, 17.–18. Oktober 2019. Volltext der Publikation als PDF-Dokument

[37]   Jordan, T.; Update on ISO PWI24077 / Safe Use of LH2 in Non-industrial Settings / Contributions of the FCH JU Project PRES-LHY. ISO TC 197 - Plenary Meeting (2019), Grenoble, Frankreich, 9.–13. Dezember 2019. Volltext der Publikation als PDF-Dokument

[38]   Jordan, T.; Wasserstoff - Der Energiespeicher für die Energiewende?. Kine-Talk, Karlsruher Initiative zur nachhaltigen Energiewirtschaft (kine 2019), Karlsruhe, Deutschland, 3. Dezember 2019. Volltext der Publikation als PDF-Dokument

[39]   Jordan, T.; The European Hydrogen Safety Panel EHSP. Programme Review Days (2019), Brüssel, Belgien, 19.–20. November 2019. Volltext der Publikation als PDF-Dokument

[40]   Jordan, T.; Analysis of H2 related incident and accident database HIAD. HRS Workshop H2ME (2019), Den Haag, Niederlande, 26. November 2019.

[41]   Jordan, T.; Safety of liquified hydrogen systems and infrastructure. International School Progress in Hydrogen Safety (2019), Belfast, Vereinigtes Königreich, 11.–15. März 2019. Volltext der Publikation als PDF-Dokument

[42]   Jordan, T. (2019, Februar 4). Hydrogen Safety International Perspective. The Future of Gas II (2019), London, Vereinigtes Königreich, 4.–5. Februar 2019. Volltext der Publikation als PDF-Dokument

[43]   Jordan, T.; PRESLHY Experiment series E3.1 (Cryogenic Hydrogen Blowdown/Discharge) results – part A "high pressure". doi:10.5445/IR/1000096833

[44]   Jordan, T.; Cirrone, D.; Prenormative REsearch for Safe use of Liquid HYdrogen.

Symposium on Hydrogen Liquefaction and LH2 Storage (2019), Perth, Australien, 26.–27. September 2019. Volltext der Publikation als PDF-Dokument

[45]   Jordan, T.; Jallais, S.; Barnard, L.; Venetsanos, A.; Coldrick, S.; Kuznetsov, M.; Cirrone, D.; Status of the pre-normative research project PRESLHY for the safe use of LH2. 8th International Conference on Hydrogen Safety (ICHS 2019), Adelaide, Australia, 24.–26. September 2019.

[46]   Kennedy, G.; Van Tichelen, K.; Pacio, J.; Di Piazza, I.; Uitslag-Doolaard, H.; Thermal-Hydraulic Experimental Testing of the Myrrha Wire-Wrapped Fuel Assembly. Nuclear technology,   1–12. doi:10.1080/00295450.2019.1620539

[47]   Klüber, V.; Bühler, L.; Mistrangelo, C.; Numerical simulations of 3D magnetohydrodynamic flows in dual-coolant lead lithium blankets. Fusion engineering and design, 139. doi:10.1016/j.fusengdes.2019.01.055

[48]   Klüber, V.; Bühler, L.; Mistrangelo, C.; Numerical Investigation of Liquid Metal Flow in Square Chennels under Inclined Magnetic Fields for Fusion Relevant Parameters. Proceedings of the 11th PAMIR International Conference, Fundamental and Applied MHD, Reims, F, July 1-5, 2019, 162–166.

[49]   Köhly, C.; Bühler, L.; Mistrangelo, C.; Design of a Test Section to Analyze Magneto-Convection Effects in WCLL Blankets. Fusion science and technology, 75 (8), 1010–1015. doi:10.1080/15361055.2019.1607705

[50]   Köhly, C.; Neuberger, H.; Bühler, L.; Fabrication of thin-walled fusion blanket components like flow channel inserts by selective laser melting. Fusion engineering and design, 143,   171–179.   doi:10.1016/j.fusengdes.2019.03.184

[51]   Kuhn, D.; Evaluierung von Ausfällungsinhibitoren für das Molassebecken "EvA-M". 7.

Praxisforum Geothermie.Bayern (2019), München, Deutschland, 7.–8. Oktober 2019. Volltext der Publikation als PDF-Dokument

[52]   Kuhn, D.; Low enthalpy ressources - Applications and potential: Energy from renewables and industry. Science Industry Workshop "KIT - Jiangsu Competence Center for Environmental and Energy Research and Technology" (2019), Nanjing, China, 28. Februar–1. März 2019.

[53]   Kuznetsov, M.; Grune, J.; Experiments on combustion regimes for hydrogen/air mixtures in a thin layer geometry. International journal of hydrogen energy, 44 (17), 8727–8742. doi:10.1016/j.ijhydene.2018.11.144

[54]   Laube, T.; Marocco, L.; Niedermeier, K.; Pacio, J.; Wetzel, T.; Thermodynamic Analysis of High-Temperature Energy Storage Concepts Based on Liquid Metal Technology. Energy technology, Article no: 1900908. doi:10.1002/ente.201900908. Volltext der Publikation als PDF-Dokument

[55]   Lifante, C.; Ben Hadj Ali, A.; Eickenbusch, H.; Bruder, M.; Kaiser, F.; Gabriel, S.; Prediction of Convective Boiling up to Critical Heat Flux (CHF) Conditions for Test Facilities with Vertical Heaters. 27th International Conference on Nuclear Engineering (ICONE 2019), Ibaraki, Japan, 19.–24. Mai 2019.

[56]   Liu, X.; Xiong, J.; Cheng, X.; Multi-scale thermal-hydraulics analysis on SCWR fuel qualification test loop. Scientia Sinica: Physica, Mechanica et Astronomica, 49 (11), article No.114604. doi:10.1360/SSPMA2018-00234

[57]   Li, Y.; Xiao, J.; Zhang, Z.; Breitung, W.; Travis, J.; Kuznetsov, M.; Jordan, T.; Analysis of Transient Hydrogen Release, Dispersion and Explosion in a Tunnel with Fuel Cell Vehicles Using All-Speed CFD Code GASFLOW-MPI. 8th International Conference on Hydrogen Safety (ICHS 2019), Adelaide, Australia, 24.–26. September 2019.

[58]   Li, Y.; Zhang, H.; Xiao, J.; Jordan, T.; Numerical study of thermal hydraulics behavior on the integral test facility for passive containment cooling system using GASFLOW-MPI. Annals of nuclear energy, 123, 86–96. doi:10.1016/j.anucene.2018.09.014

[59]   Madokoro, H.; Miassoedov, A.; Schulenberg, T.; Coupling of a reactor analysis code and a lower head thermal analysis solver. Journal of nuclear engineering and radiation science, 5 (1), Art.-Nr.: 011017. doi:10.1115/1.4041278

[60]   Margulis, M.; Blaise, P.; Gabrielli, F.; Gruel, A.; Mellier, F.; Gilad, E.; The path for innovative severe accident neutronics studies in ZPRs – Analysis of SNEAK-12B experiments for core disruption in LMFBRs. Annals of nuclear energy, 124, 119–131. doi:10.1016/j.anucene.2018.09.025

[61]   Massone, M.; Wang, S.; Rineiski, A.; Analytical Modeling of the Emergency Draining Tank for a Molten Salt Reactor. Annual Report 2017-2018 of the Institute for Nuclear and Energy Technologies. Ed.: T. Schulenberg, 19–28, KIT Scientific Publishing, Karlsruhe. Volltext der Publikation als PDF-Dokument

[62]   Mistrangelo. C.; Bühler, L.; Köhly, C.; Considerations on Magneto-Convective Flows in Model Geometries Relevant for Fusion Applications. Proceedings of the 11th PAMIR International Conference, Fundamental and Applied MHD, Reims, F, July 1-5, 2019, 7–11.

[63]   Möhrle, S.; Raskob, W.; Reusing Strategies for Decision Support in Disaster Management - A Case-based High-level Petri Net Approach. Advances in Artificial Intelligence: Reviews. Ed.: S.Y. Yurish. Vol. 1, 85–115, IFSA Publishing, Barcelona, E. Volltext der Publikation als PDF-Dokument

[64]   Niedermeier, K.; Numerical investigation of a thermal storage system using sodium as heat transfer fluid (KIT Scientific Reports ; 7755). Dissertation. KIT Scientific Publishing,

Karlsruhe. doi:10.5445/KSP/1000093902. Volltext der Publikation als PDF-Dokument

[65] Ottenburger, S.; Ufer, U.; Smart Space and Concrete Risks. 24th International Conference on Urban Planning and Regional Development in the Information Society (REAL CORP 2019), Karlsruhe, Deutschland, 2.–4. April 2019.

[66] Ottenburger, S. S.; Raskob, W.; Smart Grid Resilience: Concepts on dealing with Power Scarcity for decentralized Power Systems. Annual Report 2017-2018 of the Institute for Nuclear and Energy Technologies. Ed.: T. Schulenberg, 57–64, KIT Scientific Publishing, Karlsruhe. Volltext der Publikation als PDF-Dokument

[67] Ottenburger, S. S.; Ufer, U.; Smart Space and Concrete Risks. Is this the real world? Perfect Smart Cities vs. Real Emotional Cities - Tagungsband der REAL CORP 2019 - 24. internationale Konferenz zu Stadtplanung und Regionalentwicklung in der Informationsgesellschaft, Karlsruhe, Deutschland, 2. - 4. April 2019. Ed. M. Schrenk, 63–67, Competence Center of Urban and Regional Planning (CORP), Wien.

[68] Ottenburger, S.; Bai, S.; Raskob, W.; MCDA-based Genetic Algorithms for Developing Disaster Resilient Designs of Critical Supply Networks. 6th International Conference on Information and Communication Technologies for Disaster Management (ICT-DM 2019), Paris, Frankreich, 18.–20. Dezember 2019.

[69] Ottenburger, S.; Ufer, U.; Quartierspeicher für mehr urbane Resilienz. Ein Blick über den Tellerrand technischer Risiken bei der Energiewende. Transforming cities, 2, 66–69.

[70] Ottenburger, S. S.; Stromversorgung und urbanes Kontinuitätsmanagement, Versorgungssicherheit 2.0 - Smarte Konzepte zur Erhöhung der Resilienz moderner Städte in Zeiten dezentraler Strombereitstellung. Transforming cities, 4, 60–63.

[71] Ottenburger, S. S.; Smart Urban Resilience -Smart Grids and Critical Infrastructure Protection. 1st Smart Cities Breakfast Conference (2019), Washington, DC, USA, 3. Oktober 2019.

[72] Ottenburger, S. S.; Smart Urban Resilience - Implementing Sustainability in a Sustainable Way!. DAAD Workshop on Sustainable Urban Development in Europe and North Africa (2019), Tunis, Tunesien, 22.–24. November 2019.

[73] Ottenburger, S. S.; Continuous and Urban Resilient Power Supply During Critical States. 10th Resilient Cities 2019 : Global Forum on Urban Resilience and Adaptation (2019), Bonn, 26.–28. Juni 2019. Volltext der Publikation als PDF-Dokument

[74] Ottenburger, S. S.; Mohr, S.; Daniell, J.; Kunz, M.; Integrated Risk Analysis for Safe and Resilient Operation of Dams - Early Warning System for Risk Reduction. DAMAST (Dams and Seismicity), BMBF-FONA Project - Initial Meeting (2019), Sugdidi, Georgien, 15. Oktober 2019.

[75] Pacio, J.; Daubner, M.; Fellmoser, F.; Hering, W.; Jäger, W.; Stieglitz, R.; Wetzel, T.; Construction of experimental liquid-metal facilities. Thermal Hydraulics Aspects of Liquid Metal Cooled Nuclear Reactors. Ed.: F. Roelofs, 107–125, Elsevier Science & Technology, San Diego. doi:10.1016/B978-0-08-101980-1.00013-2

[76] Pacio, J.; Daubner, M.; Fellmoser, F.; Wetzel, T.; Experimental study of the influence of inter-wrapper flow on liquid-metal cooled fuel assemblies. Nuclear engineering and design, 352, Art. Nr.: 110145. doi:10.1016/j.nucengdes.2019.06.007

[77] Pacio, J.; Daubner, M.; Wetzel, T.; High temperature thermal energy storage with liquid metals. 13. International Renewable Energy Storage Conference (IRES 2019), Düsseldorf, Deutschland, 12.–14. März 2019. Volltext der Publikation als PDF-Dokument

[78] Pacio, J.; Daubner, M.; Wetzel, T.; Uitslag-Doolaards, H.; Mathur, A.; Roelofs, F.; Inter-Wrapper Flow: LBE Experiments and Simulations. 18th International Topical Meeting on Nuclear Reactor Thermal Hydraulics (NURETH-18), Portland, Oregon, USA, August 18-23, 2019., 796–809, ANS : LaGrange Park, Ill.

[79] Pacio, J.; Niedermeier, K.; Wetzel, T.; High-temperature thermal energy storage concepts based on liquid metal technology. Eurotherm Seminar 112 : Advances in Thermal Energy Storage (2019), Lleida, Spanien, 15.–17. Mai 2019.

[80] Pacio, J.; Schroer, C.; Tromm, W.; Weisenburger, A.; Safety-related studies on heavy-liquid metal technology for advanced reactors in Europe. 50. Jahrestagung Kerntechnik (AMNT 2019), Berlin, Deutschland, 7.–8. Mai 2019.

[81] Pacio, J.; Stoppel, L.; Wetzel, T.; Non-nuclear applications of HLMs. Heavy Metal Summer School (2019), Mol, Belgien, 17.–21. Juni 2019.

[82] Pacio, J. C.; Daubner, M.; Wetzel, T.; Mathur, A.; Uitslag-Doolaard, H.; Roelofs, F.; Inter-Wrapper Flow: LBE Experiments and Simulations. 18th International Topical Meeting on Nuclear Reactor Thermal Hydraulics (NURETH 2019), Portland, OR, USA, 18.–23. August 2019.

[83] Raquet, M. R.; Stochastische Euler-Euler-PDF-Methodik für das Zwei-Fluid-Modell und Anwendung auf kavitierende Strömungen der Automobilindustrie. Dissertation. Karlsruhe. doi:10.5445/IR/1000096827. Volltext der Publikation als PDF-Dokument

[84] Raskob, W.; Haller, C.; Hasemann, I.; Schichtel, T.; Trybushnyi, D.; Source Term Reconstruction Module in JRODOS. 5th NERIS Workshop (2019), Roskilde, Dänemark, 3.–5. April 2019.

[85] Raskob, W.; Münzberg, T.; Schmutzige Bomben und ihre möglichen Folgen für die Bevölkerung. CRISIS PREVENTION: Fachportal für Gefahrenabwehr, Innere Sicherheit und Katastrophenhilfe.

[86] Roelofs, F.; Shams, A.; Batta, A.; Moreau, V.; Di Piazza, I.; Gerschenfeld, A.; Planquart, P.; Tarantino, M.; Liquid Metal Thermal Hydraulics - Outcomes of the SESAME project. 18th International Topical Meeting on Nuclear Reactor Thermal Hydraulics (NURETH-18), Portland, Oregon, USA, August 18-23, 2019., 234–247, ANS : LaGrange Park, Ill.

[87] Roelofs, F.; Shams, A.; Batta, A.; Moreau, V.; Di Piazza, I.; Gerschenfeld, A.; Planquart, P.; Tarantino, M.; SESAME Project: Advancements in Liquid Metal Thermal Hydraulics Experiments and Simulations. 9th European Commission Conference on EURATOM Research and Training in Safety of Reactor Systems and Radioactive Waste Management (FISA / EURADWASTE 2019), Piteşti, Rumänien, 4.–7. Juni 2019. Volltext der Publikation als PDF-Dokument

[88] Roelofs, F.; Uitslag-Doolaard, H.; Dovizio, D.; Mikuz, B.; Shams, A.; Bertocchi, F.; Rohde, M.; Pacio, J.; Di Piazza, I.; Kennedy, G.; Van Tichelen, K.; Obabko, A.; Merzari, E.; Towards validated prediction with RANS CFD of flow and heat transport in a wire-wrap fuel assembly. Nuclear engineering and design, 353, Article: 110273. doi:10.1016/j.nucengdes.2019.110273

[89] Roelofs, F.; Uitslag-Doolaard, H.; Mikuz, B.; Dovizio, D.; De Santis, D.; Shams, A.; Bertocchi, F.; Rohde, M.; van Tichelen, K.; Keijers, S.; Kennedy, G.; Batta, A.; Pacio, J.; Planquart, P.; Obabko, A.; Brockmeyer, L.; Merzari, E.; Vaghetto, R.; Hassan, Y.; Leonard, D.; Martin, M.; Jackson, B.; Steer, M.; Delchini, M.; Pointer, D.; CFD and Experiments for Wire-wrapped Fuel Assemblies. 18th International Topical Meeting on Nuclear Reactor Thermal Hydraulics (NURETH-18), Portland, Oregon, USA, August 18-23, 2019, 5716–5729, ANS : LaGrange Park, Ill.

[90] Schröder, E.; Thomauske, K.; Kuhn, D.; Messung der thermodynamischen Thermalwassereigenschaften an Geothermiestandorten. Annual Report 2017-2018 of the Institute for Nuclear and Energy Technologies. Ed.: T. Schulenberg, 71–76, KIT Scientific Publishing, Karlsruhe. Volltext der Publikation als PDF-Dokument

[91] Schulenberg, T.; Structure and Laboratories of the Institute for Nuclear and Energy Technologies. Annual Report 2017-2018 of the Institute for Nuclear and Energy Technologies. Ed.: T. Schulenberg, 1–7, KIT Scientific Publishing, Karlsruhe. Volltext der Publikation als PDF-Dokument

[92] Schulenberg, T. (Hrsg.).; Annual Report 2017-2018 of the Institute for Nuclear and Energy Technologies (KIT Scientific Reports ; 7756). KIT Scientific Publishing, Karlsruhe. doi:10.5445/KSP/1000095726. Volltext der Publikation als PDF-Dokument

[93] Schulenberg, T.; Heinze, D.; Numerical Simulation of a Steam Injector for Passive Residual Heat Removal. International Symposium on Super-Critical Water-Cooled Reactors (ISSCWR-9 2019), Vancouver, Kanada, 10.–14. März 2019.

[94] Shi, Y.; Eze, C.; Xiong, B.; He, W.; Zhang, H.; Lim, T. M.; Ukil, A.; Zhao, J.; Recent development of membrane for vanadium redox flow battery applications: A review. Applied energy, 238, 202–224. doi:10.1016/j.apenergy.2018.12.087

[95] Stoppel, L.; Fehling, T.; Geißler, T.; Baake, E.; Wetzel, T.; Carbon dioxide free production of hydrogen. Annual Report 2017-2018 of the Institute for Nuclear and Energy Technologies. Ed.: T. Schulenberg, 43–56, KIT Scientific Publishing, Karlsruhe. Volltext der Publikation als PDF-Dokument

[96] Tolias, I. C.; Giannissi, S. G.; Venetsanos, A. G.; Keenan, J.; Shentsov, V.; Makarov, D.; Coldrick, S.; Kotchourko, A.; Ren, K.; Jedicke, O.; Melideo, D.; Baraldi, D.; Slater, S.; Duclos, A.; Verbecke, F.; Molkov, V.; Best practice guidelines in numerical simulations and CFD benchmarking for hydrogen safety applications. International journal of hydrogen energy, 44 (17), 9050–9062. doi:10.1016/j.ijhydene.2018.06.005

[97] Trubetskaya, A.; Kling, J.; Ershag, O.; Attard, T. M.; Schröder, E.; Removal of phenol and chlorine from wastewater using steam activated biomass soot and tire carbon black. Journal of hazardous materials, 365, 846–856. doi:10.1016/j.jhazmat.2018.09.061

[98] Uitslag-Doolaard, H. J.; Roelofs, F.; Pacio, J. C.; Batta, A.; Experiment design to assess the inter-wrapper heat transfer in LMFR. Nuclear engineering and design, 341, 297–305. doi:10.1016/j.nucengdes.2018.11.019

[99] Utili, M.; Bassini, S.; Boccaccini, L.; Bühler, L.; Cismondi, F.; Del Nevo, A.; Eboli, M.; DiFonzo, F.; Hernandez, T.; Wulf, S.; Kordač, M.; Martelli, D.; De les Valls, E. M.; Melichar, T.; Mistrangelo, C.; Tarantino, M.; Tincani, A.; Vála, L.; Status of Pb-16Li technologies for European DEMO fusion reactor. Fusion engineering and design, 146, Part B (2019) 2676-2681. doi:10.1016/j.fusengdes.2019.04.083

[100] Walsh, L.; Ulanowski, A.; Kaiser, J. C.; Woda, C.; Raskob, W.; Risk bases can complement dose bases for implementing and optimising a radiological protection strategy in urgent and transition emergency phases. Radiation and environmental biophysics, 58 (4), 539–552. doi:10.1007/s00411-019-00809-x. Volltext der Publikation als PDF-Dokument

[101] Wang, S.; Massone, M.; Rineiski, A.; Merle-Lucotte, E.; Laureau, A.; Gérardin, D.; Heuer, D.; Allibert, M.; A passive decay heat removal system for emergency draining tanks of molten salt reactors. Nuclear engineering and design, 341, 423–431. doi:10.1016/j.nucengdes.2018.11.021

[102] Yabing, L.; Han, Z.; Jianjun, X.; Jordan, T.; Preliminary assessment of the long-term radiolytic gas accumulation in modified measurement pipeline for BWR with GasFLOW-MPI. 27th International Conference on Nuclear Engineering: Nuclear Power Saves the World!, ICONE 2019; Tsukuba International Congress CenterTsukuba, Ibaraki; Japan; 19 May 2019 through 24 May 2019, American Society of Mechanical Engineers (ASME), New York (NY).

[103] Yanez Escanciano, J.; Class, A. G.; POD-Galerkin modeling of a heated pool. Progress in nuclear energy, 113, 196–205. doi:10.1016/j.pnucene.2019.01.017

[104] Yanez, J.; Class, A. G.; POd-rom verification of the accuracy of the simulation of a heated pool. 27th International Conference on Nuclear Engineering: Nuclear Power Saves the World!, ICONE 2019; Tsukuba International Congress CenterTsukuba, Ibaraki; Japan; 19 May 2019 through 24 May 2019, American Society of Mechanical Engineers (ASME), New York (NY).

[105] Yu, F.; Zhang, H.; Class, A.; Xiao, J.; Travis, J. R.; Jordan, T.; Winding number based automatic mesh generation algorithm for hydrogen analysis code GASFLOW-MPI. International journal of hydrogen energy, 44 (26), 14070–14084. doi:10.1016/j.ijhydene.2019.03.231

[106] Zhang, H.; Li, Y.; Kuznetsov, M.; Jordan, T.; Xiao, J.; Numerical Study of the Detonation Benchmark Using GASFLOW-MPI. 8th International Conference on Hydrogen Safety (ICHS 2019), Adelaide, Australia, 24.–26. September 2019.

[107] Zhang, H.; Li, Y.; Xiao, J.; Travis, J. R.; Jordan, T.; Numerical study of the stratification erosion benchmark for NPPs containment using CFD code GASFLOW-MPI. Annals of nuclear energy, 132, 199–211. doi:10.1016/j.anucene.2019.04.033

[108] Zhang, R.; Shen, F.; Albrecht, G.; Yang, Y.; The experimental study of fuel coolant interaction in flooded cavity using DISCO facility. 27th International Conference on Nuclear Engineering: Nuclear Power Saves the World!, ICONE 2019; Tsukuba International Congress CenterTsukuba, Ibaraki; Japan; 19 May 2019 through 24 May 2019, American Society of Mechanical Engineers (ASME), New York (NY).

The annual report of the Institute for Nuclear and Energy Technologies of KIT summarizes its research activities in 2019 and provides some highlights of each working group of the institute. Among them are thermal-hydraulic analyses for fusion reactors, accident analyses for light water reactors, innovative nuclear concepts and research on innovative energy technologies like liquid metal technologies for energy conversion, hydrogen technologies and geothermal power plants. Moreover, the institute has been engaged in education and training in energy technologies, illustrated by e.g. training in nuclear engineering by the Framatome Professional School courses.